ISSN 1000-9620

Marine Science Bulletin

Volume 3 • Number 2 2001

LIBRARY
FEB 2 6 2002
National Oceanic &
Atmospheric Administration
U.S. Dept. of Commerce

LIBRARY
Pacific Islands Fisheries Science Center
NOAA Fisheries
Honolulu, Hawai'i

ISSN 1000-9620
02>
9 771000 962001

NATIONAL MARINE DATA AND
INFORMATION SERVICE OF CHINA

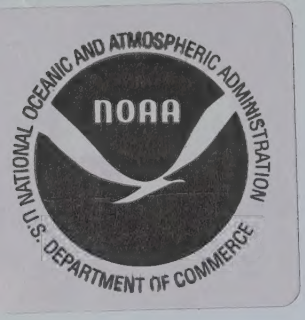
NOAA
U.S. DEPARTMENT OF COMMERCE
NATIONAL OCEANIC AND ATMOSPHERIC ADMINISTRATION

MARINE SCIENCE BULLETIN

Vol.3 No.2 Oct. 2001

LIBRARY
FEB 2 6 2002
National Oceanic &
Atmospheric Administration
U.S. Dept. of Commerce

CONTENTS

Distribution Characteristics of Mean Seawater Temperature Related to the Thermocline in the Deep-Water Area of Nasha……*Qiu Zhang*（邱 章）*et al.*（1）

Heat Transfer Coefficient between Ice Cover and Water in the Bohai Sea ……*Ji Shunying*（季顺迎）*et al.*（6）

A Method of Coding and Decoding in Underwater Image ransmission ……*Ceng En*（程 恩）*et al.*（13）

Numerical Investigation on Submerged Horizontal Plate……*Kang Haigui*（康海贵）*et al.*（19）

Chemical Fluxes of Asian Rivers into Oceans and their Controlling Factors ……*Yang Shouye*（杨守业）*et al.*（30）

Sea to air flux of dimethyl sulfide and its effect on the environment ……*Wu Ping*（吴 萍）*et al.*（38）

Application of hydrocarbons biomarkers in marine organic geochemistry ……*Wu Ying*（吴 莹）*et al.*（47）

Phosphorous forms in Sediments and their Distribution in the Yangtze Estuary and Coastal Areas ……*Liu Min*（刘 敏）*et al.*（55）

Relation between Gravity Field Feature and Tectonics and Earthquakes in Taiwan and Its Adjacent Sea……*Zhang Chijun*（张赤军）*et al.*（63）

Palynological evidence on climate changes in the East China Sea during Mid and Late Holocene ……*Li Zhen*（李 珍）*et al.*（73）

Enhancement Effects of three rare earth elements on the growth of Chaetoceros Mulleri ……*Qu Keming*（曲克明）*et al.*（83）

Supplement and consumption of dissolved oxygen and their seasonal variations in shrimp pond……*Sun Yue*（孙 耀）*et al.*（89）

Distribution Characteristics of Mean Seawater Temperature Related to the Thermocline in the Deep-Water Area of Nansha

Qiu Zhang (邱 章), Cai Shuqun (蔡树群), Zhu Liangsheng (朱良生)
South China Sea Institute of Oceanology, Academia Sinica, Guangzhou, Guangdong 510301

Abstract On the bisis of determining the there elements of thermocline (depth [upper bound depth], thickness and intensity) and the maximum vertical temperature gradient of the surveying station, the paper calculates the mean temperature of the Nansha deep-water surveying station within the upper-bound depth layer of thermocline and the mean temperature below the lower-bound depth of thermocline between the 300m and 800m layers,respectively. Analysis indicates that the horizontal distribution of mean seawater temperature shows a distinct trend of the low-temperature seawater slowly moving from the northeast to the southeast of Nansha,which seems to have been driven by the Northeast Monsoon. The larger the vertical temperature radient is, the greater is its capability of preventing the heat of the upper seawater from diffusing into the deeper layers on the vertical direction.

Keywords thermocline, low-temperature seawater, vertical thermal diffusion

There have been some researches [1-4] on the phenomenon of thermocline in the Nansha sea area, which mainly deal witn the space-time distribution characteristics and changing patterns of the three elements of thermocline in this sea area, but no research has been reported on the distribution of mean seawater temperature with respect to the elements of thermocline in the Nansha deep-water area and the maximum vertical temperature gradient. The paper also calculates the mean temperature within the upper-bound depth of thermocline and the mean temperature below the lower-bound depth of thermocline between the 300m and 800m layers, and in light of the horizontal distribution of the maximum vertical temperature gradient at the surveying station, analyses the horizontal distribution characteristics of these two mean temperatures from which to attempt to find some laws that may reflect the objective reality.

1 Data and Methods

The data used for analysis in the paper are those from the standard layers of temperature in the integrated deep-water suveying stations of the sea area of Nansha Islands in November, 1997.

The three elements of thermocline are determined in the light of the vertical gradient value of sea water temperature ($\triangle T \triangle Z > 0.05$℃ · m^{-1}) while the maximum vertical temperature gradient value at each surveying station is identified.

With the three elements of thermocline available, the mean temperature within the upper-bound depth of thermocline and the mean temperature below the lower-bound depth of thermocline between

The paper is financially supported by the China National Key Basic Research Project (G1999043810), Guangdong Science and Technology Innovation Project (99B07102G), Chinese Academy of Sciences Innovation Project (KZCX2-206 and CXjj-28) and Chinese National Science Foundation (49976002)

the 300m and 800m layers are calculated with the simple arithmetic mean method ($\overline{T}=\frac{1}{n}\sum_{i=1}^{n} Ti$).

2 Results and Discussion

Fig.1 is the horizontal distribution of thermocline upper-bound depths in the Nansha deep-water station during the suvey. The upper-bound depths of thermocline are between 20m and 50m and its basic distribution characteristic is: with the boundary at about 111°E, the thermocline upper-bound depths in the adjacent sea areas on both sides of the interface are on the small side, i.e., less than 35m, with the minimum depth of 20m occurring to the northwest of Nansha deep-water station (near 110.58°E, 11.50°N); To the east and west sides of the sea area, the thermocline upper-bound depths gradually increase to about 45m, with the maximum depth of 50m occurring to the southeast of the Nansha deep-water survey area (approximately at 113.83° E, 6.00° N).

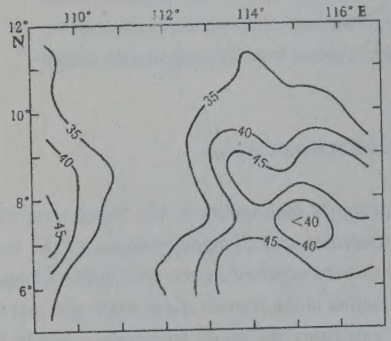

Fig. 1 Horizontal distribution of thermocline depth (m)

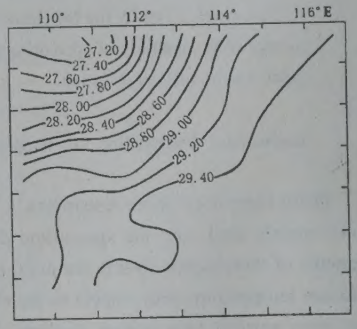

Fig. 2 Horizontal distribution of mean temperature within the upper-bound depths of thermocline (℃)

Fig.2 gives the horizontal distribution of mean temperature within the thermocline upper-bound depths in the deep-water surveying station during the survey. As can be seen from the figure, the basic characteristic of distribution is: the seawater temperature in the northwest of the sea area is on the lower side, with the lowest temperature of 27.06℃ occurring near 111°E, 11.50°N; the mean water temperature in the southeast of the sea area is higher with the highest temperature of 29.71 ℃ occurring near 116.80 ℃ , 9.00°N; During the survey, the mean temperature in the deep-water station within the thermocline upper-bound depths tends to rise slowly from northwest to southeast. As, during the survey, the Northeast Monsoon has affected the Nansha sea area, driven by the Northeast Monsoon, the seawater in the northern South China Sea with relatively lower temperature is continuously transported to the south. But, as this period is just in the early stage of the Northeast Monsoon, the northern sea area of Nansha is more obviously affected than the southern part.In the South China Sea, the Northeast Monsoon is usually stronger in the sea area on the east side of the Zhongnan peninsula than in the sea area on the west side of the Philippines. Therefore, affected by the Northeast Monsoon, it is possible for

the more obvious low-temperature seawater to enter the Nansha sea area from the northwest. The horizontal distribution characteristics of mean temperature in the deep-water station within the thermocline upper-bound depth during this investigation in Nansha bear similarities with the horizontal distribution of temperature at the 10m layer in the studied area of Nansha in November, 1989 as described in Ref.(5).

It can be seen from the results of the thermocline that the lower-bound maximum depth of thermocline is 200m. Judging from the horizontal distribution of temperature beyond the lower bound of thermocline, with the deepening of the water layer, the horizontal differnce of seawater temperature becomes smaller; Up to the depth of 600m, on the east-west direction in this sea area, the seawater temperature increases from 7.20℃ near 109°E to 7.80℃ near 117°E, with a temperature difference of less than 1℃ (Fig.3), i. e., less than 0.1℃ for each longitudinal degree.

On the south-north direction, the temperature difference in the sea area is also very small and the distribution of temperature is on the whole even. The effect of wind on the sea current is generally no longer obvious beyond the depth of 100m[6]. Therefore, it may be concluded from the horizontal distribution of temperature beyond the lower-bound depth of thermocline that there exist no cold or warm flows of deep seawater in the studied area during the season and the temperature changes of deep water bodies, the horizontal thermal diffussion may be regarded as secondary while the vertical thermal diffussion of seawater is the primary factor.As a result, the mean temperature beyond the lower bound of thermocline between 300m and 800m may basically reflect the intensity of seawater thermal diffusion from the upper layer to the deep layer.

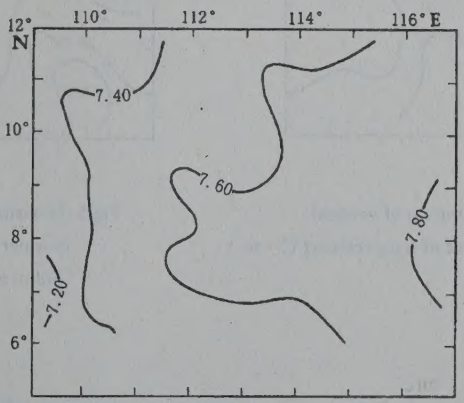

Fig. 3 Horizontal distribution of temperature in water layer of 600m(℃)

Figs.4 and 5 are the horizontal distribution of vertical maximum gradient of temperature and the horizontal distribution of mean temperature between depths of 300m and 800m, respectively. It is obvious that the distribution characteristics in the two figures correspond to each other. The area of the highest values of vertical maximum gradient of temperature in Fig.4 corresponds to the low-value area of mean temperature in Fig.5. The vertical maximum gradient of temperature is on the high side in the northwest of the sea area in Fig.4, with a maximum of 0.43℃ · m^{-1}, occurring near 110.26° E, 11.49°N

while in Fig.5, the mean temperature in this area between depths of 300m and 800m is on the low side, with the lowest temperature reaching 8.17℃. The southwestern part of sea area in Fig.4 is the secondary high-value zone of vertical maximum gradient of temperature with the vertical maximum gradient of temperature of 0.28℃ occurring near 111.30°E, 6.50°E while in Fig.5 the area around here is a secondary low-value zone of mean temperature, which is maintained below 8.70℃. From west to east, the vertical maximum gradient of temperature in the surveying station becomes smaller gradually, with the minimum value of 0.12℃ · m^{-1},occurring near 115° E, 7.42° N. Corresponding to this is a gradual uplift zone of mean temperature below the thermocline lower-bound depth between the depths of 300m and 800m, where the mean temperature gradually rises to the east from the lowest value in the west, with the highest temperature reaching 9.25℃ and occurring near 116, 80° E, 9.00°N. On the vertical direction, the thermocline may well be termed the protective screen for the thermal exchange of seawater between the upper and lower layers. It may be found from the analysis above that the larger the vertical gradient of temperature is, the more obvious are its effects of preventing the heat of upper seawater from diffusing into the deeper layers.

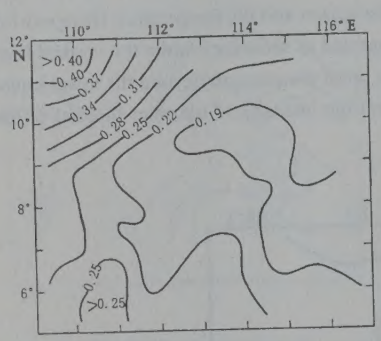

Fig.4 Horizontal distribution of vertical maximum gradient of temperature(℃ · m^{-1})

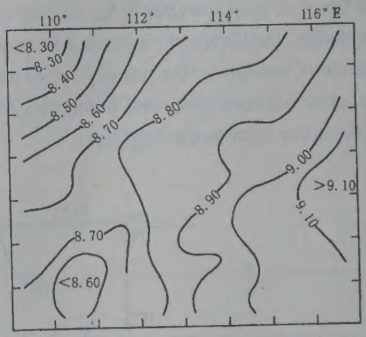

Fig.5 Horizontal distribution of mean temperature between depths of 300m and 800m(℃)

3 Summary

The following preliminary conclusions may be drawn from analysis of the standard layer data of the deep-water stations in the sea area of the Nansha Islands in November of 1997:

(1) The horizontal distribution of mean temperature within the upper-bound depth of thermocline clearly indicates the trend of low-temperature seawater slowly moving from the northwest to the southwest of the Nansha sea area, which seems to have been driven by the Northeast Monsoon.

(2) The horizontal distribution of vertical maximum gradient of temperature at each surveying station and the horizontal distribution of mean temperature between depths of 300m and 800m suggest that the larger the vertical temperature gradient is, the greater is its capability of preventing the heat of the upper seawater from diffusing into the deeper layers on the vertical direction.

References

[1] Qiu Zhang and Huang Qizhou (1994). Analysis of the Space-Time Distribution of the Thermocline in the Sea Area of the Nansha Islands [A]. Collectain of Research Papers on Physical Oceanography in the Sea Area of the Nansha Islands I [C]. Beijing: China Ocean Press, 64-80.

[2] Xu Xizhen,Qiu Zhang and Long Xiaomin (1993). Basic Features of the thermocline in the South China Sea and the One-Dimensional Prediction Model [J], *Oceanologia et Limnologia Sinica*, **24**(5): 494-502.

[3] He Youhai, Guan Cuihua, Wang Sheng'an, *et. al.*(1994). Vertical Distribution of Thermal Structure and Water Temperature in the Southern South China Sea [A]. Collection of Research Papers on Physical Oceanography in the Sea Area of the Nansha Islands I [C]. Beijing: China Ocean Press, 167-177.

[4] Qiu Zhang, Xu Xizhen and Long Xiaomin (1996). Characteristics of Spring Layers in the Studied Sea Area of the Nansha Islands in September of 1994 [J].*Tropic. Oceanology*, **15** (2): 61-67.

[5] Huang Qizhou and Qiu Zhang (1994). Temperature-Salinity Distribution and Water Mass in the Studied Sea Area of the Nansha Islands in 1989 [A.].Collection of Research Papers on Physical Oceanography in the Sea Area of the Nansha Islands I [C]. Beijing: China Ocean Press, 167-177.

[6] Zhang Fan, Huang Qizhou, Wang Wenzhi, *et.al.* (1994). Diagnostic Calculation of the SeasonalMean Sea Current in the Deep-Water Zone of the South China Sea [J], *Tropic Oceanology*, **13** (3): 8-15.

Heat Transfer Coefficient between Ice Cover and Water in the Bohai Sea

Ji Shunying (季顺迎) Yue Qianjin (岳前进) Bi Xiangjun (毕祥军)
State Key Laboratory of Structural Analysis for Industrial Equipment, Dalian University of Technology, Dalian, 116023

Abstract The calculative method of heat transfer coefficient between ice cover and water is analyzed considering the heat balance at ice cover bottom firstly. The heat transfer coefficient is calculated with the meteorological, oceanographic data and sea ice conditions measured on the JZ20-2 Oil/Gas Platform in the Bohai Sea during the winter of 1997/1998. From the results, it is shown that the heat transfer coefficient is smaller in the freezing and melting periods, which is about 0.16×10^{-3} and 0.04×10^{-3} respectively. In the middle of ice season, the heat transfer coefficient has a larger value, which is about 0.5×10^{-3}. Lastly, the influences of ice thickness and ice type on the heat transfer coefficient are discussed. With the heat transfer coefficient determined above, the oceanic heat flux in the winter of 1997~1998 is calculated, and its trend in the winter is analyzed. This study can be referenced in the sea ice numerical simulation and prediction in the Bohai Sea.

Keywords sea ice, oceanic heat flux, heat transfer coefficient, bulk method

Introduction

In the study of sea ice numerical simulation, the oceanic heat flux is an important factor, which influences the ice thickness and the ice edge directly. Since the 1960s , a series of work has been conducted to determinate the oceanic heat flux in different ocean regions. In the previous studies, several methods have been established to determine the oceanic heat flux as follows: the eddy-correlate method (Mcphee, 1987; Maykut, 1986; Wettlaufer, 1991), the bulk model formulation (Omstedt and Wattlaufer, 1992; Moore, 1988; Josberger, 1987), the residual method (Shirasawa, Ingram and Hudier, 1997; Omstedt and Wattlaufer, 1992; Lytle and Ackley, 1996; Harvey, 1990; Tang, 1991) and the sensitivity analysis method (Parkinson and ishington, 1979; Wang et al., 1984; Lu, 1987). The oceanic heat flux is controlled by the transport capability in the ice/water boundary layer, and is influenced by the relative velocity between ice and water, amount of heat available in the water, ice roughness and internal waves, etc. So in many situations the purpose of studying the eddy-correlate method is to determine the heat transfer coefficient of the bulk formula (Omstedt and Svensson, 1992; Shirasawa and Ingram, 1997) for the bulk method can be used to calculate the oceanic heat flux directly in sea ice numerical simulation and forecast.

The key to the oceanic heat flux calculation with bulk formula is to determine heat transfer coefficient. In the past, a series of values of heat transfer coefficient C_h have been determined. For example, Josberger(1987) found that C_h was in the range of $2\sim8\times10^{-4}$ according to the test results in the Bering Sea and the Fram Strait. In the Resolute Passage Sea of Canada, as measured by

Shirasawa *et al.* (1997), C_h was near 2.3×10^{-3}. In the East Arctic, Omested *et al.* (1992) obtained $C_h = (2.8 \pm 1) \times 10^{-3}$. The prime reason for the difference of C_h above was that the heat transfer coefficient has close relation with water salinity, ice type, ice thickness, and other factors.

In the present study, we focus mainly on the measurements taken on the JZ20-2 platform in the north Bohai Sea. The meteorological and oceanographic data, and ice conditions were measured in the winter of 1997/1998. The heat transfer coefficient and the oceanic heat flux are calculated, and their influence factors are discussed.

1 Mathematical Formulation of Heat Transfer Coefficient

In the previous study of oceanic heat flux, several different bulk formulas were adopted. In the widestly applied method, considering ice-water relative velocity, water density, and specific heat of water, the oceanic heat flux can be calculated as(Omstedt, 1992; Shirasawa and Ingram, 1997; Josberger, 1987)

$$F_w = \rho_w c_p C_h u_{wi} (T_w - T_m) \tag{1}$$

where F_w is the oceanic heat flux, ρ_w is the water density, C_h is the heat transfer coefficient, T_w is the water temperature, and T_m is the temperature at the ice/water interface.

To calculate the heat transfer coefficient in the equation (1), the oceanic heat flux should be determined firstly. In the residual method, the ocean heat flux is calculated as the difference between vertical heat flux within the growing sea ice and the latent heat released by freezing at the ice-water interface. As the ice of Bohai Sea is not thick enough, the solar radiation at sea ice bottom should be considered. At any location in the growing ice sheet, the energy balance at the ice-water interface can be described by

$$F_w = -\rho_i L_i \left(\frac{dh_i}{dt} \right)_0 - F_c - Q_{sb} \tag{2}$$

where ρ_i is the sea ice density, L_i is the heat of fusion of sea ice, $\left(\frac{dh_i}{dt} \right)_0$ is the sea ice growth rate at the ice-water interface, F_c is the heat conduction, and Q_{sb} is the solar radiation at the sea ice bottom. When ice thickness $h_i > 0.5m$, Q_{sb} can be ignored, but in the Bohai Sea, the ice is very thin (usually $h_i < 0.2m$), the sea ice growing rate is affected by the solar radiation.

The simultaneous equation of equations (1) and (2) can be written as

$$\rho_w c_p C_h u_{wi} (T_w - T_m) = -\rho_i L_i \left(\frac{dh_i}{dt} \right)_0 - (F_c + Q_{sb}) \tag{3}$$

Regarding the value of C_h as a constant from time t_1 to time t_2, and integrating the equation (3), we can obtain

$$C_h = \frac{-\rho_i L_i \Delta h - \int_{t_1}^{t_2} (F_c + Q_{sb}) dt}{\int_{t_1}^{t_2} \rho_w c_p u_{wi} (T_w - T_m) dt} \tag{4}$$

where, Δh is the ice thickness change from time t_1 to time t_2, u_{wi}, T_w, T_m, F_c and Q_{sb} are

all the variables of t.

2 Calculation of Heat Transfer Coefficient in the Bohai Sea

To study the characters of sea ice growth, drifting and breakup, a field sea ice observation station is established on the JZ20-2 oil/gas platform in the Liaodong Bay. The meteorological data, oceanographic data and sea ice parameters can be measured in the winter. Moreover, the solar radiation, conductive heat flux and relative water velocity at the ice cover bottom can be calculated with a sea ice dynamic-thermodynamic model. With the data measured and calculated, the heat transfer coefficient can be determined with the equation (4).

2.1 Instrumentation on the JZ20-2 platform

The sea ice observation system on the JZ20-2 platform mainly consists of four subsystems, i.e. weather station, current meter, marine radar system and video recorders. With the weather station, air temperature, wind velocity, relative humidity, atmospheric pressure and solar radiation are recorded continuously. With the current meter, water temperature, salinity, current velocity and tidal level are recorded per 15-minute during the whole ice season. A video camera run by a computer automatically is fixed on a platform pile. When the ice cover is broken and turned up under the action of ice-broken cone, the sea ice thickness is measured with the video camera. At the same time, the sea ice type and velocity are also measured. Through the marine radar system, ice velocity, ice type can be observed. In the winter of 1997/1998, the ice season for the JZ20-2 area was about 40 days, from 8 January to 20 February 1998. In the whole ice season, air temperature, wind velocity, water temperature, water salinity, ice thickness and compactness measured with the sea ice observation system are shown in Fig.1.

2.2 Calculation of heat transfer coefficient

In the Bohai Sea, the sea ice breaks up constantly under the action of wind, current and tide, so the growth of the ice thickness is discontinuous, which will bring some trouble to the sea ice numerical simulation with a dynamic-thermodynamic model. In order to deal with the problem, the whole ice period is divided into several periods, and each one is about 3–5days, in which the influence of dynamic action is not strong, and the simulated sea ice thickness may be modified with the observed data.

With the ice thickness measured at 8:00 and 17:00 in three days from1998-01 11 to 1998 01 14, the solar radiation and the conductive heat flux at the ice-water interface, the relative velocity and temperature between ice bottom and water were calculated with the sea ice numerical model from 00:00 of 1998 01 11 to 00:00 of 1998 -01-14, and the results are shown in Fig. 4. With the equation (4), some results in the calculation process are listed in Table 1, and the mean value of the heat transfer coefficient in the three days is 0.26×10^{-3}.

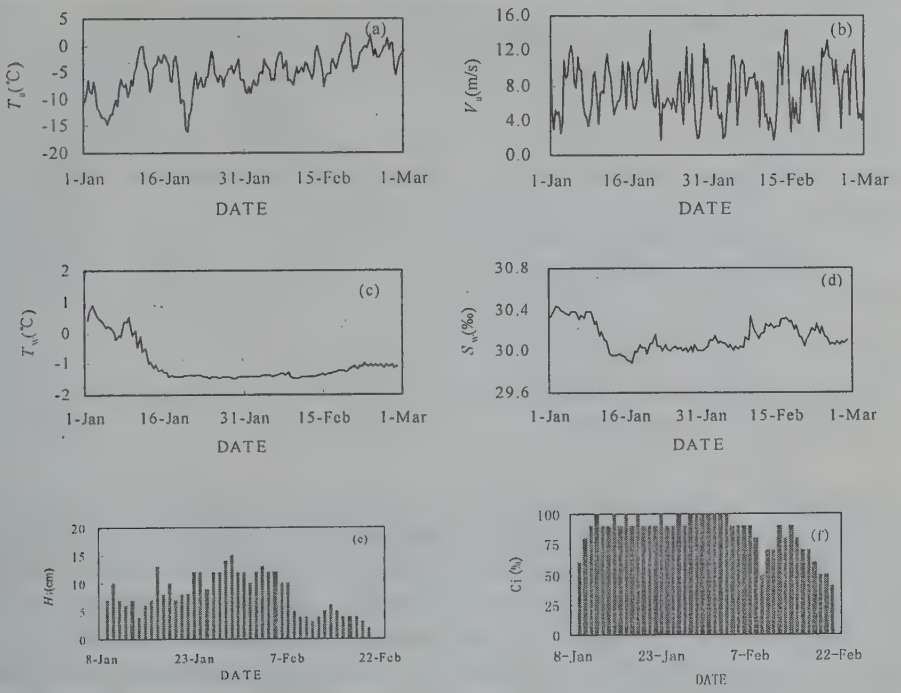

Fg. 1 Time series plots of (a) air temperature, (b)wind velocity, (c) water temperature, (d) current velocity, (e) ice thickness, (f) ice compactness measured in the JZ20-2 area in the 1997/1998 winter.

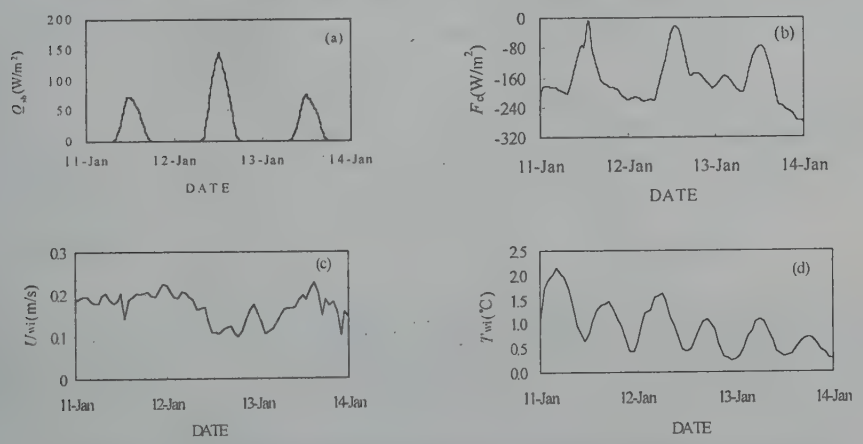

Fig. 2 Sea ice thermodynamic and dynamic factors calculated from 00:00 of 1998-01-11 to and 00:00 of 1998-01-14.

(a) solar radiation at the ice-water interface (Q_{sb}), (b) conductive heat flux at the ice-water interface (F_c), (c) relative velocity between the ice and water (U_{wi}), (d) temperature difference (T_{wi}).

Tab. 1 Some results in the calculation process for the heat transfer coefficient

DATE	TIME	h_i (cm)	Δh_i (cm)	$\int_{t_1}^{t_2} u_{wf}(T_w - T_m)dt$ ($\times 10^3$ J • m^{-2})	$\int_{t_1}^{t_2}(Q_{sh} + F_s)dt$ ($\times 10^6$ J • m^{-2})	C_h ($\times 10^{-3}$)
1998-01-11	08:00	7.0	--	--	--	--
	17:00	6.0	--1.0	5.92	--2.17	0.21
1998-01-12	08:00	8.0	2.0	6.01	--11.11	0.19
	17:00	6.5	--1.5	3.25	--0.27	0.35
1998-01-13	08:00	8.0	1.5	4.77	--9.21	0.23
	17:00	7.0	--1.0	3.99	--2.66	0.34

With the method above, the heat transfer coefficient in the winter of 1997/1998 is calculated, and the results are shown in Fig.3. In the freezing and melting periods, the heat transfer coefficient has smaller values, which were 0.16×10^{-3} and 0.04×10^{-3} respectively. In the middle of the ice season , it is up to 0.5×10^{-3}. On the basis of heat transfer coefficient determined above, the oceanic heat flux in the whole winter of 1997/1998 is calculated with bulk formula, and the results are shown in Fig. 4. The results show that the oceanic heat flux is different in the whole winter. In the freezing period, the oceanic heat flux is more than 300W/m^2, and then decreases continuously with the extension of the ice season. At the end of the ice season, it trends to zero.

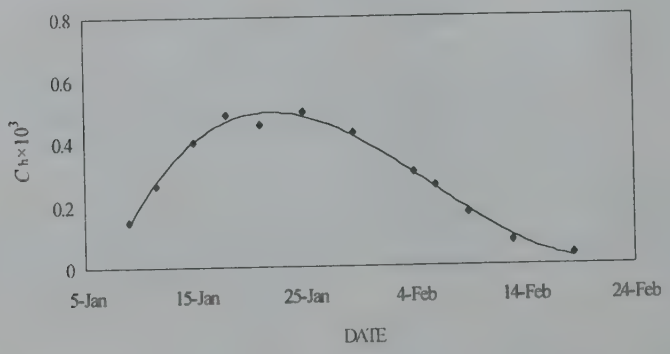

Fig. 3 Heat transfer coefficient (C_h) and its fitting curve in the winter of 1997/1998

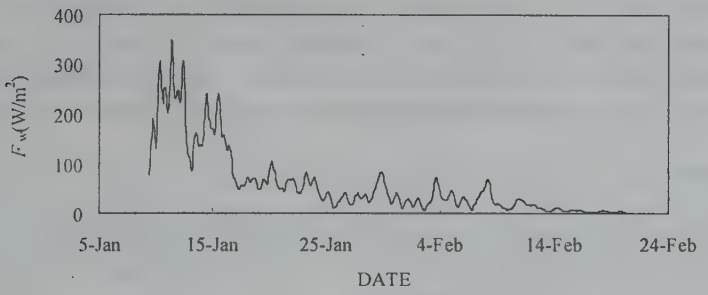

Fig. 4 Oceanic heat flux (F_w) calculated with the heat transfer coefficient in the winter of 1997/1998

3 Discussion

The heat transfer coefficient controls the value of oceanic heat flux directly, and also has great influence on the results of sea ice numerical simulation and prediction. The bulk method of oceanic heat flux is a semiempirical formula, in which the heat transfer coefficient is usually set as a constant value. In fact, the heat transfer coefficient is sensitive to ice thickness and ice roughness. From the results above, it is shown that the value of heat transfer coefficient has a smaller value in the freezing and melting periods, and in the middle ice season, it has a large value. The influences of ice thickness and ice type on the heat transfer coefficient are described as follows.

(1) Ice thickness. Under the condition of thin ice cover, the water exchanges heat with the atmosphere through ice cover easily. At the bottom of thick ice cover, the temperature gradient is lower than that of thin ice cover, which affects the heat exchange between ice cover and water. From the change of ice thickness and heat transfer coefficient of the winter of 1997/1998, we can find that the heat transfer coefficient increases with ice thickness.

(2) Ice type. The roughness of level ice, rafted ice and pancake ice is different obviously. Based on the boundary theory of ice cover, the contact area of ice and water increases with ice roughness, which causes the heat transfer sufficiently. Therefore, the heat transfer coefficient of rough ice is larger than that of smooth ice.

4 Conclusions

The heat transfer coefficient is calculated based on the sea ice dynamic-thermodynamic numerical simulation, and the meteorological data, oceaographic data and sea ice conditions measured on the JZ20-2 oil/gas platform in the Bohai Sea in the winter of 1997/1998. The results show that the heat transfer coefficient is different at different times. It is smaller in the freezing and melting periods, which is 0.16×10^{-3} and 0.04×10^{-3} respectively. In the middle of the ice season, the heat transfer coefficient has a lager value, which is about 0.5×10^{-3}. According to the heat transfer coefficient calculated in this paper, the oceanic heat flux in the winter of 1997/1998 is calculated. It is more than 300 W/m^2 in the initial ice period, and then decreases with the ice period. At the end of the ice period, it is close to zero. Based on the sea ice data measured on the JZ20-2 platform and the heat transfer coefficient determined above, it is

found that the heat transfer coefficient has close relationship with roughness and thickness of ice cover.

In the JZ20-2 sea area of the Liaodong Bay, the heat transfer coefficient has been calculated and has passed the reliability check, but its accuracy should be examined in other areas of the Bohai Sea. With further study, the oceanic heat flux of the whole Bohai Sea can be calculated with bulk formula to improve the computational precision of sea ice numerical simulation and prediction.

Acknowledgements

This project is co-sponsored by the National Foundation of Natural Science, and in part by the Bohai Offshore Oil Corporation (Grant No. 59739170). We should also thank the staff of the JZ20-2 platform for their great help in the field observation.

References

[1] Harvey L D D. (1990) Testing alternative parameterizations of lateral melting and upward basal heat flux in a thermodynamic sea ice model. *Journal of Geophysical Research*, **95** (C5): 7359-7365.

[2] Josberger E G. (1987) Bottom ablation and heat transfer coefficients from the 1983 Marginal Ice Zone Experiment. *Journal of Geophysical Research*, **92** (C7): 7012-7016.

[3] Lu Qian-Ming (1987) On Mesoscale Modeling of the Dynamics and Thermodynamics of Sea Ice, Technical University of Denmark.

[4] Lytle V I and Ackley S F. (1996) Heat flux through sea ice in the western Weddell Sea: Convective and conductive transfer processes. *Journal of Geophysical Research*, **101** (C4): 8853-8868.

[5] Maykut G A. (1986) The surface heat and mass balance. In: N. Untersteiner (Editor), *The Geophysics of Sea Ice*. Plenum New York, NY, 395-465.

[6] Mcphee M G, Maykut G A and Morison J H. (1987) Dynamics and thermodynamics of the ice/upper ocean system in the marginal ice zone of the Greenland Sea. *Journal of Geophysical Research*, **92** (C7): 7017-7031

[7] Moore R M and Wallace D W R. (1988) A relationship between heat transfer to sea ice and temperature-salinity properties of Arctic ocean waters. *Journal of Geophysical Research*, **93** (C1): 565-571.

[8] Omestedt A and Svensson U. (1992) On the melt rate of drifting ice heated from below. Cold Regions Science and Technology, **21**: 91-100.

[9] Omstedt A and Wettlaufer J S. (1992) Ice growth and oceanic heat flux: Models and Measurements. *Journal of Geophysical Research*, **97** (C6): 9383-9390.

[10] Parkinson C L and ishington W M. (1979) A large-scale numerical model of sea ice. *Journal of Geophysical Research*, 84: 311-337.

[11] Shirasawa K and Ingram G R. (1997) Currents and turbulent fluxes under the first-year sea ice in Resolute Passage, Northwest Territories, Canada Journal of Marine System, 11:21-32.

[12] Shirasawa K. Ingram G R and Hudier E J J. (1997) Oceanic heat flux under thin sea ice in Saroma-ko Lagoon. Hokkaido, Japan. Journal of Marine System, 11:9-19.

[13] Tang C L. (1991) A two-dimensional thermodynamic model for sea ice advance and retreat in the Newfoundland Marginal Ice Zone. *Journal of Geophysical Research*, **96** (C3): 4723-4737.

[14] Wang Renshu. (1984) Numerical tests of Bohai Sea ice. *Acta Oceanologica Sinica*(in Chnese), **6** (4): 572-580

[15] Wettlaufer J S. (1991) Heat flux at the ice-ocean interface. *Journal of Geophysical Research*, **96** (C4): 7215-7236.

A Method of Coding and Decoding in Underwater Image Transmission

Cheng En (程 恩)
Department of Electronic Engineering, Xiamen University, Xiamen 361005

Abstract A new method of coding and decoding in the system of underwater image transmission is introduced, including the rapid digital frequency synthesizer in multiple frequency shift keying, image data generator, image grayscale decoder with intelligent fuzzy algorithm, image restoration and display on microcomputer.

Keywords underwater image transmission, digital frequency synthesizer, frequency demodulation

The underwater acoustic channel is a very complicated time-, space-, frequency-variant channel. The variations in the acoustic velocity field, the reflection of acoustic waves on the sea bottom and surface, the attenuation of acoustic waves by the sea as well as sea noise have constituted the characteristics of the underwater acoustic channel: limited frequency bandwidth, strong multipath interference and ambient noise. The laws governing the transmission of acoustic signals in seawater are so complicated that so far no perfect mathematical models have been established for the transmission of the shallow-sea channel. In the past years, we have been conducting experimental research on underwater image transmission, have completed the experimental prototype and carried out several experiments in real ocean. The method of coding and decoding introduced in this paper is proposed in the light of the characteristics of underwater acoustic channel.

1 Composition of system

The underwater image transmission system (Fig.1) is composed of the following two parts. Underwater emitter: The underwater television camera converts the underwater images into video signals and through image digitizer data is stored in RAM. Digital frequency modulation is carried out for the digital data corresponding to the field, line and image grayscale in proper order as required by the rate of underwater image transmission and then are emitted by the transducer driven by the power amplifier. Overwater receiving part: The receiver sends the received signals, which have been pre-amplified, to the adaptive amplitude equalizer for treatment and are divided into two parts, one for field and line synchronizing signal detection and the other for image grayscale decoding in the frequency discriminator. Finally, the synchronizing signals and grayscale signals are sent to the microcomputer for image restoration and display.

Supported by Fund for University Backbone Teachers by the Ministry of Education

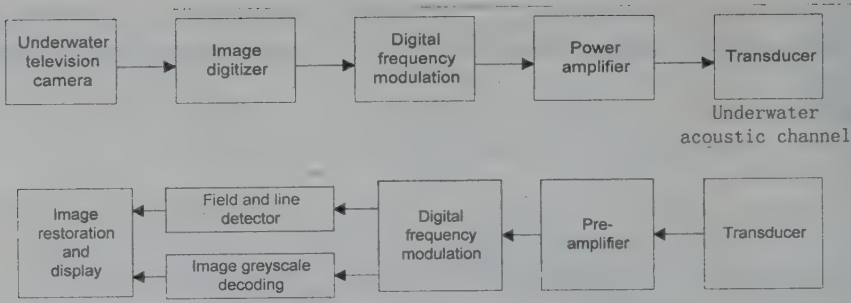

Fig. 1 Block diagram of underwater image transmission system

2 Principles

2.1 Generator of image data

For the convenience of experimental research, the grayscale images which have been digitalized are superimposed on by the field and line symchronizing information and kept in EPROM(27512). The digits corresponding to the field and line are identical, but the corresponding time widths are different, 32 and 8 pixels of time respectively. In this way the field and line synchronizing signals may be extracted through discrimination of pulse widths. The function of the image data generator (Fig.2) is to send out as required by the rate and sequence of underwater image transmission the digits corresponding to the field, line and grayscale for digital frequency modulation. Each transmitted image has 320×200 pixels and 16 levels of grayscale, on which are superimposed the field and line synchronizing information. See Fig.3 for the sequence signal of image data transmission.

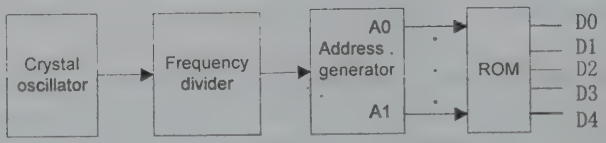

Fig. 2 Generator of image data

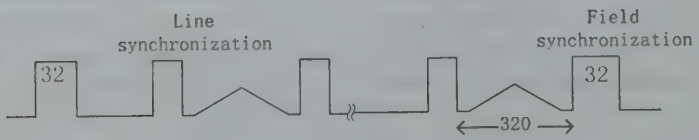

Fig. 3 Sequence signal of image data transmission

2.2 Digital frequency modulation

The general principles of multiple frequency shift keying (MFSK) are shown in Fig.4. The N outputs from the N-tuple code chip represent N information units, which are binary pulses. When the

level is "1", the gate connected to it opens and sends out the signals of the frequency corresponding to this information unit. When the level is "0", which indicates this information unit does not appear, the gate connected to it closes. As the image grayscale has 16 levels plus the synchronizing information, 17 frequencies will be required. If the MFSK is designed by directly using the method in Fig.4, the electrical circuit would be made complex and the debugging difficult, and the frequency stability of oscillators would be poor, which would inevitably bring about errors in receiving decodes.

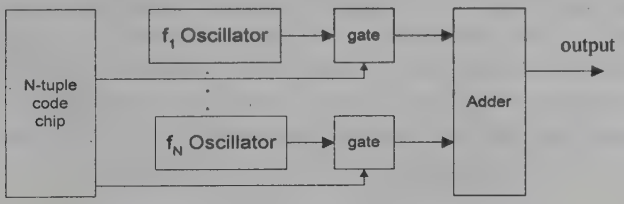

Fig. 4 Schematic diagram of MFSK producer

We therefore, put forward a new method of implementing the MFSK producer : rapid digital frequency synthesizer, which overcomes the shortcoming of slow response speed in the phase-locked frequency synthesizer. As the various frequencies are obtained from frequency divider of the crystal oscillator, they are stable. Such digital frequency modulation is mainly accomplished by the rapid digital frequency synthesizer (Fig.5) . The 8 bits presettable frequency divider is composed of two presettable reversible counters (74HC 193) connected in cascade. The A input end of the 8-bit binary digital adder (composed of two 74HC 283 in cascade connection) is connected with the frequency dividing coefficient offset switch (No) for adjusting frequency bands to satisfy the requirements of different frequency band transducers. The B input end is connected with the image digital (Nx) and its output is taken as the frequency dividing coefficient of the presettable frequency divider. The output of the frequency divider then undergoes frequency division by 2 so as to obtain symmetric square waves. The frequency output by the digital frequency synthesizer is :

$F_0=2000/(No+Nx)$ (kHz)

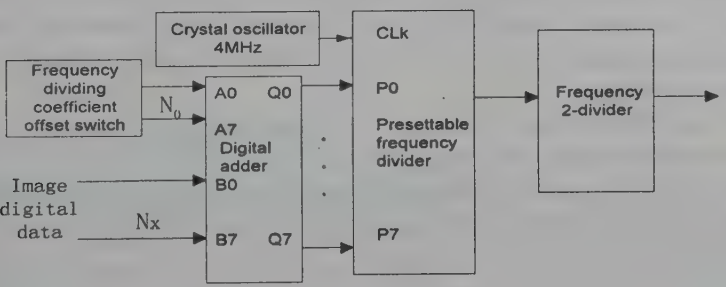

Fig. 5 Digital frequency synthesizer

2.3 Image grayscale decoding circuit

Within the width of a pixel in this system, the number of sine-wave is rather limited, so it is not appropriate to select the high-Q frequency-selecting amplifier for frequency discrimination. The low-Q frequency-selecting amplifier assisted by the fussy discrimination logic may counteract the low resolution of low Q. Therefore, we have proposed a method (Fig.6) to perform the image grayscale decoding function. The wave detector output is usually a gradually transitional smooth wave form, whose peak value has retained the amplitude information in the original transmitted wave form. The role of the sampling circuit is to extract the value at the peak time of wave form, which is provided by the bit synchronization extraction circuit. As the acoustic channel attenuation varies constantly with time and space, we have adopted the measure of discrimination level (threshold) automatic tracking, which obviously improves the reliability. The central frequencies of the 16 band pass filters (BPF) are the transmitting frequencies corresponding to the 16 levels of image grayscale.

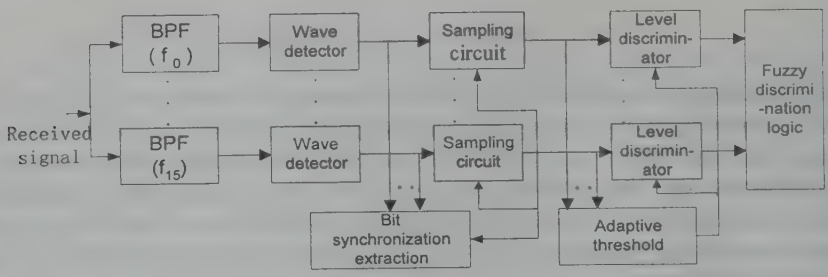

Fig. 6 Schematic diagram of frequency demodulation for MFSK

Under the ideal conditions without any interference, at a given time, at most only one group of level discriminators among the 16 groups has output in theory. But due to the multipath interference and the application of low Q frequency selecting amplifier, there often occur outputs of many adjacent groups. In the light of this, we use the probability statistics, adopt the method of intelligent fussy discrimination and take the group which may most probably occur when many groups of level discriminators have outputs simultaneously as the result of discrimination, thus raising the accuracy of decoding. Take the case where four groups of detection occur simultaneously for example. The criteria of fussy discrimination may be summed up as follows:

1) If only one group has outputs, this group is taken as the discrimination result;
2) If two groups have outputs, their average value is taken as the discrimination result;
3) If three groups have outputs, the intermediate value is taken as the discrimination result;
4) If four groups have outputs, the average value of the intermediate two groups is taken as the discrimination result.

The fuzzy discrimination logic is performed on the microprocessor, which may collect the output status of the 16 level discriminators through the programmable parallel interface and then output the discrimination result according to the status, i.e., the grayscale decoding output. It should be noted,

however, in the presence of strong interference, such decoding method is still likely to result in wrong discrimination, which are a few interference points as they are reflected on the received images.

2.4 Image restoration and display

Image restoration and display are carried out by using the IBM PC . A status input port of the PC universal printer interface receives the field and line synchronizing signals and the rest status input ports receive the binary codes (representing the 16 level grayscale information) output by the fussy discrimination logic coding. See Fig.7 for the flow chart of display program. The programs are compiled in the assembly language.

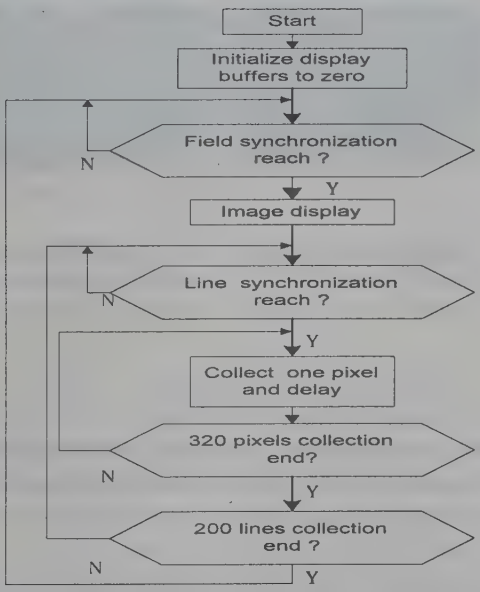

Fig. 7 Flow diagram of display program

3 Experimental results and discussion

In the underwater transmission system using this method of coding and decoding, the picture pixel is 320×200, the image grayscale 16 levels, the omni-directional transmission distance larger than 6 km and the transducer bandwidth 5kHz. The results from all the experiments conducted many times in real ocean environments have been satisfactory and the received images are reliable and clear. See Fig.8 for original image and images received from different distances.

Now we make use of an In-system programmable logic device (ISP) of Lattice Corporation to implement a rapid digital frequency synthesizer, which may reduce the volume, cut power consumption

and improve the security of the circuit itself. In order to raise the image transmission rate the image data may be compressed and coded, and then after decoding of the receiving part, decompressed and restored to images.

Fig. 8 Original image and images received from different distances

1. original image
2. image received at 4 km distance
3. image received at 7 km distance
4. image received at 10 km distance

References

[1] Behrouz Forouzan (1998) Introduction to Data Communications and Networking [M]. WCB McGraw-Hill.

[2] Schweber B. (2001) Underwater modem meets the challenge of a difficult channel-but slowly[J]. END. 39-40.

[3] Daniel B. Kilifoyle, Arthur B.(2000) The state of the art in underwater acoustic telemetry [J]. IEEE Journal of Oceanic Engineering, **25** (1): 4-27.

[4] Proakis J G Biglieri E, Shamai S. (1998) Fading channels:information-theoretic and communications aspects [J]. IEEE Trans. Information Theory. 44: 2619-2692.

[5] Crowley D. (1994) Communication Theory Today. Calif. Stanford University.

[6] Jayant N.S. (1988) Digital Coding and Waveforms: Principles and Applications to Speed and Video. New Jersey: Prentice-Hall, INC.

[7] Wooley B.A. *et al.* (1978) An integrated per-Channel PCM encoder based on interpolation, IEEE Trans. Communication, **12** (3): 272~278.

[8] Shi Guoan (1990) Ultrasonic Deep-Sea Image Transmitting System, Modern Communications, 12: 6~7.

Numerical Investigation on Submerged Horizontal Plate

Kang Haigui (康海贵)[1], Wang Ke (王 科)[2]

1 *Department of Civil Engineering, Dalian University of Technology,* Dalian 116024

2 *Graduate School of Civil Engineering, Dalian University of Technology, Dalian* 116024

Abstract Hydrodynamic characters on a horizontal, thin, rigid plate located beneath the free surface are numerically investigated. Assuming a linear, time-harmonic potential flow and utilizing Green identity, the governing Laplace equation can be simplified into Fredholm integral equation of the second kind. Supposing linear-order discontinuous elements along intersecting vertical boundaries, and by use of the boundary element method, numerical solution about source strength distribution on the plate can be changed into a series of algebraic equations. The 3D Green function is introduced to set up the integral equations, and the GMRES solver is performed for solving the large dense linear system of equations. The added-mass, damping force and exciting force are evaluated directly from the equations. It is found that the added-mass coefficient becomes negative for a range of frequencies when the plate is sufficiently close to the free surface.

Keywords Submerged plate, Dreen function, Added mass, Damping coefficient

1 Introduction

The very large floating structure (VLFS) has aroused great interest in recent years. Lots of numerical and experimental results have been obtained about the structure deformation and elevation. But from the viewpoint of stability and construction, none of these results is desirable. The reason is that the wave factor is not decelerated or eliminated before it acts on the structure and its propagating direction is also random.

The present work is to choose a system of submerged horizontal plate to take it as a model of floating breakwater to prevent the external incident waves. The idea of using the horizontal plate has many advantages:

(1) No damage to the ocean environment.

(2) Permiting water exchange from inside and out of the breakwater.

(3) Eliminating most ranges of wavelength by modifying the dimension of the plate appropriately.

(4) Easy to construct because of its simple shape.

Considering the small amplitude time-harmonic surface waves by an oscillating thin rigid plate in three dimensions, the problem is to calculate the radiated-diffracted waves and the hydrodynamic forces on the plate. If the plate lies on the free surface, such problems are known as dock problems, and circular docks have been studied by Kim[1963], Miles & Gilbert [1968], Garrett [1971]. Suppose now the plate is submerged, then we can simplify the problem to a Fredholm equation of the second kind, the unknown is ϕ : the source strength distribution over the plate (direct boundary value problem). Similar reductions have been made of the two-dimensional problem by Parsons & Martin [1992,1994]. They use the indirect boundary element method and reduce the boundary value problem to a hypersingular integral equation over the plate; the unknown is [ϕ]: the discontinuity of the potential across the plate. There is a

higher singular kernel in the integral equation and it is hard to deal with it. Also the previous work on submerged plates in three dimensions are limited to the use of matched eigenfunction expansions such as that done by Yu & Chwang [1993] for a horizontal circular plate. The eigenfunction expansion method has its own limitations, for it can only be applied to the bodies with very simple surface such as circular surface or rectangular surface and it also needs too much mathematical manipulation.

In this paper, we use the direct boundary element method with velocity potential ϕ as its unknown, which has explicit physical implications denoting the source strength distribution over the plate. Indeed, this method is very flexible and valid when a body has any smooth open bounded surface. The 3D Green function with infinite water depth and that with finite water depth have been applied respectively. Algorithms for these two kinds of Green function have been interpreted according to Newman's formulation and Seto's formulation. Numerical solutions of the new integral equation are presented.

2 Formulation

A Cartesian coordinate system is chosen, in which z is directed vertically upwards, the undisturbed free surface lying at $z = 0$. A plate, with surface S, is completely submerged beneath the free surface of the fluid D; S is a smooth closed bounded surface (see Figure 1). We consider small-amplitude time-harmonic motions. The assumptions of an inviscid , incompressible fluid and an irrotational motion can allow the introduction of a velocity potential $\mathrm{Re}\{\phi(x, y, z)e^{i\omega t}\}$ where ω is the circular frequency.

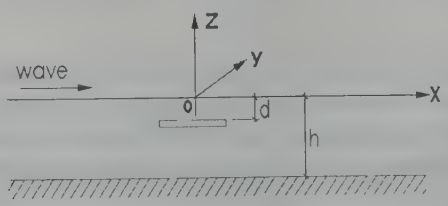

Fig. 1 Wave fluid domain

The conditions to be satisfied by ϕ are the Laplace equation,

$$\left(\frac{\partial^2}{\partial x^2}+\frac{\partial^2}{\partial y^2}+\frac{\partial^2}{\partial z^2}\right)\phi = 0 \quad \text{in fluid domain } \Omega \tag{1}$$

along with the free-surface condition

$$K\phi - \frac{\partial \phi}{\partial z} = 0 \quad \text{on } z = 0 \tag{2}$$

Where $K = \omega^2/g$ is the wave number for the deep-water depth and g is the acceleration of gravity.The scattering equation for the wave number K_0 is:

$$K = \frac{\omega^2}{g} = K_0 \tanh(K_0 h) \tag{3}$$

Where h is the water depth and k_0 is the shallow water wave number.

The bottom boundary condition of velocity potential can be expressed as:

$$\frac{\partial \phi}{\partial z} = 0, \text{ on } z = -\infty \text{ or } z = -h \tag{4}$$

The velocity potential ϕ can be expressed in the form

$$\phi = \left[(\phi_0 + \phi_7) + \sum_{j=1}^{6} i\omega X_j \phi_j \right] e^{i\omega t} \tag{5}$$

Where ϕ_0 is the incident velocity potential, ϕ_7 is the diffraction potential representing the disturbance of the incident wave by the fixed body. The indices j =1, 2, 3, 4, 5, 6 denote six conventional rigid-body motions (surge, sway, heave, roll, pitch, yaw) on the undisturbed position of the body boundary, and the radiation and diffraction potentials are subjected to the conditions:

$$\frac{\partial \phi_j}{\partial n} = n_j$$

$$\frac{\partial \phi_7}{\partial n} = -\frac{\partial \phi_0}{\partial n} \tag{6}$$

The unit normal vector n points out of the fluid domain and into the plate. In addition, ϕ must satisfy the radiation condition:

$$r^{\frac{1}{2}}\left(\frac{\partial \phi}{\partial r} - iKR\right) \to 0 \quad \text{when } r = (x^2 + y^2)^{\frac{1}{2}} \to \infty \tag{7}$$

Applying Green's theorem, we get the following well-known boundary integral equation for ϕ on S.

$$2\pi\phi(p) + \int_S \phi(q) \frac{\partial G(p,q)}{\partial n_q} ds_q = \int_S G(p,q) n_j(q) ds_q \tag{8}$$

Where $G(p, q)$ denotes Green function corresponding to a three-dimensional wave source. This equation is uniquely solvable for all values of K.

3 Formulations of 3D Green Function

3.1 Deep Water Green Function

The conventional form of Green function for infinite water depth is defined by the expression:

$$G_\infty = \frac{1}{r} + \frac{1}{r^*} + \int_0^\infty \frac{2Ke^{k(z+\zeta)}}{k-K} J_0(kR) - i2\pi K e^{K(z+\zeta)} J_0(KR)$$
$$\frac{1}{r} = \left[R^2 + (z-\zeta)^2\right]^{-1/2}$$
$$\frac{1}{r^*} = \left[R^2 + (z+\zeta)^2\right]^{-1/2}$$
$$R = \left[(x-\xi)^2 + (y-\eta)^2\right]^{1/2} \tag{9}$$

Where (x, y, z) is the field point, (ξ, η, ζ) is the source point. $J_0(.)$ denotes the zero-order Bessel function of the first kind , the integration path in Eq. (9) is indented below the pole of the integrand at $k=K$, so that G_∞ can satisfy the radiation condition.

Following Newman's method, and by use of the nondimensional coordinates $X=KR$, $Z=-K(z+\zeta)$,

the principal integral in Eq. (9) can be transformed as follows:

$$A(X,Z)=\int_0^{\infty}\frac{2Ke^{k(z+\zeta)}}{k-K}J_0(kR)dk$$
$$=-\pi Ke^{K(z+\zeta)}\left[H_0(KR)+Y_0(KR)\right]-2Ke^{K(z+\zeta)}\int_0^{-K(z+\zeta)}\frac{e^{\tau}}{\left[\tau^2+(KR)^2\right]^{1/2}}d\tau$$
$$=-\pi Ke^{-Z}\left[H_0(X)+Y_0(X)\right]-2Ke^{-Z}F(X,Z) \qquad (10)$$

In which $\boldsymbol{H}_0(.)$ is the Struve function of the order zero and $\boldsymbol{Y}_0(.)$ is the Bessel function of the second kind, while

$$F(X,Z)=\int_0^{-K(z+\zeta)}\frac{e^{\tau}}{\left[\tau^2+X^2\right]^{1/2}}d\tau$$
$$=J_0(X)\left[\log(Z+(Z^2+X^2)^{1/2})-\log(X)\right]+\frac{\pi H_0(X)}{2X}\left\{(Z^2+X^2)^{1/2}-X\right\}$$
$$+\sum_{m=1}^{\infty}\frac{1}{(2m)!}\overline{F}_{2m}(X,Z)+\frac{1}{(2m+1)!}\overline{F}_{2m+1}(X,Z) \qquad (11)$$

Where $\overline{F}_{2m}(X,Z)$ and $\overline{F}_{2m+1}(X,Z)$ are calculated by the recursive relationship below, respectively.

$$2m\overline{F}_{2m}(X,Z)+(2m-1)X^2\overline{F}_{2m-2}(X,Z)=Z^{2m-1}(Z^2+X^2)^{1/2}\quad \overline{F}_0=0,\overline{F}_2=\frac{1}{2}Z(Z^2+X^2)^{1/2}$$
$$(2m+1)\overline{F}_{2m}(X,Z)+2mX^2\overline{F}_{2m-1}(X,Z)=Z^{2m}(Z^2+X^2)^{1/2}\quad \overline{F}_1=0,\ \overline{F}_3=\frac{1}{3}Z^2(Z^2+X^2)^{1/2} \qquad (12)$$

Thus, the deep water Green function can be calculated very fast and accurately owing to the rapid convergence of the series expression.

3.2 Shallow Water Green Function

In a fluid of constant finite depth h, the Green function can be expressed in terms of a contour integral form:

$$G=\left[R^2+(z-\zeta)^2\right]^{-1/2}+\left[R^2+(z+\zeta+2h)^2\right]^{-1/2}$$
$$+2\int_0^{\infty}\frac{(k+K)\cosh\left[k(z+h)\right]\cosh\left[k(\zeta+h)\right]}{k\sinh(kh)-K\cosh(kh)}e^{-kh}J_0(kR)\,dk \qquad (13)$$

or, John's infinite-series expansion:

$$G=2\pi\frac{K^2-K_0^2}{K_0^2h-K^2h+K}\cosh\left[K_0(z+h)\right]\cosh\left[K_0(\zeta+h)\right]\left[Y_0(K_0R)+iJ_0(K_0R)\right]$$
$$+4\sum_{n=1}^{\infty}\frac{k_n^2+K^2}{k_n^2h+K^2h-K}\cos\left[k_n(z+h)\right]\cos\left[k_n(\zeta+h)\right]K_0(k_nR) \qquad (14)$$

In Eq. (14) the wave number K_0 can be obtained from Eq. (3), and k_n denotes the set of corresponding imaginary roots, defined more explicitly as the positive real root of the equation $k_n\tan(k_nh)=-K$, $n=1,2,3,\ldots$ $\boldsymbol{K}_0(.)$ is the modified Bessel function of the second kind.

If we want to use Eq. (14) to evaluate the value of integral equation, for larger R, this orthogonal eigenfunction expansion can converge very fast with accurate values especially close to the free surface.

But in the vicinity R =0, owing to the logarithmic singularities of $Y_0(.)$ and $K_0(.)$, it converges very slowly and needs too many series terms and, viewed from the angle of numarical calculation, it is inefficient. Here Eq.(13) may be used to evaluate Green function for smaller R, and an alternative form of Eq. (13) has been given by Seto[1992, 1993]:

$$G = \mathrm{Re}[G_\infty] + (\mathrm{Re}[G] - \mathrm{Re}[G_\infty]) - i\frac{2\pi K_0^2}{h(K_0^2 - K^2) + K}\frac{\cosh[K_0(\zeta + h)]}{\cosh(K_0 h)}\frac{\cosh[K_0(z + h)]}{\cosh(K_0 h)}J_0(K_0 R)$$

$$= \frac{1}{r} + \frac{1}{r^*} + \int_0^\infty \frac{2Ke^{k(z+\zeta)}}{k - K}J_0(kR)dk + \sum_{n=0}^{\infty}\frac{1}{(2n)!\,h}\left[\left\{C_{2n+2}^{(2)}(V) - V^2 C_{2n}^{(2)}(V)\right\}\left(\frac{r}{h}\right)^{2n}P_{2n}(\cos\theta)\right.$$

$$\left. + \frac{2VC_{2n+2}^{(2)}(V)}{2n+1}\left(\frac{r^*}{h}\right)^{2n+1}P_{2n+1}(\cos\theta^*) + \left\{C_{2n+2}^{(2)}(V) + V^2 C_{2n}^{(2)}(V)\right\}\left(\frac{r^*}{h}\right)^{2n}P_{2n}(\cos\theta^*)\right]$$

$$- i\frac{2\pi K_0^2}{h(K_0^2 - K^2) + K}\frac{\cosh[K_0(\zeta + h)]}{\cosh(K_0 h)}\frac{\cosh[K_0(z + h)]}{\cosh(K_0 h)}J_0(K_0 R) \qquad (15)$$

Where Re[G] means the real part of G and $V = Kh$, $P(.)$ is the zero-order Legendre function of the first kind.

$C_m^{(2)}(V)$ is the principal integral independent of the space variables and depends only on V as defined below:

$$C_m^{(2)}(V) = \int_0^\infty \frac{u^m e^{-u}}{(u - V)[u\sinh(u) - V\cosh(u)]}du \qquad m > 0 \qquad (16)$$

$C_m^{(2)}(V)$ can be evaluated fast and accurately following the numerical scheme in the appendix of this paper. Also it is useful to have a table of $C_m^{(2)}(V)$ as 1D block data for practical applications.

In order to get a robust shallow water Green function with high convergence, the switching method (integral form and series form) is utilized. 16D accuracy has been achieved for the wave number K_0 and subroots wave number K_n has at least 16D accuracy with a total of 4 000 terms while $C_m^{(2)}(V)$ in Eq. (16) has a total of 36 terms.

4 Hydrodynamic Forces

Once ϕ has been solved from Eq. (8), the added-mass coefficients and damping coefficients can be given by:

$$a_{ij} + i\frac{b_{ij}}{\omega} = \rho\int_{S_0}\phi_i\frac{\partial\phi_j}{\partial n}ds \qquad i, j = 1,2, \cdots, 6 \qquad (17)$$

and the wave exciting forces by

$$F_\omega = \rho i\omega\int(\phi_0 + \phi_7)n_i ds \qquad i = 1,2, \cdots 6 \qquad (18)$$

while ϕ_7 can also be solved by use of the Green function method if we substitute $\partial\Phi_7/\partial n = -\partial\Phi_0/\partial n$

on the right hand side of the Eq. (8).

5 Boundary element analysis and GMRES solver

It is well known that an initial boundary value problem can be solved by its corresponding boundary value problem. In this paper, linear-order element is introduced to perform this task, the discontinuous elements are used along the intersection line of the plate edge, where dot lines denote geometry boundary and solid lines denote boundary elements, control points are located at each node of the triangular. The freedom nodes are located at 2/3-element size for all kinds of discontinuous elements (see Fig. 2). Since the solving linear system of equations is large, a fast iterative solver is strongly demanded, the generalized minimal residual (GMRES) algorithm which was firstly proposed by Saad and Schultz (1986) is utilized here. This algorithm first constructs an orthonormal basis by using the Arnoldi process and the norm of the residue vector is minimised in each iteration step on Krylov subspace. Suppose linear system of equations $Ax = f$, where A is a matrix of $n \times n$, x is $n \times 1$, f is $n \times 1$, the procedure can be briefly summarized as follows:

(1) Start: Choose x_0 and compute $r_0 = f - Ax_0$ and $v_1 = r_0 / \| r_0 \|$.

(2) Iterate: For $j = 1, 2, \cdots, m$ do:

$$h_{i,j} = (Av_j, v_i), \quad i = 1,2,\ldots, j,$$

$$\hat{v}_{j+1} = Av_j - \sum_{i=1}^{j} h_{i,j} v_i,$$

$$h_{j+1,j} = \left\| \hat{v}_{j+1} \right\|, \quad \text{and}$$

$$v_{j+1} = \hat{v}_{j+1} / h_{j+1,j}$$

(3) Form the approximate solution

$$x_m = x_0 + V_m y_m \quad \text{where} \quad y_m \text{ minimizes} \quad \left\| \beta e_1 - \overline{H}_m y \right\|, \ y \in R^m$$

(4) Restart:

Compute $r_m = f - Ax_m$; if satisfied then stop

or else, compute $x_0 = x_m$, $v_1 = r_m / \| r_m \|$ and go to 2

The successive QR factorization can be effectively utilized in the minimization procedure. Numerical experiment shows that this kind of GMRES solver with diagonal preconditioner is faster than the direct solver for a large matrix and also has good convergence characteristics.

Fig. 2 Boundary element and collocation points

6 Results and Discussion

6.1 Results of Heaving Plate

Using the above-mentioned Green functions, we consider the hydrodynamic forces acting on a submerged floating plate with longitude L=2.0m, breadth B =2.0m, thickness T=0.005m and submergence d. (see Figure 1).

Figures 3, 4 show the added-mass and damping coefficients as a function of $K * L/2$ for two depths of submergence d =−10cm, d =−5cm when the plate has a vertical oscillation (heaving mode with n_j =1). In these two figures we notice the occurrence of negative added mass for sufficiently small d and with increasingly sharp maxima and minima. It can also be observed that the higher peak of the added mass is accompanied by a large peak of the damping coefficients. This can be confirmed by the Kramers -Kronig relations.

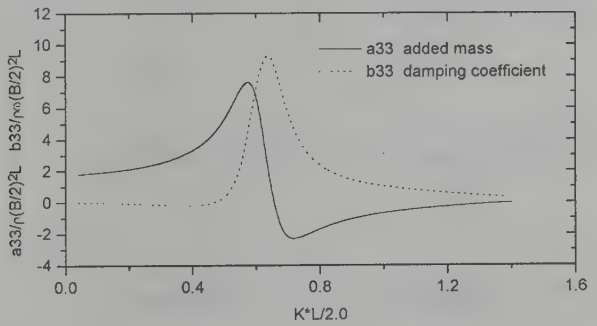

Fig. 3 Added mass and damping coefficient, d =10cm

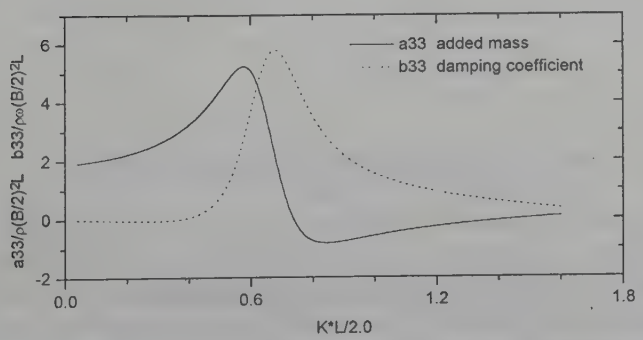

Fig. 4 Added mass and damping coefficient, d = 5cm

Physically, the damping coefficient is proportional to the velocity of the body, and the added mass coefficient is proportional to the acceleration of the hydrodynamic force acting on the oscillating horizontal plate. When the submergence is small and the width of the shallow region on top of the plate is large, near the zero point of added mass, the added mass coefficient will vary rapidly from maximum to minimum and be accompanied by a large peak damping coefficient with a little phase lag. This causes the hydrodynamic forces related with the added mass and the damping coefficient to offset each other and the drastic resonant motion to occur. These frequencies are called resonant frequencies. Also when the submergence becomes shallower, larger added mass and damping coefficient could be obtained with the resonant frequency shifted. (See Figures 5, 6)

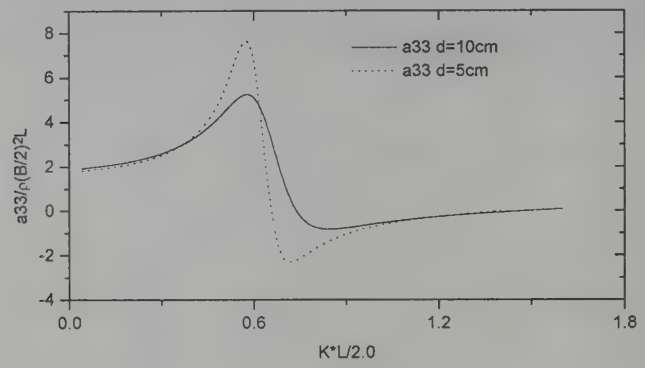

Fig. 5 Comparisons of added mass in deep water

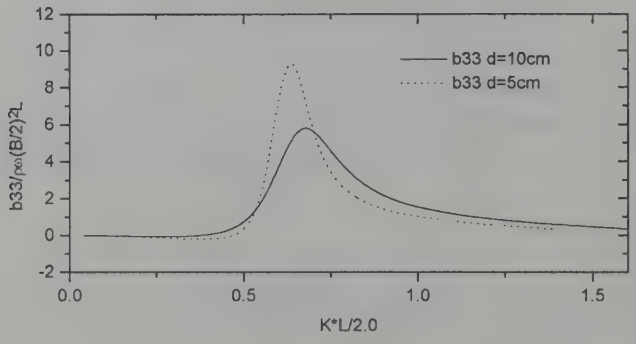

Fig. 6 Comparisons of damping coefficient in deep water

If we expand our calculation to the shallow water with water depth h =5m, a similar trend of negative added mass and sharp variation of damping coefficient can be observed (Figures 7, 8), but in

this case the two curves have almost the same value and the resonant frequency is just like the deep water case. From these results we can conclude that the shallow water effect can be neglected when the plate is fully submerged and close to the free surface, and that the resulting vertical hydrodynamic force is associated only with the flow in the shallow region on top of the plate. Figures 9, 10 show the results of wave exciting forces for heave and pitch respectively while h = 5m, d = 10cm.

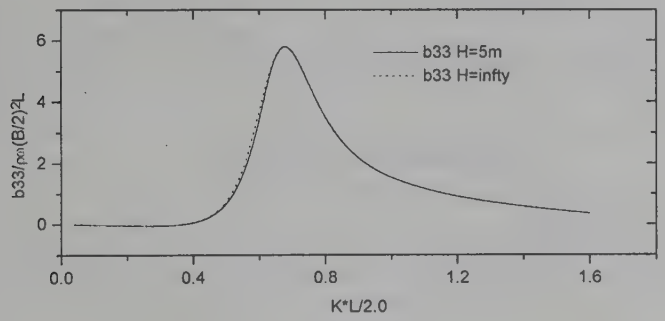

Fig. 7 Comparisons of added mass, d = 10cm

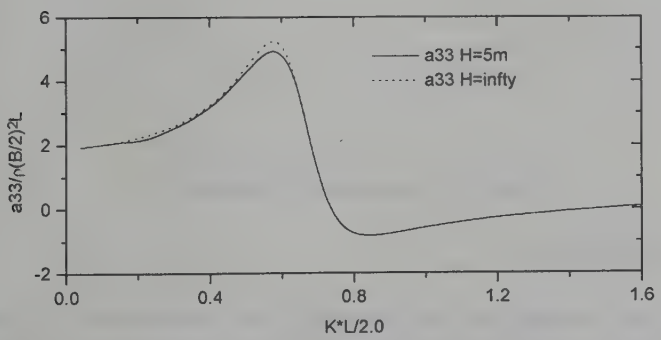

Fig. 8 Comparisons of damping coefficient, d = 10cm

Another interest shall be focused on the comparisons with the results when the plate is on the free surface, the so-called dock problem. According to the results calculated by Yamashita [1979], in the low frequency range the added mass coefficient goes into infinity and the shallow water effect can not be neglected in this case, while for a fully submerged plate, in the range of low frequency, the logarithmic singularity in Green function has been cancelled by top and bottom of the submerged body surface, thus constant added mass coefficient and zero damping can be obtained in the low frequency limit.

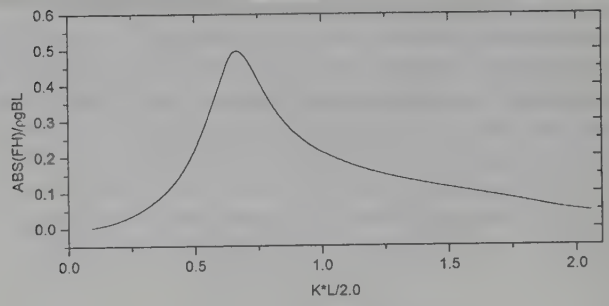

Fig. 9 Wave exciting force for heave

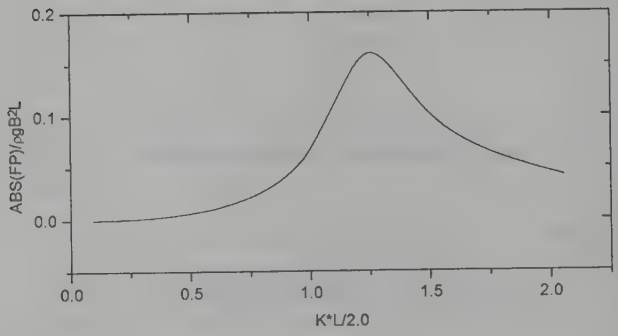

Fig. 10 Wave exciting force for pitch

7 Conclusion and Remarks

The 3D Green function method has been introduced in the present work and the integral equation has been solved numerically using a boundary element method. Actually this method is very flexible and valid for any kind of body shape.

Negative added mass occurs when the plate is very close to the free surface, the resulting added mass and damping coefficient are associated only with the shallow region above the plate, the water depth effect can be neglected for a fully submerged plate very close to the free surface.

In the practical calculation, as the submerged horizontal plate is rather thin, the wave pressure acting on the edge side of the plate can be regarded as a constant value. This corresponds to the equal velocity potential on the edge side, and then after introducing this condition, much computer time of matrix installing will be saved.

References

[1] Kim, W, D . (1963) The pitching motion of a circular disk. *J. Fluid Mech.*, 17, 607-629.

[2] Miles, J. & Gilbert, F. (1968). Scattering of gravity waves by a circular dock. *J. Fluid Mech.*, 34 783- 793.

[3] Garrett, C.J.R (1971) Wave forces on a circular dock. *J. Fluid Mech.* 46, 129-139.

[4] Parsions, N.F.& Martin, P.A. (1992) Scattering of water waves by submerged plates using hypersingular integral equations. *Appl.Ocean Res.* 14, 313-321.

[5] Parsions, N.F.& Martin, P.A. (1994) Scattering of water waves by submerged curved plates and by surface-piercing flat plates. *Appl. Ocean. Res.* 16, 129-139.

[6] Yu, X. & Chwang, A.T. (1993) Analysis of wave scattering by submerged circular disk. *J. Engng Mech.* 119, 1804-1817.

[7] Newman, J.N. (1985) Algorithms for the free-surface Green functions, Jour, and Eng. Math.19.

[8] Seto, H (1991) Efficient evaluation of some singular integrals appearing in multipole expansions in water of finite depth, Trans. of the west-Japan soc. of naval arch., N0.83.

[9] Seto, H (1992)Some expressions of pulsating source potentials in shallow water and their efficient algorithms. Trans. of the West-Japan Soc. of Nav. Arch., No. 85.

[10] Yamashita, S. (1979) Motions and Hydrodynamic pressures of a box-shaped floating structure of shallow drift in regular waves. J.Soc.of Nav. Arch. of Japan, **146**: 165-172.

[11] Saad and Schultz. (1986) GMRES: a generalized minimal residual algorithm for solving nonsymmetric linear systems. SIAM J.Sci.Stat.Comput. **7** (3), July.

Chemical Fluxes of Asian Rivers into Oceans and their Controlling Factors*

Yang Shouye (杨守业), Li Congxian (李从先) and Liu Shuguang (刘曙光)

Laboratory of Marine Geology, Tongji University, Shanghai 200092

Abstract Chemical fluxes of Asian rivers into oceans bear different regional variations. Three zones are characteristic of distinct dissolved sediment loads and yields and ionic concentration. Rivers into oceans in China play an important role in Asia because of their different chemical fluxes, among which those draining the Loess Plateau have high ionic concentration, low water discharges and dissolved sediment loads and yields.

Climate, vegetation, soil and strata lithology, chemical weathering intensity and tectonic activity dominate chemical fluxes of Asian rivers into oceans, and different factors have different effects on the chemical fluxes of separate regional rivers. Rising of the Tibet Plateau also exerts an important influence on chemical compositions of rivers originating from it.

Keywords Chemical flux, Asian rivers into ocean, controlling factors

1 Introduction

Most Asian rivers into oceans are located in 10.3°N~73°N, 24°E~161°E, and their river basins cover tropical, semitropical, warm-temperate, temperate and frigid zones, respectively. They mainly flow into the Arctic Ocean, the Pacific Ocean and the Indian Ocean, whereas the Indus River enters the Arabian Sea. Those rivers located in South Asia and East Asia originate from the Himalayas which is the highest mountain in the world, and flow into oceans with huge fall. The Ganges / Bramaputra rivers contain the largest water discharge and sediment load in these rivers, and the Changjiang River with an annual water discharge of $9\ 300 \times 10^8 m^3$ takes the second place. The Huanghe River yields one billion tons of sediment on average of many years, and the total sediment load of the Huanghe and the Ganges/ Bramaputra rivers occupies 20% of that carried by world rivers into oceans, and further more, those rivers in South Asia and around the Pacific and the Indian Oceans carry 70% of the sediment load by world rivers (Milliman and Meade, 1983).

Due to the importance of Asian rivers into oceans in world rivers, sediment and water discharges of these rivers are widely documented, but their chemical fluxes are less studied and reviewed. Although detrital and dissolved chemical compositions of some rivers in China are often studied, comparative study of the chemical fluxes of Asian rivers into oceans and their controlling mechanisms has not been reported (Huang and Zhang, 1994; Zhang *et al.*, 1990, 1992; Li *et al.*, 1984; Qu *et al.*, 1984; Zhao and Yan, 1992; Wang, 1995; Yang and Li, 1999; Zhang and Huang,1990). This paper comparatively studies the chemical fluxes of most Asian rivers into oceans and further discusses the controls of climate, vegetations, soil, strata, weathering and tectonic activities.

* Project supported by the National Natural Science Foundation of China (Grant No. 49976016)

2 Chemical fluxes of Asian rivers into oceans

Study shows that dissolved sediment loads of Asian rivers gradually decrease from low latitude to high latitude(Table 1), and according to dissolved sediment loads, ionic concentrations and dissolved sediment yields, Asian rivers can be divided into three regions. The first region mainly refers to those rivers located at 37°N southward, and these rivers have the highest dissolved sediment loads and yields; The second region contains rivers between at 37°N and 41°N which have low dissolved sediment loads and yields, but the highest ionic concentrations and turbidities, and the ratios of dissolved sediment loads to total chemical loads are the lowest in Asian rivers; The third region includes subarctic-arctic rivers which universally have the lowest dissolved sediment loads and yields and ionic concentrations, but the dissolved sediment loads occupy a major part of the total chemical loads.

Dissolved sediment loads of South Asian rivers are all beyond 50×10^9kg/a and vary little with an average of 79×10^9kg/a; Rivers into oceans in China have largely variably dissolved sediment loads, in which the Changjiang River bears the highest, reaching 153×10^9kg/a, and other rivers less than 50×10^9kg/a, especially the Dalinghe River reaching the lowest, up to 1×10^9kg/a. The Lena River in subarctic-arctic rivers has the highest dissolved sediment loads of 85×10^9kg/a. Based on ionic concentrations, rivers lying in 37°N~41°N in China, including the Huanghe, Haihe, Dalinghe and Liaohe rivers, yield large values with an average of 433g / m^3, and the Honghe River has the highest ionic concentration of 569g/m^3 while other rivers mostly have values below 200g /m^3, and the subarctic-arctic rivers yield the lowest concentration with an average of 98g / m^3.

Dissolved sediment yields of Asian rivers also gradually decrease from low latitude to high latitude (Table 1, Fig.1). The South Asian rivers have large yields with an average of 178×10^3 kg / km^2a, and the Honghe River reaches the highest among Asian rivers, achieving 583×10^3 kg / km^2a. Average dissolved sediment yields of rivers into oceans in China is 52×10^3 kg / km^2a, while the subarctic-arctic rivers bear

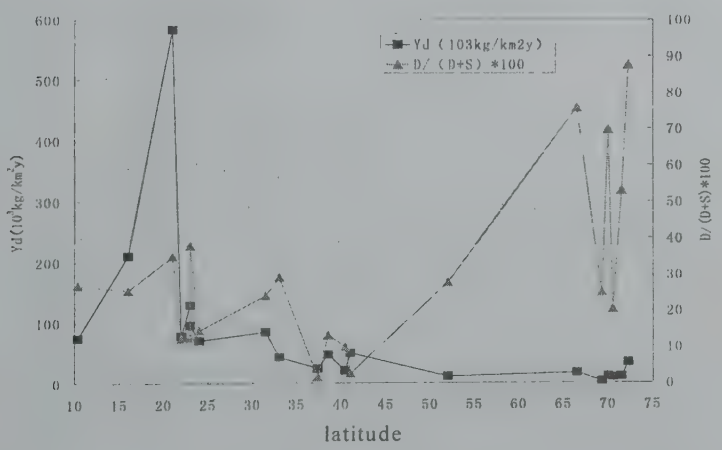

Fig. 1 Variation with altitude of dissolved sediment yields(Yd) and D/(D+S) of Asian rivers

the lowest with an average of 14×10^3kg / km^{2}a. Comparatively, the ratios of dissolved sediment loads to total chemical loads (denoted by D/ (D+S) $\times$100) show different change trends (Table 1, Fig.1). The ratios in the Ganges/Buramaputra Rivers are about 12~15%, close to that in the Indus River, and rangefrom 27% to 35% in other South Asian rivers. The Huanghe, Haihe, Liaohe and Dalinghe rivers in North China yield D/(D+S) less than 15%, in which the Huanghe River attains only 2%, the lowest in Asian rivers, whereas the Pearl River has the highest ratio among the rivers in China, reaching 38%. The ratios of subarctic-arctic rivers vary markedly, from 20% to 88% with an average of 51%, obviously higher than those of South Asian rivers and most rivers in China. Therefore, all dissolved sediment loads of South Asian and East Asian rivers are lower than detrital sediment loads, whereas most subarctic-arctic rivers are to the contrary, with dissolved loads higher than detrital sediment loads, in which the Lena River is the most obvious and the dissolved load is 7 times the detrital sediment load.

Studies also reveal that, with increasing annual temperatures of river basins, ionic concentrations and dissolved sediment yields increase gradually in Asian rivers, and their correlation coefficient(R) is 0.53, while D/(D+S) gradually decreasess with R of−0.53. Similarly, with the increase of precipitation, the dissolved sediment yields also increase gradually, and the value of R reaches 0.50, while D/(D+S) gradually decreases with R value of −0.34 (Fig.2). Comparatively, variation of ionic concentration with precipitation is not obvious. Dissolved sediment yield also increases with increasing runoff, and the value of R is 0.75, but ionic concentration and D/(D+S) vary unobviously with runoff.

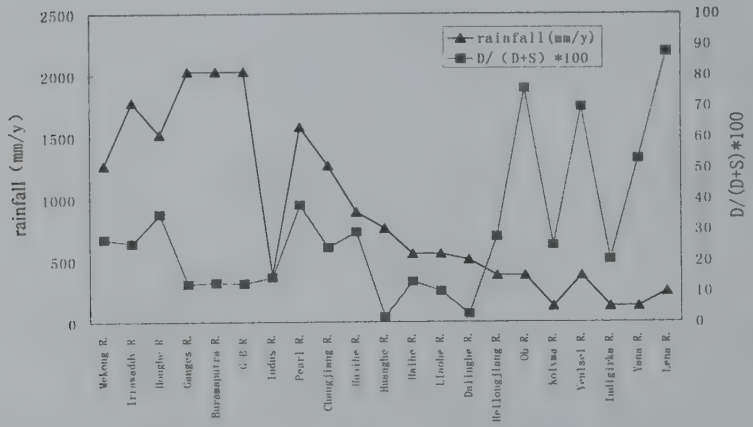

Fig. 2 Variation of precipitation and D/(D+S) of Asian rivers into oceans

Tab. 1 Chemical fluxes of major Asian Rivers into oceans (data from Zhang J., 1997; Hay, 1998; Milliman and Meade, 1983)

River	North latitude	East longitude	Area (km^2)	Precipitation (mm/y)	Runoff (mm/y)	Water discharge ($10^8m^3/y$)	T (℃)	IC (g/m^3)
Mekong R	10.33	105	0.79	1 270	595	470	21	126
Irrawaddy R.	16	95	0.432	1 780	991	428	24	213
Honghe R.	21	106	0.12	1 520	1025	123	24	569
Ganges	22	88	0.98	2 030	373	590	21	124
Buramaputra R.	23	91	0.61	2 030	951	630	15	126
G/B R.	22		1.59	2 030	611	971	18	157
Indus R.	24	68	0.96	380	248	238	24	286
Pearl R.	23	113	0.44	1 580	686	302	21	140
Changjiang R.	31.48	121	1.8	1 270	500	900	16	170
Huaihe R.	33	118.3	0.27	894	239	65		80
Huanghe R.	37.32	118.19	0.75	760	65	49	13	372
Haihe R.	38.5	118	0.26	556	88	23		538
Liaohe R.	40.4	122	0.22	556	66	15	7	315
Dalinghe R	41	121	0.02	508	98	1.96		510
Heilongjiang	52	141	1.85	380	189	350	−1	57
Ob' R.	66.5	68	2.98	380	129	385	−1	130
Kelyma R.	69.3	161	0.644	130	110	71	−9	28
Yenisei R.	70	86	2.58	380	217	560	−7	54
Indijirka R.	70.5	149	0.36	130	153	55	−12	65
Yana R.	71.5	135	0.318	130	91	29	−15	121
Lena R.	72.25	126.4	2.49	250	206	514	−9	165

River	Turbidity (g/m^3)	S (109kg/y)	D (109kg/y	Ys ($10^3kg/km^2y$)	Yd ($10^3kg/km^2y$)	D/ (D+S) *100	D/S* 100	Yd/Ys* 100
Mekong R.	340	160	59	202.5	74.7	27	37	0.4
Irrawaddy R.	619	265	91	613.4	210.6	26	34	0.3
Honghe R.	1057	130	70	1083.3	583.3	35	54	0.5
Ganges	881	520	73	530.6	78.0	12	14	0.1
Buramaputra R.	857	540	79	885.2	130.0	13	15	0.1
G/B R.	1092	1060	152	666.7	95.6	13	14	0.1
Indus R.	1681	400	68	416.7	70.8	15	17	0.2
Pearl R.	228	69	42	156.8	96.1	38	61	0.6
Changjiang R.	533	480	153	266.7	85.0	24	32	0.3
Huaihe R.	193	12.48	5.16	104.0	43.0	29	41	0.4
Huanghe R.	22449	1100	18	1466.7	24.3	2	2	0.02
Haihe R.	3540	81	12	311.5	47.3	13	15	0.2
Liaohe R.	2819	41	4.6	186.4	20.8	10	11	0.1
Dalinghe R	18367	36	1	1800.0	50.0	3	3	0.03
Heilongjiang	149	52	20	28.1	10.8	28	38	0.4
Ob' R.	42	16	50	5.4	16.8	76	313	3
Kelyma R.	85	6	2	9.3	3.1	25	33	0.3
Yenisei R.	23	13	30	5.0	11.6	70	231	2
Indijirka R.	255	14	3.6	38.9	10.0	20	26	0.3
Yana R.	107	3.1	3.5	9.7	11.0	53	113	1.1
Lena R.	23	12	85	4.8	34.1	88	708	7.1

Note: D denoting water discharge; S showing sediment loads; Ys showing detrital sediment yields; Yd showing dissolved sediment yields; T denoting temperature; IC showing ionic concentration.

3 Characteristics of chemical composition in rivers into oceans in China

Rivers into oceans in China occupy an important position in world rivers, and especially those draining the Loess Plateau or northwestern plateau, such as the Huanghe, Liaohe, Haihe and Dalinghe rivers, have higher turbidity with an average of 11.79×10^3 g/m^3, more than that of the Changjiang and Pearl rivers with an average of 0.38×10^3 g/m^3 and other Asian rivers. Detrital sediment yields of both the Huanghe and Dalinghe rivers are above $1\,000 \times 10^3$kg/km^{2}a, obviously higher than that of other Asian rivers, and their ionic concentration average is 433g/m^3, 2.6 and 3.1 times that of the Changjiang River and the Pearl River, respectively. Due to low water discharge(less than 100km^3/a), dissolved sediment loads and yields of these rivers are distinctly lower than those of the Changjiang and Pearl rivers, and D/ (D+S) is 7% on average, also lower than that of the Changjiang (24%) and Pearl River (38%), and the Huanghe River has the lowest ratio, only 2%.

According to ionic composition, PHs of the rivers in 37°N~41°N are more alkaline with high alkali- and alkali earth element contents, including Ca^{2+}, Mg^{2+}, Na^+, K^+, and main anions are Cl^- and SO_4^{2-}, reflecting strong salt weathering in the river basins. Salinity and ionic contents in the Huanghe River are the highest in large rivers in China. Comparatively, the Changjiang River dominated by high Ca^{2+} and HCO_3^- and (Ca+Mg) / (K+Na), low Na / Cl, is characterized by strong carbonate weathering (Huang and Zhang, 1994; Zhang *et al.*, 1992; Wang, 1995; Zhang and Dong,1990). PH of the Pearl River is far lower and alkali metals bear low contents, and Ca^{2+} and HCO_3^- are high as compared with the Changjiang River (Zhang and Dong, 1990; Xu, 1994, 1996). Ionic concentration in the Huaihe River lies between those of the Changjiang and the rivers in North China.

Elemental compositions of detrital sediment show distinct change from rivers in South China to those in North China. Alkali- and alkali earth elements in the Huanghe river sediment such as Na, Ca, Sr and Ba yield high contents, but trace element contents are very low. The Changjiang River has higher K and Mg contents and trace elements than the Huanghe River, especially those transitional metals. The Pearl River has the lowest alkali- and alkali earth elements contents, but the highest contents of Fe, Ti and Al, while most trace element contents are close to those of the Changjiang River (Li *et al.*,1984; Qu *et al.*, 1984; Zhao and Yan, 1992, 1994; Yang ang Li, 1999; Zhang and Huang, 1993).

4 Controlling factors of chemical fluxes

Chemical fluxes of Asian rivers into oceans are closely related to climate, vegetation, soil, strata, weathering and tectonic activity, and different factors have different effects on chemical fluxes of separate regional rivers. From South Asian rivers in low latitude to subarctic-arctic rivers in high latitude, the river basins cover different climate zones, and the annual temperature averages decrease from 24℃ to -15℃, and the annual precipitation from 2 030mm to 130mm. Variations of precipitation and temperature are closely related to chemical weathering in river basins. Because of high precipitation and temperature in south Asia area, runoffs of rivers are very large and this strengthens chemical weathering and mineral dissolution. In addition, due to abundant rainfall and vegetation, solution in soil approximates acidic and CO_2 is high, so this will be in favor of the minerals' breaking down and the elements' eluviating, thus resulting in higher dissolved sediment loads and yields in these south Asian rivers than those in other Asian rivers. Therefore, chemical fluxes of these rivers are mainly controlled

by climate and chemical weathering. In spite of low water discharge of the Honghe River, easily dissolved salt strata well developed in the river basin might bring about the highest ionic concentration and dissolved sediment yields in Asian rivers, and its ionic concentration is 2~4 times that of other south Asian rivers and dissolved sediment yield 8 times that of the Indus River.

The Pearl River is located in the tropic and humid zone, and its vegetation type is the evergreen broadleaf which belongs to the tropical rain forest. Differences of temperature in a day and in a year are both small, and abundant rainfall leads to high runoff, up to 686mm/a. Physical weathering is very weak in the drainage basin because of vegetation protection, and sediment concentration and detrital sediment yield are rather low in rivers. On the contrary, chemical weathering is very strong because of the widely distributed carbonate rocks in river basins, which results in the highest dissolved sediment yield in rivers into oceans in China. The Changjiang River basin lies in the subtropical humid zone with an annual temperature average of 16℃ and precipitation of 1 270mm, and the provenance bedrock dominantly consists of carbonate rocks in the upper reaches and igneous rocks in the middle-lower reaches. Its upper reaches is the second largest forest in China, and the abundant vegetation and active subsurface drainage make extensive dissolution of carbonate which accounts for high Ca^{2+} and HCO_3^{2-} in river water and high dissolved sediment yields in river basin. On the contrary, those rivers draining north plateaus in middle latitude, including the Huanghe, Haihe, Liaohe and Dalinghe rivers, lie in the warm-temperate semi-humid zone and warm semi-arid zone with an average precipitation of less than 800mm, and differences of temperature in a day and/or in a year increase further more than the rivers in low latitude. The loess is the main source rock in the river basins, and because of sparse vegetation and loose soil, physical weathering is very strong, which results in high detrital sediment yield and turbidity. Due to high salt content in loess, salt dissolution accounts for high ionic concentration in river water, but arid climate and sparse vegetation bring about weak chemical weathering and obviously lower dissolved sediment yields than in the Changjiang River, Pearl River and other south Asian rivers. The proportion of dissolved chemical flux in the total chemical flux is very small and D/ (D+S) is very low. Overall, the chemical flux of these rivers in middle latitude is closely related to strata lithology and climate.

Subarctic-arctic rivers in 50° N northward lie in the subfrigid and frigid zone with an annual temperature below 0℃ and precipitation less than 500mm. Taiga is widely distributed in the drainage basin, so physical weathering is rather weak. River water mainly comes from molten snow in spring, so sediment concentration and detrital sediment yield are very low and the latter lower by one to two orders than other Asian rivers. Furthermore, chemical weathering of tundra is very weak in cold climate, and dissolved sediment yields are the lowest in Asian rivers. Comparatively, ionic concentration increases in summer because of increasing rainfall and temperature. Therefore, compared with other Asian rivers, these subarctic-arctic rivers have similar detrital sediment yields and dissolved sediment yields, and the dissolved chemical fluxes account for a large proportion in the total flux, exceeding detrital sediment fluxes, and D/ (D+S) also higher than other Asian rivers. So it can be deduced that vegetation and climate are the main controlling factors of the chemical fluxes of subarctic-arctic rivers.

Besides climate, strata lithology and vegetation, the chemical fluxes of Asian rivers are also related to tectonic activity, especially those of the rivers originating from the Qinghai-Tibet Plateau, whose rise greatly influences chemical compositions of these rivers (Hong *et al.*, 1995; Shi *et al.*, 1999). High sediment concentrations and loads and sediment yields of the Changjiang, Huanghe, Ganges/ Buramaputra, Indus and Honghe rivers are tightly related to strong rise and erosion of the Qinghai-Tibet Plateau which causes monsoon formation in East Asia and the Loess Plateau development, and plays a

key role in controlling the chemical compositions of rivers originating from here.

5 Conclusions

Based on the above discussion, we can come to the following preliminary conclusions:

(1) Asian rivers into oceans have different chemical flux changes according to their geographical locations. These rivers can be divided into three zones on the basis of dissolved sediment loads and yields and ionic concentrations. Rivers located in 37°N southward have the highest dissolved sediment loads and yields, while rivers in 37°N~41°N bear lower dissolved sediment loads and yields, but the highest ionic concentrations and turbidity; Rivers in 41°N northward belong to the subarctic and arctic zone and most of them have the lowest dissolved sediment loads and yields and ionic concentrations, but the highest ratio of dissolved sediment loads to the total sediment loads.

(2) Ionic concentration and dissolved sediment yield increase gradually with the increasing annual temperature and precipitation, whereas the ratio of dissolved sediment loads to the total sediment loads decreases gradually. Dissolved sediment yields increase with runoffs, but ionic concentrations vary little with runoff.

(3) Rivers into oceans in China play an important role among Asian rivers. Several large rivers such as the Changjiang, Huanghe and Pearl rivers have different chemical fluxes which are mainly controlled by strata lithology and climate.

(4) Variations of chemical fluxes of Asian rivers are dominantly decided by climate, vegetation, strata lithology, weathering and tectonic activity. Different factors exert relatively different influence on chemical fluxes of different Asian rivers. Rise of the Qinghai-Tibet Plateau greatly influences the chemical compositions of the rivers originating from it.

References

[1] Milliman, J D, Meade, R H.(1983) World-wide delivery of river sediment to the oceans. *J.Geol.*, 91:1-21.

[2] Huang W W and Zhang J.(1994) Transport characters of chemical composition of the Changjiang River to East China Sea. *Acta Oceanologica Sinica*, **16** (2): 53-62 (in Chinese).

[3] Zhang L C, Dong W J and Wang L P. (1992) Geochemical characteristics of the Changjiang River water system. *Acta Geolographica Sinica*, **47** (3): 220-231 (in Chinese).

[4] Li, Y.H., Teraoka, H., Young, T.S. and Chen, J.S. (1984) The elemental composition of suspended particles from the Yellow and Yangtze Rivers. *Geochim. Cosmochim. Acta.*, 48, 1561-1564.

[5] Qu C H, Zheng J X, Yang S J, *et al.* (1984) Chemical compositions and their constraints of suspended sediments in controlling stations in the lower reaches of the Changjiang,Huanghe and Pearl rivers. *Science Bulletin*, 17: 1063-1066 (in Chinese).

[6] Zhao Y Y and Yan M C.(1992) Compare of chemical elements of Chinese shallow marine sediments.*Science Bulletin*, 37: 1202-1204 (in Chinese)

[7] Wang H W.(1995) Preliminary geochemical study of the Changjiang river water environment. *Geology and Geochemistry*, 6: 109-110 (in Chinese).

[8] ZhangL C and Dong W J.(1990) Chemical geographical characters of river water in East China. *Geographical Research*, 2: 67-75 (in Chinese).

[9] Yang S Y and Li C X. (1999) Elemental composition and geological background of the Changjiang

and Huanghe river sediments. *Marine Geology and Quaternary Geology*, **19** (2):19-25 (in Chinese).

[10] Zhang J(eds.).(1997) Biogeochanicla Study on Chinese main estuaries.Beijing: Ocean Press, 1-241 (in Chinese).

[11] Zhang J. and Huang W.W. (1990) Drainage basin weathering and major element transportation of two large Chinese rivers (Huanghe and Changjiang). *J. of Geophysical Research*, 95: 13277-13288.

[12] Xu J X.(1996) River process of different zones in China. Beijing: Science Press, 1-277 (in Chinese).

[13] Hay, W.W, (1998) Detrital sediment fluxes from continents to oceans. *Chem. Geol.*, 145: 287-323.

[14] Xu J X.(1994) Chemical erosion of different natural zones in China. *Scientia Geographica Sinica*, **14** (4): 306 -314 (in Chinese).

[15] Zhao Y Y and Yan M C.(1994) Geochemistry of shallow marine sediments in China. Beijing: Science Press, 1-203 (in Chinese).

[16] Zhang J. and Huang W.W. (1993) Dissolved trace metals in the Huanghe: the most turbided large river in the world. *Wat. Res.*. 27: 1-8.

[17] Hong Y T, Gu A L and Wang H W.(1995) Sulfur isotope composition of the Huanghe River and rise of the Tibet Plateau. *Quaternary Research*, 4: 360-366 (in Chinese).

[18] Shi Y F. Li J J and Li B Y.(1999) Rise of the Tibet Plateau during late Cenozoic and environmental change in East Asia. *Acta Geolographica Sinica*, **54** (1): 10-21 (in Chinese).

Sea to Air Flux of Dimethyl Sulfide and Its Effect on the Environment*

WU Ping (吴 萍), Yang Guipeng (杨桂朋)**
College of Chemistry and Chemical Engineering, Ocean University of Qingdao, Qingdao 266003

Abstract Reviews on the current studies on the sea to air flux of dimethyl sulfide (DMS) have been made at home and abroad, pointing out that the flux of DMS is influenced by many factors. There is great difference between the results coming from different models. Besides, this paper focuses on the oxidation mechanisms of DMS by OH and NO_3 radicals after it enters the atmosphere, the oxidation products' contribution to acid rain and fog and the relationships among the DMS, CCN and climate system.

Keywords dimethyl sulfide, sea-air flux, marine atmosphere, cloud condensation nuclei

Dimethyl sulfide produced from ocean phytoplankton is the primary natural source of sulfide in the atmosphere. DMS in the surface water is over saturated, and the concentration gradient of DMS between the ocean and atmosphere makes DMS send off to the atmosphere at an appreciable flux, which occupies about 50% of the total flux over the globe. It has already been showed that DMS would be oxidized within one or two days after it enters the atmosphere, and the products include methyl sulfonate (MSA), dimethyl sulfoxide (DMSO), *et al.*, and the products are continually oxidized to sulfate aerosol, which is one of the most important factors affecting the global climate. It not only directly influences the distribution of the raindrop and the radiation of cloud by increasing the amount of cloud condensation nuclei (CCN), but also indirectly influences the radiation reception and disbursement balance of the sunrays arriving at the earth by the so-called sun umbrella effect[1]. Moreover, DMS is closely related to the formation of acid rain and fog, thus greatly influencing the climate and environment. Studies about the source and distribution, flux and circulation of DMS have already been heated topics in the world [2,3]. This article mainly makes a summary of the atmospheric chemistry of DMS and its influence on the climate and environment.

1 Sea to air flux of DMS

If there were no mixture of gas over the land near the shore, the main source of DMS in the atmosphere would be the sea-to-air flux. The concentration of DMS in the marine atmosphere is about 100~300 $ng \cdot m^{-3}$, with a mean of 150 $ng \cdot m^{-3}$. In the course of measurement, if we pay attention to the specimens, we will find that the concentration of DMS in the marine atmosphere in each region is consistent with the dissolving concentration of DMS in the seawater[4]. We have known that the volatile organic sulfide comes into atmosphere through molecular diffusion and turbuient diffusion, but by now little is known about the diffusion process and we cannot estimate the value of the sea-to-air flux

* Natural Science Foundation of China (NO. 49706070)
* Natural Science Foundation of Shandong Province,(NO. Q97E04145)
** To whom all the correspondence should be addressed

with desirable mathematical and physical models. Recently we often use the Stagnant-Film model, that is, the model of gas flux: $F = -V_P (C_G / - C_L)$, in which, V_P is the transmission velocity of the gas in the surface water and also called the flux coefficient of gas, C_G: concentration of DMS, H: henry coefficient, C_L: concentration of DMS in the surface water. Because $C_G / H << C_L$, the formula can be written as $F = -V_P C_L$ [5]. Now we can see that actually the sea-to-air flux of DMS is controlled by the concentration in the surface water. The concentration of DMS in the surface water (C_L) is controlled by many factors and the transmission velocity (V_P) especially depends on the wind-speed, the fluctuation of water temperature and bubbling and so on. This makes the calculation of DMS very complex, although there have been many researchers who have done the calculation of the flux of DMS regionally and globally [6,7]. Because of the difference in the models and concentration of DMS in each area, there is much difference in the flux Of DMS. Tables 1 and 2 respectively list the flux of DMS in the ocean areas and different oceans in the world calculated by different authors.

Tab. 1 Sea to air flux of DMS in different oceans calculated by different authors

	Sea-to-air flux (μ mol/m² • d)	Mean flux (μ mol/m² • d)	Source (author)
Equator (summer)	3.79—6.61	5.10	Zheng Min et al.[5]
Equator (winter)	3.7—9.1	4.97	Bates [7]
North Pacific (summer)	2.89—14	6.25	EricksonIII [8]
North Pacific (winter)	0—10.8	3.97	EricksonIII [8]
East China Sea	—	3.4	Yang [9-12]
South China Sea	—	5.5	Yang [9-12]

Tab. 2 The concentration and flux of DMS in different oceans

Ocean areas	Area (10^6Km²)	Mean concentration (nmol/L)	Total flux (10^{12}g/a)
Equatoral and littoral upwelling area	86.5	4.9	6.4-22.4
Littoral shelf area	49.4	2.8	3.2-6.4
Tropical low production area	148.3	2.4	6.4-19.2
Temperate zone area	82.8	2.1	3.2-9.6

The data in the above two tables demonstrate that the flux of DMS has a great change with the change of time and area. Although the calculation of flux is not exact, we can affirm that DMS is the predominant biological source sulfide in the seawater, and its cycle over the globe is very important.

2 Reactions between DMS and radicals in the atmosphere

The major fate of DMS in the marine atmosphere is reaction with OH radicals during daytime and NO_3 radicals during nighttime. Recent studies have shown that the Cl-atom and IO radicals also can oxidize DMS in the atmosphere[13,14], but it is showed that the velocity of the reactions is slower, so it can be neglected[15].

The reaction between DMS and OH radicals proceeds by both O_2-dependent and O_2-independent

pathways, with the O_2-independent pathway accounting for 75% of the overall reactivity at 300K. The O_2-dependent pathway involves the formation of adducts and the subsequent competition between adduct reaction with O_2 and adduct decomposition to reform DMS and OH[16,17]. The O_2-independent pathway is dominated by H-atom abstraction, producing the CH_3SCH_2 radicals [18,19]: $DMS + OH \rightarrow CH_3SCH_2 + H_2O$. By analogy with other alkyl radical oxidation processes, the following mechanism has been proposed for the atmospheric oxidation of the CH_3SCH_2 radical[20]:

$$CH_3SCH_2 + O_2 + M \rightarrow CH_3SCH_2O_2 + M \quad (1)$$

$$CH_3SCH_2 + M \rightarrow CH_3SCH_2O + NO_2 \quad (2)$$

$$CH_3SCH_2O + M \rightarrow HCHO + CH_3S + M \quad (3)$$

It is thought that, in addition to thermal decomposition of CH_3SCH_2O in the DMS oxidation mechanism outlined above, there might be a reaction channel with O_2 to form MTF (CH_3SCHO), which can be further oxidized to produce COS[21].

$$CH_3SCH_2O + O_2 \rightarrow CH_3SCHO + HO_2 \quad (4)$$

$$CH_3SCHO + OH \rightarrow H_2O + CH_3 + COS \quad (5)$$

The O_2-dependent pathway is dominated by OH radicals addition to S-atom: $CH_3SCH_2 + OH \rightarrow CH_3S(OH)CH_3$, this reaction becomes progressively more important with the decrease of temperature. More recently, laser flash photolysis (LFP)— pulsed laser-induced fluorescence (PLIF) techniques are used to study the chemistry of DMS + OH + O_2 + NO system, and it has been proved that CH_3S is the dominant sulfur-containing product generated by the sequence of (1)–(3)[19]. The CH_3S radical is a central species in the current proposed DMS oxidation mechanisms because it is theorized to be the principal source of the frequently cited DMS oxidation products SO_2, SO_3, MSA and sulfuric acid[22]. Hynes *et al.*[16] utilize the same technique to study the kinetics of reaction between DMS and OH with its deuterated analogue reaction: $OH + CD_3SCD_3 \rightarrow$ products. Their results are consistent with the former, proving that the two channels are right. The fate of the weakly bound DMS-OH adduct formed in the O_2-dependent addition channel will be thermal decomposition in competition with reaction with oxygen[16,23]. Potential reaction pathways for the DMS-OH adduct are:

$$CH_3S(OH)CH_2 + O_2 \rightarrow CH_3SOCH_3 + HO_2$$

$$\rightarrow DMSO_2 + OH$$

$$\rightarrow (CH3)_2S(O_2)OH$$

$$\rightarrow CH_3SOH + CH_3$$

It is found that SO_2 is the most important adduct in the reaction between DMS and OH radicals, and it accounts for 70% of the overall adducts.

During nighttime, especially in the polluted marine atmosphere, there is much NO_x, and the dominated reaction of DMS is between DMS and NO_3 radicals. Although the mechanistic and kinetic study of the reaction between DMS and OH radicals has been carried out earlier, by the middle of the 1980s little had been known about the mechanism and products of NO_3 reaction with DMS. At that time the products were studied with FT-IR and gas chromatography techniques, HNO_3, NO_2, HCHO and small amounts of SO_2 were found, DMSO and MSA were not detected and no reaction mechanism was proposed. At the same time the reaction mechanism for NO_3 with a series of other sulfur compounds has also been studied[24]. Until the 1990s, in the laboratory study, long path FT-IR spectroscopy and ion chromatography were used for measuring intermediates and end products of the DMS + NO_3 reaction in air, HNO_3, HCHO, SO_2, MSA were found to be the main products of reaction, with MSA as the most abundant sulphur compound, organic peroxynitrates and CH_3SNO_2 have been identified as intermediates

from their characteristic spectral feature. Based on the results the mechanism for the reaction DMS+NO_3 is proposed, which has hydrogen abstraction as the first step:

$CH_3SCH_3 + NO_3 \rightarrow CH_3SCH_2 + HNO_3$

There is no evidence for the alternative addition reaction: $CH_3SCH_3 + NO_3 \rightarrow CH_3S(NO_3)CH_3 \rightarrow CH_3SOCH_3 + NO_2$. Cl-atoms are from the decomposition of Cl_2CO: $Cl_2CO \rightarrow 2Cl + CO$[22], the first step of the reaction DMS + Cl is also the hydrogen abstraction: $Cl + DMS \rightarrow CH_3SCH_2 + HCl$. In the above reactions CH_3SCH_2 radical can be oxidized continually: $CH_3SCH_2 + O_2 \rightarrow CH_3SCH_2O_2$, and $CH_3SCH_2O_2 + NO_x \rightarrow$a series of products[24].

Usually OH and NO_x radicals coexist in the marine atmosphere, so their reactions with DMS are interrelated. Studies have demonstrated that the principal products of DMS + NO_3 appear to be the same as those of the DMS + OH + NO_x system, except for HNO_3, which comes from the hydrogen abstraction by NO_3. Besides, NO_x concentrations also influence the products distribution of OH-initiated oxidation of DMS, the formation yields of MSA and $DMSO_2$ increase with the NO_x concentration, whereas the yields of DMSO and SO_2 decrease, and the presence of low levels of NO reduces the yields of both MTF and COS to zero[23]. Based on the above analysis, and according to the literature research findings, the reaction pathways, products, and velocity coefficients are listed in Figure 1[4,25,26].

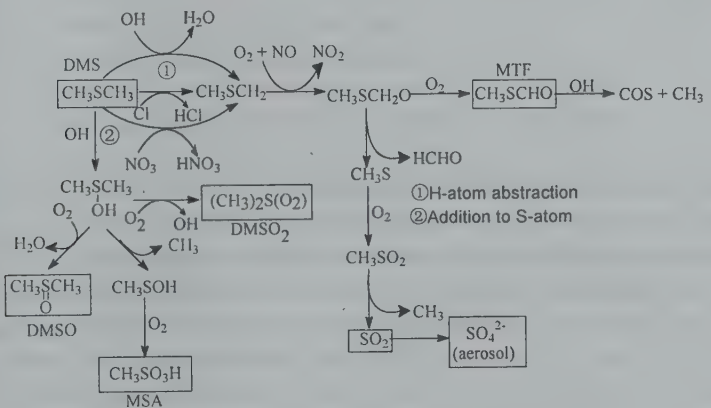

Fig 1 The reaction pathway of DMS in the atmosphere

$CH_3SCH_3 + OH \rightarrow aSO_2 + (1-a)CH_3SO_3H$ + other products

Reaction rate constant $k_{OH} = 0.75-1.5\times10-11$ cm^3 mol^{-1} $s-1$[5,27,28]

$CH_3SCH_3 + NO_3 \rightarrow aSO_2 + (1-a)CH_3SO_3H + NO_2$ + other products

Reaction rate constant $k_{NO3} = 5.4-9.9\times10^{-13}$ cm^3 mol^{-1} s^{-1}[4,5,28]

3 The influence of DMS on the environment

Field measurements and theory studies have demonstrated that the flux of DMS, the oxidation of DMS to MSA and SO_2, continual oxidation to non-sea-salt sulfate, the dry deposition and wet deposition constitute the cycle of sulfur in the unpolluted marine atmosphere. A model overview is presented in

Figure 2[129].

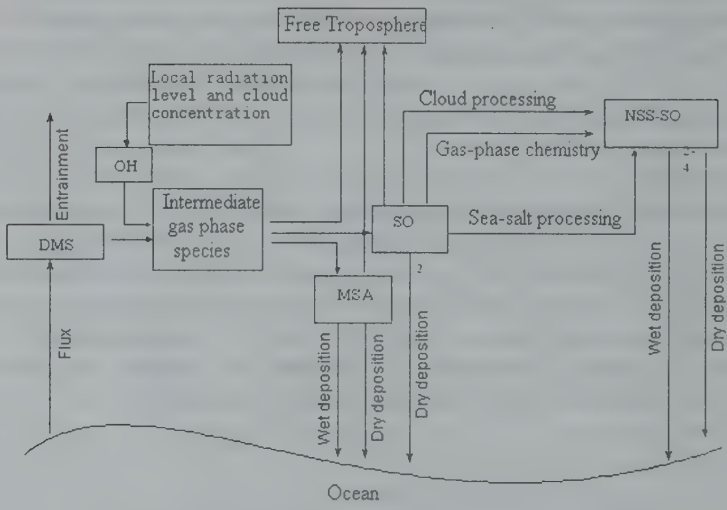

Fig 2 The cycle of sulfur in the unpolluted marine atmosphere

In Figure 2, 35% of SO_2 are consumed by deposition, 60% are transferred to non-sea-salt sulfate by heterogeneous phase reaction[15], greatly surpassing the dry deposition velocity [130]. Dry deposition is parameterized using a deposition velocity, a value of 0.5 cm/s is used for SO_2,and 0.01cm/s for NSS-SO_4^{2-} and MSA. In this model SO_2 is oxidized to sulfate rapidly in cloud droplets through reaction with hydrogen peroxide, and it is assumed that all available SO_2 can be converted to NSS-SO_4^{2-} because there is excess H_2O_2 in the marine boundary layer[129]. Reaction in sea-salt particles also converts SO_2 to sulfate, but in this case the dominant oxidation is ozone. The ozone reaction rate is sensitive to pH, and the buffering capacity of sea-salt keeps the pH high enough to the ozone reaction, the velocity of gas-phase reaction is much lower compared with that of the heterogeneous phase reaction. The cycle of DMS between ocean and atmosphere influences the climate and environment seriously in the following ways:

Firstly, the amount of DMS emitted from the ocean is so large that it can influence the balance of sulfur all over the globe. There are many evidences demonstrating that the sulfur emitted from the ocean plankton can transport to the land atmosphere[130]. Most of the oxidation products of DMS in the atmosphere are strongly acidic and influence the acidity of natural deposition materials. Nguyen[131] thought that the oxides of DMS such as SO_2 and so on, are the main source of acid rain, and can contribute about 40% of the acidity of acid rain. But recently, with the growth of population and the development of industry, the amount of SO_2 coming from human activities is two times bigger than that from DMS, and its effect has extended beyond the northern hemisphere[132], which is bound to aggravate the acid level of environment. The acidification of environment resulted from acid rain (pH < 5.6) or acid deposition is one of the most important problems in this century.

Secondly, the sulfate aerosol coming from DMS oxidation in the air is the major source of CCN in the marine atmosphere. Calhoun[33] *et al.* proved this conclusion by determining the aerosol particles using the sulfur isotope. In the unpolluted marine atmosphere the concentration of CCN particles is about 30~200cm^{-3}. It is observed that sea-salt particle concentrations at the cloud height are typically not more than 1 cm^{-3}, so that the sea-salt itself cannot be the main CCN. Water-soluble materials other than sea-salt and NSS-SO_4^{2-} do exist in the marine air but the data are not extensive. Nitrates probably are found on coarser particles, and hence do not contribute substantially to the number population. Organic compounds exist in the sub-micrometer particles, but their mass concentration is probably only one tenth of NSS-SO_4^{2-}, their number concentration and source is still unknown. So by now the major CCN is NSS-SO_4^{2-} and the mass concentration of NSS-SO_4^{2-} in the remote marine troposphere is about 0.3 μ g · m^{-3}, if the number mean radius is 0.07 μ m.

The forming of clouds and the reflectance for solar radiation are sensitive to CCN density, which also affects the climate and the temperature of the globe. Charlson[30] et al. estimated that the increase of CCN could offset 2% of the increasing sunlight or the doubling greenhouse effect of CO_2. Andreae[6] suggested that if the flux of DMS doubled, the mean temperature of globe would change several degrees. But some authors[32] thought that even if the climate effects would result from the sulfate aerosols contrary to the greenhouse effect, this effect was partial. They also thought that because the radiative forcing resulted from the concentration increase of greenhouse gases was about 2.3 W · m^{-2} [34], the climate effect of sulfate aerosols couldn't compensate for the greenhouse effect.

Putaud *et al.* [25] proved that there was obvious correlation between the daily mean sea-air flux and the daily mean concentration of DMS, the DMS concentration in the unpolluted marine atmosphere and NSS-SO_4^{2-}, the NSS-SO_4^{2-} concentration and CCN concentration, the DMS concentration and CCN. Bates *et al.* [35] considered that there is direct correlation between DMS and CCN, CCN and the albedo of clouds [30], so there must be inevitable correlation between a series of links: DMS flux — DMS concentration —NSS-SO_4^{2-} concentration—CCN concentration—cloud albedo—global temperature. For example, the measurement results of north Pacific showed that when the particle concentration coming from DMS doubled, the amount of CCN would increase 30-40%[36]. Figure 3 is the climatic anti-feedback of DMS advanced by Charlson *et al.*[30]

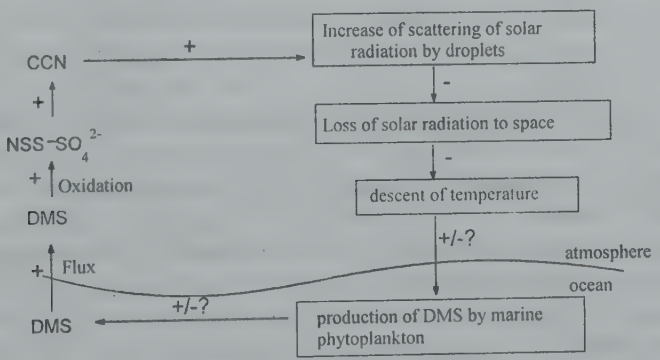

Fig 3 Anti-feedback of DMS to the climate

4 Summary

In this paper, we have learned much about the flux of DMS and its influence on the environment. DMS escapes to the air throngh sea-to-air flux, which is affected by many factors. By now there is no desirable method to calculate it. In the later studies we should make the model calculation much nearer to the actual conditions, so that we can get more satisfactory results. Moreover after DMS enters the atmosphere, it is oxidized by a series of processes to generate sulfate aerosol, thus influencing the climate and environment seriously. Recently a great breakthrough has been effected in the studies about the mechanism of DMS oxidized by OH and NO_3 radicals, which has been made much clearer. But still little has been known about the quantity relations between the emitted amount of DMS and sulfate aerosol and CCN. With the studies becoming deeper, we can conquer difficulties and make greater contributions to knowing the reasons of climate change and environment acidification.

References

[1] Jiao Ningzhi, Liu Chengzhang, Chen Nianhong (1999) Distribution of dimethylsulphoniopropionate and its controlling factors [J]. *oceanologia et limnologia, sinica.* (ch), **30** (5): 525-531.

[2] Hu Min, Tang Xiaoyan (1997) Dimethyl sulfide in seawater in the Jiaozhou Bay [J].*Huanjing kexue xuebao* (ch), **17** (1) : 110-115.

[3] Cui Zeng, Zhang Manping. (1999) Study on the determination and origin of dimethyl sulfide in seawater [J]. *Oceanography of Yellow and Bohai Seas* (ch), **17** (1) : 70-75.

[4] Andreae M O, Ferek R J, Bermond F P, *et al.* (1985) Dimethyl sulfide in the marine atmosphere [J]. *J. Geophys Res*, **90** (D7): 12891-12900.

[5] Zheng Min, Li Xingsheng (1994) Numerical simulation of dimethyl sulfide in the marine atmosphere [J]. *Science in China* (ch), **24** (6) : 664-672.

[6] Andreae M O (1990) Ocean-atmosphere interactions in the global biogeochemical sulfur cycle [J]. *Mar. Chem.*, 30: 1-29.

[7] Bates T S, Cline J D, Gammon R H, *et al.* (1987) Regional and seasonal variations in the flux of oceanic dimethyl sulfide to the atmosphere [J]. *J. Geophys Res.*, 92: 2930-2938.

[8] Erickson III D J, Ghan S J, Penner J E. (1990) Global ocean to atmosphere dimethyl sulfide flux [J]. *J. Geophys Res*, 95: 7543-7552.

[9] Yang Guipeng (2000) Spatial distribution of dimethyl sulfide in the South China Sea [J]. *Deep-Sea Res.* I. 47: 177-192.

[10] Yang Gui peng, Zhang Jianwu (2000) Dimethyl sulfide in the surface water of the East China Sea [J]. Cont. Shelf Res. 20: 69-82.

[11] Yang Guipeng, Liu Xintong, Li Li, *et al.* (1999) Biogeochemistry of dimethyl sulfide in the South China Sea [J]. *J. Mar Res*, **57** (1): 189-211.

[12] Yang Guipeng (1999). Dimethyl sulfide enrichment in the surface micro-layer of the South China Sea [J]. *Mar Chem.* 66: 215-224.

[13] Pszenny A A P, Keene W C, Jacob D J, *et al.* (1993) Evidence for inorganic chorine gases other than hydrogen chloride in marine surface air [J].*Geophys Res Letts*, **20** (8): 699-702.

[14] Barnes I, Becker K H, Carlier P, *et al.* (1987) Ftir Study of the DMS/NO_2/I_2/N_2 Photolysis system:

The reaction of IO radicals with DMS [J]. *Int J Chem Kinet*, 19: 489-501.

[15] Daykin E P, Wine P H. (1990) Rate of reaction of IO radicals with dimethyl sulfide [J]. *J. Geophys Res*, 95:18547-18553.

[16] Hynes A J, Stoker R B, Pounds A J, *et al.* (1995) A mechanistic study of the reaction of OH with dimethyl-d_6 sulfide, direct observation of adduct formation and the kinetics of the adduct reaction with O_2 [J]. *J. Phys Chem*, 99: 16967-16975.

[17] Barone S B, Turnipseed A A, Ravishankara A R. (1996) Reaction of OH with dimethyl sulfide (DMS). 1. Equilibrium constant for OH + DMS reaction and the kinetics of the OH • DMS + O_2 reaction [J]. *J. Phys Chem*, 100: 14694-14702.

[18] Stickel R E, Zhao Z, Wine P H. (1993) Branching ratios for hydrogen transfer in the reactions of OD radicals with CH_3SCH_3 and $CH_3SC_2H_5$ [J]. *Chem Phys Lett*, 212: 312-318.

[19] Turnipseed A A, Barone S B, Ravishankarara A R. (1996) Reaction of OH with dimethyl sulfide. 2. Products and mechanisms [J]. *J. Phys Chem*, 100: 14703-14713.

[20] Niki H, Maker P D, Savage C M, *et al.* (1983) An FT-IR study of the mechanism of the reaction OH+ CH_3SCH_3. *Int J Chem Kinet*, 15: 647-654.

[21] Barnes I, Becker K H, Patroescu I. (1994) The tropospheric oxidation of dimethyl sulfide: A new source of carbonyl sulfide [J]. *Geophys Res Lett*, **21** (22): 2389-2392.

[22] Shawn P V, Robert E S, Zhao Z Z, *et al.* (1997) Mechanistic and kinetic study of formaldehyde production in the atmospheric oxidation of dimethyl sulfide J]. *J. Chem Soc Faraday Trans*, **93** (6): 2813-2819.

[23] Patroescu I V, Barnes I, Becker K H, *et al.* (1999) FT-IR product study of OH-initiated oxidation of DMS in the presence of NOx [J]. *Atmos Enviro*, **33** (1): 25-35.

[24] Jensen N R, Hjorth J, Lohse C, *et al.* (1991) Products and mechanism of the reaction between NO_3 and dimethyl sulphide in air [J].*Atoms Enviro*, **25A** (9): 1897-1904.

[25] Putaud J P, Belviso S, Nguyen B C, *et al.* (1993) Dimethyl sulfide, aerosols, and condensation nuclei over the tropical northeastern Atlantic ocean [J]. *J. Geophys Res*, 98: 14863-14871.

[26] Malin G, Turner S M, LISS P S. (1992) Sulfur: The plankton/climate connection [J]. *J. Phycol*, 28: 590-597.

[27] Nguyen B C, Bonsang B, Gaudry A. (1983) The role of the ocean in the global atmospheric sulfur cycle [J]. *J. Geophys Res*, 88: 10903-10914.

[28] Atkinson R, Pitts J N J, Aschmann S M. (1984) Tropospheric reactions of dimethyl sulfide with NO_3 and OH radicals [J]. *J. Phys Chem*, 88: 1584-1587.

[29] Kevin P C, Spyros N P.(1997) Dimethyl sulfide chemistry in the remote marine atmosphere: Evaluation and sensitivity analysis of available mechanisms [J]. *J. Geophys Res*, **102** (D19): 23251-23267.

[30] Charlson R J, Lovelock J E, ANDREAE M O *et al.* (1987) Oceanic phytoplankton, atmospheric sulphur, cloud albedo and climate [J]. *Nature*, 326: 655-661.

[31] Nguyen B C, Mihalopoulos N, Putaud J P, *et al.* (1992) Covariations in oceanic dimethyl sulfide, its oxidation products and rain acidity at Amsterdam Island in the southern Indian Ocean [J]. *J. Atmos Chem*, 15: 39-53.

[32] Hu Rongming, Shi Guangyu (1998) The radiative forcing and climate effect due to anthropogenic sulfate aerosols over China [J], *Atmospheric Science* (ch), **22** (6): 919-925.

[33] Calhoun J A, Bates T S, Charlson R J. (1991) Sulfur isotope measurements of sub-micrometer aerosol particles over the Pacific Ocean [J]. *Geophys Res Lett*, 18: 1877-1880.

[34] Shi G Y, Fan X B. (1992) Past, present and future climate forcing due to greenhouse gases [J]. *Adv. Atmos. Sci*, 9: 279-286.

[35] Bates T S, Charlson R J, Gammon R H. (1987) Evidence for the climatic role of marine biogenic sulpher [J]. *Nature*, 329: 319-321.

[36] Quinn P K, Covert D S, Bates T S, *et al*. (1993) Dimethyl sulfide/cloud condensation nuclei/climate system relevant size-resolved measurements of the chemical and physical properties of atmospheric aerosol particles [J]. *J. Geophys Res*. **98** (D6): 10411-10427.

Application of Hydrocarbons Biomarkers in Marine Organic Geochemistry

Wu Ying (吴 莹)[1], Zhang Jing (张 经)[1,2]

1 *State Key Laboratory of Estuarine and Coastal Research, East China Normal University, Shanghai* 200062

2 *College of Chemistry and Chemical Engineering, Ocean University of Qingdao, Qingdao* 266003

Abstract Biomarker is an important tool in the study of marine organic geochemistry. Its development and application makes it possible to elucidate the process and mechanism of the organic matter in the ocean. Hydrocarbons are the most useful molecular markers. They are used as tracers in many aspects, such as source indication; the degradation of organic matter; diagensis process; environmental pollution and paleooceanic study, etc. They are studied in the estuaries, coastal area and deep sea to give the knowledge of marine organic geochemistry. The paper deals with the characteristics, development and application of biomarkers as well as their advantages and disadvantages.

Keywords biomarker, hydrocarbon, marine organic geochemistry

1 Introduction

Early on in the sedimentary process, some organic compounds exist as largely unaltered constituents of the source organisms, such as porphyrin[1]. Depending on the specificity of these compounds, it should be possible to gain an idea of the types of organism contribution to the sedimentary matter and even to estimate their relative contributions. Such compounds are defined as biomarkers [2]. Biomarkers are important source indicators in the study of marine organic geochemistry. For example, 4-methylsterols is a good indicator of the contribution of phytoplankton[3], and lignin and triterpanes are good tracers of terrestrial inputs in the environment[4]. An illustration of biomarkers in the chemosphere is showed in Figure 1.

For source analysis, biomarkers afford several advantages over measurements of bulk chemical properties such as elemental and stable isotope composition. First, the diversity and great number of different organic molecules in natural samples allow finer resolution sources contribution. Secondly, biomarkers often occur in suites within which the relative abundance of the congeners sometimes carries additional environmental or diagenetic information. For example, changes in unsaturation within the suite of long-chain ketones correspond to the water temperature that could help to indicate ancient temperature in the history[5]. Finally, source distinctions based on molecular-level analyses often afford orders of magnitude greater sensitivity than bulk chemical measurement.

The biomarker approach has been used to judge the nature of: (1) original source materials and remineralization and degradation processes[6]; (2) paleoenvironmental conditions of sedimentation[7]; (3) environmental pollution and petroleum seepage.[8]

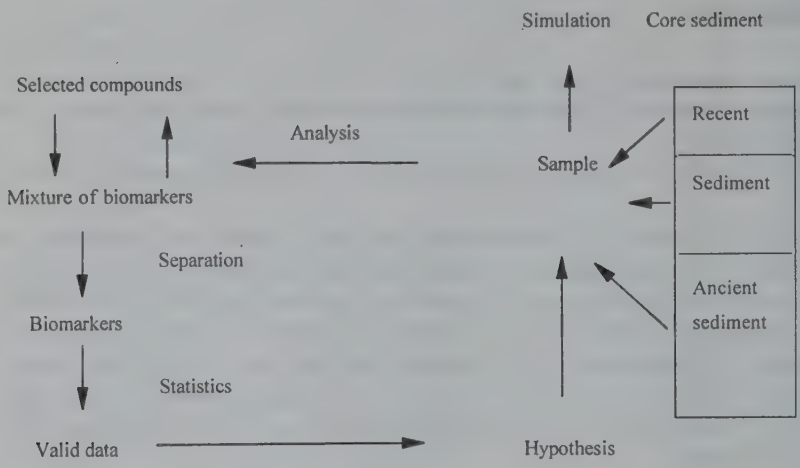

Fig. 1 Establishment and analysis of biomarkers in the study of organic geochemistry[7]

Many kinds of compounds could be used as biomarkers, such as porphyrin, humus, lignin, n-alkanes, PAHs, sterols etc. In the series of compounds, the different ratios are studied to get a clearer indication of sources or processes.

However, there is still some hypothesis for the biomarkers used as source indicators. That is just the limit of biomarkers and any study on the biomarkers should take it seriously (Table 1).

Tab. 1 Biomarker: hypothesis of five basic applications [9]

Application	Hypothesis
1. source indication	A. B can be quantitatively detected.
	B. The source of B is definite and known.
2. relative concentration of biomarker	A. Both of the above are OK.
	B. B could be quantitatively detected.
	C. B' s concentration is resistant to the degradation process..
3. the relationship between biomarker and AOM	A. Both of the above are OK.
	B. In the sources, B/AOM is unchanged.
	C. B/AOM will not change with degradation.
4. AOM's concentration	A. All the above is OK.
	B. B/AOM is known in the samples.
5. estimate of paleoproduct of AOM	A. All the above is OK.
	B. B/AOM of the sources is steady for long time.
	C. B and AOMs sources are definite.
	D. B/AOM have no relationship with degradation.

Biomarker methods, however, pose significant disadvantages as well. One of these is that

information on the distributions of organic molecules in living organisms is incomplete and spotty. In addition, biomarkers, like bulk organic materials, are sensitive to diagenetic effects. To overcome these difficulties, some ratios and relative contributions are often used. Factor analysis of a wide range of sedimentary components may be employed[10]. Isotopic composition of individual compounds have the potential for establishing sources for the material, bacterial or otherwise.[11, 12]

2 Application of hydrocarbons

Hydrocarbons are one of the important compounds which involve extracting the sediment with a suitable combination of organic solvents. They include n-alkanes, polycyclic aromatic hydrocarbons (PAHs), fatty acids, sterols etc. All of them are widely used in the study of organic geochemistry.

2.1 n-Alkanes

The n-alkanes are ubiquitous compounds and have a strong preference. N-alkanes in marine phytoplankton show a unimodal distribution with a maximum at C_{15} and C_{17}.[13] The major n-alkanes found in terrestrial plant waxes are C_{29} and C_{31}. Such distribution shows a strong odd to even predominance with Carbon Preference Index (CPI) varying from 4~11.[14] N-alkanes is a good indicator of different sources[15](Table 3). It may also be used to assign the depositional paleoenvironments of ancient sediments and petroleum seepage[16].

Tab. 2 Sources of *n*-alkanes on the earth[17]

	Composition	Carbon range	Predominant peak
Bacteria	Hydrocarbons	C_{16}-C_{20}	
	Fatty acids	C_{10}-C_{20}	
Phytoplankton	Hydrocarbons	$< C_{20}$	nC_{15}, nC_{17}
	Fatty acids	$< C_{20}$	nC_{16}, nC_{18}
Aquatic algae	Lipids		nC_{21}, nC_{23}, nC_{25}
Bark	Cutin, xylem	C_{16},C_{18},C_{12}-C_{26}	nC_{12}-nC_{26}
leaves	Fat, wax	C_{24}-C_{26}	nC_{27}, nC_{29}, nC_{31}
Seed			
Pollen	Resin	C_{15}-C_{40}	Short-chain n-alkanes
Fruits	Spore		
	Tannin		
	Pigment		

2.2 PAHs

PAHs are a series of compounds, which contain several fused benzenoid rings. Distributions of PAHs are characterized by the dominance of the parent, non-alkylated species including phenanthrene, pyrene, chrysene, fluoranthene, benzopyrene, perylene, benzofluoranthene, coronene etc. They are formed by the action of the heat generated during the combustion process, but under conditions of local oxygen deficiency, they can be considered as pyrolysis products. The presence of pyrolytic PAHs in

recent sediments is generally considered to reflect inputs from the combustion of organic matter, such as wood and fossil fuels. Pyrolytic PAHs are widespread in the sediments postdating the industrial revolution and demonstrate the extent of human influence on the environment.[18]

Several researches have found that some PAHs, such as benzopyrene and pyrene etc., are strongly carcinogenic. The distribution and cycling of such compounds have received much attention.[19,20] PAHs could be concentrated and exaggerated through the food chain and have the potential of threatening human health. More studies are carried out with focus on the behavior and harms of PAHs in the environment. Because of its stability and resistance to degradation, PAHs are considered as an ideal indictor of environmental pollution. Usually the concentrations of PAHs are quite low and vary at 10^{-9}–10^{-12}, but their compositions still could indicate the contributions of different sources. Hites etc.[21] found that the sediments which are near or far from cities could be considered as anthropogenic and natural inputs. The different distributions of PAHs on the Northern and Southern Hemispheres are related to the development of industry and growth of population. It is quite impossible that PAHs are traced to the wood fires which are far from the study area. Usually the open sea receives a relatively high amount of PAHs via long distance atmospheric transportation. They are the products of combustion from oil and coal and transported by wind and rain as dry/wet depositions to put into the marine environment; sometimes, riverine inputs could be responsible for the anthropogenic sources' contribution.[22]

2.3 Fatty acids and sterols

In the sediment environment, there are plenty of organic matters, such as phytoplankton, algae, fungi, bacteria, zooplankton, benthic organisms, plant etc. All of the organic matter is produced in situ or transported by currents from elsewhere and deposited and kept in the sediments. Remineralization and degradation are unavoidable during the whole processes. Most organisms change a lot from the original forms except fatty acids and sterols. More attention is focused on those two kinds of compounds.

Fatty acids are widely occurring compounds and fulfil a variety of roles, such as cellular membrane components, energy storage and protective coating. The amount of fatty acids in phytoplankton could reach 5~25%. Most abundant compounds are C_{14}, C_{16} and C_{18}. Usually the higher fatty acids show even to odd predominance in plants and micro-organisms. Such preference is well kept even in the sediments. However, fatty acids in bacteria are often observed in the C_{80}–C_{110} range with the predominance of C_9. Short saturated fatty acids (C_{120} C_{200}) are easily found from phytoplankton and micro-organisms .[23] Higher plants are different from algae in exhibiting a characteristic distribution of long chain fatty acids (C_{220}–C_{340})[24]. Thus fatty acids are useful broad indicators of source types.

Sterols are found in both free and bound form in organisms. The carbon number distribution of regular sterols in sediments appears to permit a degree of distinction between the contributions of some groups of organisms.[25] The plankton in general contains dominant C_{27} and C_{28} sterol. β-sitosterol is mainly from vascular plant and dinoseterol (24β) comes from marine algae. Coprosterol is only produced in the alimentary canals of animals. It is considered as a good sewager tracer in the coastal area.[26] In Table 3, we list the lipid biomarkers' general indications in the studies.

Tab. 3 General indications of lipid biomarkers in the study of organic geochemistry

Source	Description	Indication	Ref.
Terrestrial input	n-alkanes: C_{31}/C_{17}; $C_{22}+/C_{22}-$; CPI	The ratios > 1, indicate terrestrial inputs.	27
	Fatty acids: CPI_A; H/L	The ratios > 1, indicate terrestrial inputs.	28
	PAHs: alkyl-chrysene; retene; perylene	Originated from vascular plant	29
	sterol: C_{29}-sterol	Easily found in higher plant	25
Marine source	phytoplankton: short chain alkanes; C_{27}-C_{28} sterols; unsaturated fatty acids	They are quite specific for definite source.	30, 31,32
	Sea grasses: $C_{16:0}$; $C_{18:1}$; $C_{18:2}$ fatty acids		
	bacteria: ante, fatty acids		
Paleoenvironment	n-alkanes	Indication of paleoproduction	33
Environmental pollution	Alkanes: UCM	Oil pollution	34
	PAHs: phe/anth; fluo/pyr; methy-phe/phe etc	Pyrolytic or petroleum pollution	35
	sterols: coprosterol	Sewage pollution	26

2.4 Degradation of hydrocarbons

The hydrocarbon is subject to a variety of processes, which can alter its character in the relatively short time between its synthesis and its long-term burial in the water bottom. Foremost among these processes is the biochemical oxidation of organic matter within the water column and sediment-water interface. Several parameters may be in control of this process, such as season, water temperature, burial depth, settling rate and burial rate of organic carbon, etc. However, the most important factors are sources of organic matter, distribution of bacteria and environment-specific characteristics (oxygen concentration, redox zonation).[36] Usually a clear reactivity trend is indicated: fatty acids >sterol > n-alkanes during early diagenesis.[37] The detailed evaluation of hydrocarbon biomarkers in sediments provides specific information on the stability and reliability of the compound, as well as on the diagenetic process and recycling on the sediment-water interface.[38]

Of the organic matter deposited on the sediment surface, 30~99% is remineralized during early diagenesis. Extremely labile marine lipids that are enriched in settling particles, such as pristane, 24-methylcholesta-5, 22 E-dien-3 β-ol etc., are quickly lost near the sediment-water interface. Only the moderately reactive components ($C_{22:0}$, $C_{24:0}$ fatty acids and long-chain n-alkanes) persist deep enough to preserve the geographical trends observed for rapidly settling particles.[39] The sediment-water interface is a dynamic zone where high rates of microbial mediated processes alter organic matter and regenerate essential inorganic nutrients. In the anoxic sediment, the contribution of bacteria will be stronger and long-chain compounds will become steady .[40] Fatty acids are easily affected by bio-degradation in core sediments. It is found that the concentration of fatty acids and the ratio of FA/TOC decrease dramatically in the top 25 cm. However, the long-chain fatty acids (such as $C_{24:0}$, $C_{26:0}$ and $C_{28:0}$) vary little while the short-chain fatty acids ($C_{15:0}$, $C_{16:0}$ and $C_{18:0}$) vary remarkably. The degradation rate could reach 6~7.[41] So me types of fatty acids are more susceptible to early diagenesis than are others, so that comparisons between different components can distinguish diagenentic effects from source changes. Short-chain

n-alkanes (C_{17} and C_{19}) which are indicative of phytoplankton inputs are usually found in low concentrations in the core sediments. N-alkanes / undissolved organic matter increases with depth.[42]

Elucidating the history of Earth from the view of marine organic geochemistry has always been a challenging and demanding task. It relies on the variety of biomarkers. The hydrocarbons have been given reliable clues about the source and sinks for sedimentary organic carbon. Important new data about the organic geochemical cycles and global change will come from fine-scale atomic, molecular and isotopic analysis of sediments in the near future.

Reference

[1] Trebis A. (1934) Chlorophyll and humin deviate in bitumin, gesteriren, erdoter, erdwachsen and asphalten. *Ana. Chem.*, 510: 42-62.

[2] Killops S.D. and Killops V.J. (1992) An introduction to Organic Geochemistry, Longman Scientific & Technical, London, pp 253.

[3] Stacher I.L. and Jefferey S.W. (1988) Photosynthetic pigments in fifty one species of marine diatoms. *J.Phycol.*, 24: 158-172.

[4] Simoneit B.R.T. (1986) Cyclic terpenoids of the geosphere in biological markers in the sedimentary records (R.B. Johns ed.) Elsevier New York, 43-99.

[5] Mccaffery M.A., Farrington J.W. and Repeta D.J. (1990) The organic composition of Peru marine sediments: historical EL NINO records. *Geochim. Cosmochim. Acta*, 54: 1671-1682.

[6] Getliff J., Teece M., Parkes R.J. *et al.* (1993) Microbial processes and the genesis of fossil biomarkers: An experimental study of the alga Emiliania huxleyi. Terra Nova, 5 706.

[7] Eglinton G., Bradshaw S.A., Rosell A. *et al.* (1987) Molecular record of secular sea surface temperature changes on 100-year timescales for glacial terminations. *Nature*, 356: 423-426.

[8] Lipiatou E. and Saliot A. (1991) Fluxes and transport of anthropogenic and natural polycyclic aromatic hydrocarbons in the western Mediterranean Sea. Mar. Chem. 32: 51-71.

[9] John I. Hedges and Fredrick G.Prahl (1993) Early diagenesis consequence for applications of molecular biomarkers. In: Organic Geochemistry Principle and applications. (Edited. Michael H. Eegal and Stephen A. Macko) Plenum Press, New York, pp 861.

[10] Eglinton G., Parkes R. J. and Zhao M. (1993) Lipid biomarkers in biogeochemistry : future roles?*Marine Geology*, 113: 141-145.

[11] Meyers P. A. (1997) Organic geochemical proxies of paleoceanographic, paleolimnologic and paleoclimatic processes. *Org. Geochem.* **27** (5/6) 213250.

[12] Hayes J.M., Takigiku R. And Ocampo R. *et al.* (1987) Isotopic composition and probable origins of organic molecules in the Ecocene Messel shale.*Nature*, 329: 48-51.

[13] Blumer M., Guillard R.P.L. and Chase T. (1971) Hydrocarbons in marine phytoplankton. *Mar. Biol.*, 8: 183-189.

[14] Nishimoto S. (1974) A chemotaxonomic study of n-alkanes in aquatic plants. J. Sci. Hiroshima Univ. Ser. A. 38: 159-163.

[15] Wakeham S.G. (1990) Algal and bacterial hydrocarbons in particulate matter and interfacial sediment of the Caria co Trench. *Geochim. Cosmochim. Acta.*, 54: 1325-1336.

[16] Didyk B.M., Simoneit B.R.T. and Brassell S.C., *et al.* (1978) Organic geochemical indicators of

paleoenvironmental conditions of sedimentation. *Nature*, 272: 216-222.

[17] Deng H. W., Qian K. (Edited) (1993) Sediments geochemistry and environmental analysis, Science and Technology Press of Gansu, Lanzhou.

[18] Organic geochemsitry and sedimentology groups of Acedemic Society of China (1982) Organic geochemsitry, Science press, Beijing.

[19] Pererira W. P., Hostettler F .D. and Luoma S. N. *et al.* (1999). Sedimentary record of anthropogenic and biogenic polycyclic aromatic hydrocarbons in San Francisco Bay, California. Mar. Chem., 64 99113.

[20] Wakeham S. G. (1996) Aliphatic and polycyclic aromatic hydrocarbons in Black Sea sediments. *Mar. Chem.*, 53: 187-205.

[21] Sanders G., Hamilton-Taylor J. and Jones K. C. (1996) PCB and PAH dynamics in a small rurla lake. *Environmental Science Technology*, 30: 2958-2966.

[22] Latimer J. S., Quinn J .G. (1996) Historical trends and current inputs of hydrophobic organic compounds in an urban estuary: the sedimentary record. *Environmental Science Technology*, 30: 623-633.

[23] Heras X., Garrimalt O., Albaiges J. *et al.* (1989) Origin and diagenesis of the organic matter in Miocene freshwater lacustrine phosphate (Cerendya Basin Eastern Pynerees).*Org. Geochem.*, 14: 667-677

[24] Matsuda H. And Koyama T. (1977) Early diagenesis of fatty acids in lacustrine sediments from recent sediments and some source materials. *Geochim. Coschim. Acta.*, 41: 1825-1834.

[25] Lajat M., Saliot A., Schimmelmann A. (1990) Free and bound lipids in recent (1835-1987) sediments from Santa Barbara Basin. Org. Geochem., 16: 793-803.

[26] Venkatesan M.I. and Mirsadeghi F.H. (1992) Coprostanol as sewage tracer in McMurdo Sound, Antarctica. Marine Pollution Bulletin, **25** (9-12): 328-333.

[27] Kvenvolden K.A., Rapp J.B. and Margaret G. *et al.* (1987) Multiple sources of alkanes in Quaternary oceanic sediment of Antarctica. *Org. Geochem.* **11** (4): 291-302.

[28] Matsuda H. And Koyama T. (1977) Early diagenesis of fatty acids in lacustrine sediments---Identification and distribution of fatty acids in recent sediments from a freshwater lake. *Geochim. Cosmochim. Acta*, 41: 777-783.

[29] Ioanna Bouloubassi and A. Saliot (1993) Investigation of anthropogenic and natural organic inputs in estuarine sediments using hydrocarbon markers (NAH, LAB, PAH). *Oceanologica Acta.* **16** (2): 145-161.

[30] Farrington J.W. and Quinn J.G. (1973) Biogeochemistry of fatty acids in recent sediments from Narragansett Bay, Rhode Island. *Geochim. Coschim. Acta,* 41: 289-296.

[31] Colombo J.C., Gearing J.N. and silverberg N. (1996) Lipid biogeochemsitry in the Laurentian Trough: fatty acids, sterols and aliphatic hydrocarbons in setting particles. Org. *Geochem.* 22: 211-225.

[32] Ackman R.G., Tocher C.S. and MsLachlan J. (1968) Marine phytoplantkton fatty acids. *J. Fish. Res. Bd. Can.*, 25:1603-1620.

[33] Didy B. M., Simoneit B .R. T. and Brassell S. C., *et al.* (1978) Organic geochemical indicators of paleoenvironmental conditions of sedimentation. *Nature*, 272: 216-222.

[34] Reed W.E. and Kaplan I.R. (1977) The chemistry of marine petroleum seeps. *J. Geochem. Explor.* 7: 255-293.

[35] Bouloubassi I. and A. Saliot (1991) Source and transport of hydrocarbons in the Rhone delta sediments (Northwestern Mediterranean). Fresenius J. anal. Chem., 339: 765-771.

[36] Meyers P.A. and Ishiwatari R. (1993) Lacustrine organic geochemsitry an overview of organic matter sources and diagenesis in lake sediments. *Org. Geochem.*, **20** (7): 867-900.

[37] Colombo J.C., Silverberg N. And Gearing J.N. (1997). Lipid biogeochemistry in the Laurentian Trough Changes in composition of fatty acids, sterols and aliphatic hydrocarbons during early diagenesis.*Org.*

Geochem., **26** (3/4): 257-274.

[38] Colombo J.C., Silverberg N. And Gearing J.N. (1996) Biogeochemsitry of organic matter in the Laurentian Trough Bulk composition of the sediments and relative reactivity of major components during early diagenesis. *Mar. Chem.* **51**: 295-314.

[39] Canuel E.A. and Martens C.S. (1996) Reactivity of recently deposited organic matter; Degradation of lipid compounds near the sediments-water interface. *Geochim. Cosmochim. Acta*, **60** (10): 1793-1806.

[40] Gong C. and Hollander D. J. (1997) Differential contribution of bacteria to sedimentary to organic matter in oxic and anoxic environments, Santa monica Basin, California. *Org. Geochem.*, **26** (9/10): 545-563.

[41] Leeheer M. J. and Meyers P.A. (1984) Comparison of lipid character of sediments from the Great Lakes and the Northwestern Atlantic. *Org. Geochem.* **7**: 141-150.

[42] Reemtsma T. And Ittekkot V. (1992) Determination of factors controlling the fatty acids composition of setting particles in the water column by principal-component analysis and their quantitative assessment by multiple regression. *Org. Geochem.*, **18** (1): 121-129.

Phosphorous Forms in Sediments and Their Distribution in the Yangtze Estuary and Coastal Areas

Liu Min* (刘 敏), Xu Shiyuan (许世远), Hou Lijun (侯立军)and Ou Dongni (欧冬妮)
Department of Geography, Open Laboratory of Urban Environmental Dynamic Process of the Ministry of Education, East China Normal University, Shanghai 200062

Abstract Based on analyses of surface and core sediments in the tidal flats of the Yangtze Estuary and coastal areas, the present study reveals phosphorous forms existing in sediments and their distributions. The results show that phosphorus in tidal flat sediments in the study area mainly consists of inorganic phosphorous forms, involving DP, Fe-P, Al-P, and Ca-P and organic phosphorous forms. in which Ca-P and OP are dominant compositions. This finding indicates that spatial distributions of various phosphorous forms are related to sedimentary environments in water and grain sizes of sediments. and are influenced by sewage discharges and effluents from aquacultivation in the coastal areas.

Keywords phosphorous forms, distribution, tidal flat sediments, the Yangtze Estuary

Estuarine sediments are important sinks for nutrients, showing an intense environmental purification function to the overlying water. Moreover, the estuarine and coastal area, located in the land-sea transitional zone, is a typical environmentally vulnerable zone. Various environmental factors are changeable and complex. Sediments in the estuary can serve as nutrient sources at a certain content and release various forms of phosphorus nutrient into the overlying water[1,2]. As a result, it may be an important influencing process for the formation of water eutrophication.

In recent twenty years, water eutrophication contamination gets more serious in the Yangtze estuarine water. Bloom occurs often[3]. Results have shown that phosphorus in the Yangtze estuarine water is a critical limitation factor of eutrophication production[4].Various bound-forms of phosphorus in sediments have different bioavailabilities, and show potential impacts on the production of water eutrophication [5,6].Therefore, the study of various forms of phosphorus in the Yangtze estuarine and coastal tidal flat sediments has significant environmental effect. There are presently little data about it. The objective of this present study is to analyze phosphorus forms and concentration levels in surface and core sediments, and to explore the impacts of environmental factors on distribution of sediment phosphorus forms, and also to provide basic data for the study of estuarine sediments as internal sources releasing into the overlying water.

1 Sample collection and experimental method

Surface sediment samples (0~5cm) were taken from different types of sedimentary environments in the Yangtze estuarine and coastal tidal flats in March 1998 and May 2000, involving Liuhekou

* Corresponding author. Tel.: 021-62232416; fax:021-62232416.
E-mail address:mliu36@public9.sta.net.cn

(LHK), Shidongkou (SDK), Jiuduansha (JDS), Bailonggang (BLG), Caoyang Farm (CY), Donghai Farm(DH), Luchaogang (LC), Liaoyuan (LY), Fenxin (FX), Caojing (CJ) and Jinshan (JS) sites (as shown in Fig.1). Samples are frozen prior to analysis and experiment. Selected samples were then air -dried at room temperature, ground and homogenized to a fine power with a motar and pestle, and through a brass sieve (200 mesh).

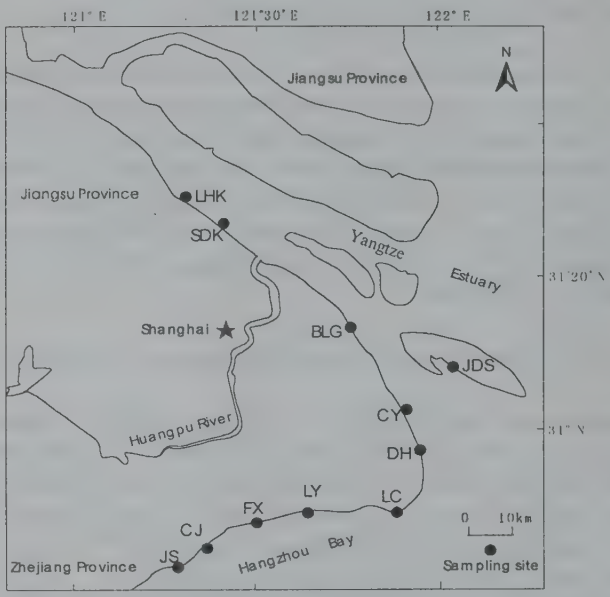

Fig. 1 Sampling sites in the study area

Presently, the analytic methods of phosphorus forms are different largely due to different study methods and aims. This study mainly classifies the phosphorus forms in sediments into five components, involving dissolved phosphorus (DP), Al-bound phosphorus (Al-P), iron-bound phosphorus (Fe-P), calcium-bound phosphorus (Ca-P) and organic phosphorus (OP). The details are as follows.

Sequence extractions for inorganic phosphorus are: ① DP:1g of sediment sample added to 50ml 1mol/l NH_4Cl , is extracted and determined as DP; ② Al-P: The sediment extracted by NH_4Cl , added to 50ml 0.5mol/l neutral NH_4F, is determined as Al-P; ③ Fe-P: The sediment extracted with neutral NH_4F, and added to 50ml 0.1mol/l NaOH is extracted and determined as Fe-P; ④ Ca-P: The sediment extracted with NaOH , and added to 50ml 0.5mol/l H_2SO_4, is extracted as Ca-P. The total inorganic phosphorus is the sum of four kinds of phosphorus forms.

OP: First, the organic matter in sediments is oxidized with H_2O_2, and added to by diluted hydrochloric acid and NH_4F, then is extracted for phosphorus determination. Secondly, sediments added to NH_4F are extracted and also determined as phosphorus. The difference of phosphorus amounts between both front and back is OP. The sum of OP and IP is the total phosphorus.

The above extractions are determined by the standard analytic method with 722-type grating spetrophotography at wavelength 700nm. The experimental error is within 10%. Sediment grain sizes are determined using the LS100Q laser particle meter.

2 Results and discussion

2.1 Concentration, distribution and variation of phosphorus in surface sediments

2.1.1 Distribution of TP

TP in tidal flat sediments ranges from 692.80~1 444.96 μg/g (Table 1).The distribution of TP in the coastal zone is characterized by multi-peak value variations. High values occur at FX, LY, BLG, SDK and LHK sites, showing different phosphorus origins. Peak values of TP are mainly affected by river sewage discharges and aquacultivation while domestic and industrial sewage inputs may be responsible for higher concentrations at BLG and SDK sites based on their spatial distribution. High concentration of TP at LHK are possibly related to nearby runoff inputs. In comparison with the river water, environmental factors in the estuarine and coastal area change intensively, so that the variation of sediment phosphorus in tidal flats is complex. Phosphorus is concentrated in sediments under a suitable environmental condition, and, otherwise, it could release from the sediments into the overlying water.

2.1.2 Distribution of IP

The concentration of IP in the study area varies from 220.03~980.53 μg/g, occupying 31.8~67.9% of the total phosphorus. IP includes DP, Fe-P, Al-P and Ca-P (see Table 1)

Tab. 1 Concentration of phosphorus forms in surface sediments in the Yangtze estuarine and coastal tidal flats (μg/g)

Sampling site	DP	Al-P	Fe-P	Ca-P	OP	IP	(Al+Fe)-P	TP
LHK	1.17	7.94	13.28	635.78	537.05	658.17	21.22	1195.22
SDK	0.23	4.36	20.42	593.81	624.52	618.82	24.78	1243.34
JDS	0.80	12.56	1.16	205.51	472.77	220.03	13.72	692.80
BLG	4.51	34.75	34.75	593.90	506.43	667.91	69.50	1174.34
CY	4.49	12.32	3.51	554.22	416.68	574.54	15.83	991.22
DH	2.04	9.69	33.94	463.91	462.74	509.58	43.63	972.32
LCG	1.13	5.65	11.55	593.81	422.23	612.14	17.20	1034.37
LY	3.22	46.69	0.08	598.08	489.95	648.07	46.77	1138.02
FX	1.13	1.90	38.22	939.28	464.43	980.53	40.12	1444.96
CJ	2.98	6.74	26.91	514.51	344.39	551.14	33.65	895.53
JS	8.95	14.35	34.75	424.33	380.73	482.38	49.10	863.11

The concentration of DP is correlated with the sedimentary environment. Ferric phosphate in surface sediments is reduced for ferrous phosphate, and releases PO_4^{3-}[8] . Therefore, DP is rare in land soils while nearby coastal sediment phosphorus is an important form of inorganic phosphorus[9]. The distribution of DP ranges from 0.23~8.95 μg/g in the study area. The high concentration level occurs at JS, BLG and CY sites, with concentrations of 8.95, 4.51 and 4.49 μg/g respectively, having a high

affinity with the high reduction environment.

In addition, Tables 1 and 2 show that fine particles are suitable for DP adsorption, so most of the coastal sediments have high concentrations of DP. The concentration of (Fe+Al)-P ranges from 13.72~69.50 μg/g, occupying 1.7~5.9% of TP and showing a close correlation with sediment grain sizes (r =−0.60, α=0.05). The tidal flat fine particle sediments have high concentrations of Fe-P and Al-P due to large surface areas and strong adsorption abilities as shown in Fig.2. Fe-P exhibits a high concentration level near contamination sources (High concentration of Fe-P occurrs at DH site. The reason for this may be that the fine particles are suitable for adsorption and enrichment of Fe-P). This is consistent with Xu Jinshu's report[7], showing that Fe-P can be taken as an indicator of sedimentary quality.

Tab. 2 Analytic results of sediment grain sizes

Sampling site	Grain size accumulation percentage (%)				Mφ (μm)
	< 4 μm	< 16 μm	< 32 μm	< 63 μm	
LHK	5.06	9.95	13.0	21.6	110.90
SDK	3.02	5.56	6.42	8.26	135.10
JDS	4.05	8.1	15.2	57.6	82.03
BLG	24.3	65.3	88.7	98.5	10.71
CY	5.07	9.18	16.3	59.26	78.73
DH	39.8	80.7	92.0	98.0	6.90
LC	21.5	51.3	77.6	96.6	15.39
LY	9.5	15.3	20.91	65.2	30.41
FX	7.27	12.5	18.8	62.9	54.99
CJ	21.6	50.1	76.9	97.1	15.97
JS	27.2	63.4	85.4	98.0	10.36

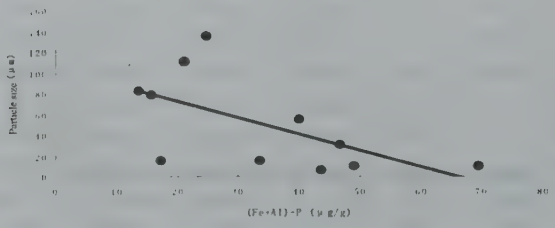

Fig. 2 Correlation between the sediment grain size and (Fe+Al) -P

Ca-P in the study area varies from 205.519~39.28 μg/g, occupying 87.979~7.00% of the inorganic phosphorus and the mean value is 93.53%. In comparison with other inorganic phosphorus , Ca-P is dominant in inorganic phosphorus. This suggests typical marine sediments. Ca-P concentration mainly depends on water acidity and alkalinity. High acidity-alkalinity is suitable for the deposit of Ca-P.

Except Ca-P is only 205.51 μg/g at JDS, it is higher than 400 μg/g at other sites. The reason may be that JDS is located in the sea-land interactive zone, where the acidity-alkalinity changes violently, while in other areas it is relatively stable.

2.1.3 Distribution of OP

The concentration of OP in the study area ranges from 344.39~624.52 μg/g, occupying 32.14%~68.24% of TP. OP is an important form in sediments. The OP concentration is affected by inputs, sediment characteristics, early disgenesis and organisms. The concentration levels of OP are high at SDK, LHK, BLG and LY, reflecting obvious effects of phosphorus inputs on them.

2.2 Phosphorus concentrations in core sediments

2.2.1 Vertical variations in core samples

The total phosphorus concentrations at the SDK and CY sites are 890.65~2 145.28 μg/g and 1 033.651~615.32 μg/g respectively. However, the mean concentration at SDK is higher than that of CY. It reflects large spatial differences of phosphorus inputs due to different geographical and geomorphological locations. The total phosphorus concentrations at both sites are characterized by being lower in the surface and bottom sediments, and higher in the subsurface sediments (Fig.3 and 4). The trend of TP variation is consistent with that of OP, showing that OP is the main factor in controlling the change of TP.

The organic phosphorus concentrations at the SDK and CY sites vary from 642.66~1 218.04 μg/g and from 550.60~1 078.53 μg/g, respectively. The variation trends of OP at both sites are similar, being lower in the surface and bottom sediments, and higher in the subsurface sediments (Fig.3 and 4). The above indicates that the OP concentration in surface sediments is mainly controlled by mineralization while the OP concentration in bottom sediments are possibly related to the lower phosphorus inputs.

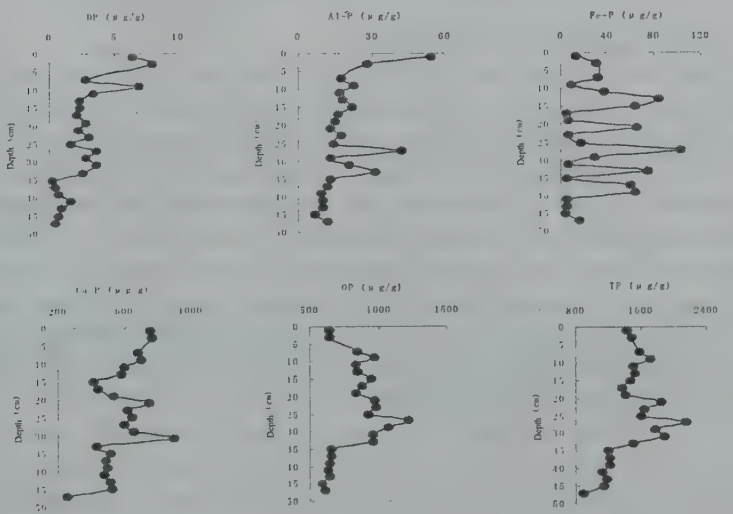

Fig. 3 Variation of phosphorus forms in SDK core sediments with depth

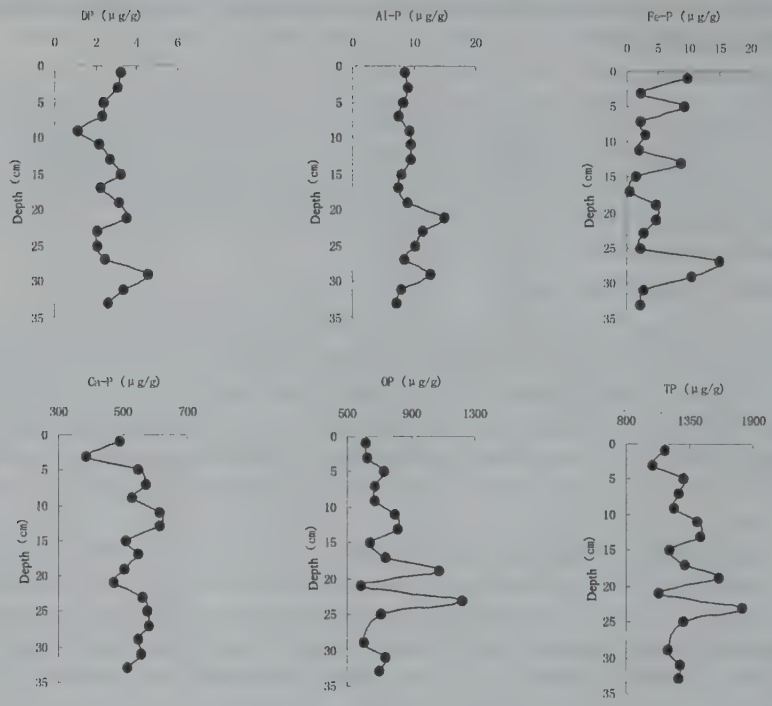

Fig. 4 Variation of phosphorus forms in CY core sediments with depth

2.2.2 Vertical variation of various phosphorus forms

IP includes mainly the four kinds of DP, Al-P, Fe-P and Ca-P. Results indicate that Ca-P is a dominant component in IP at SDK and CY sites, occupying 90.72% and 96.87%, respectively. However, DP, Al-P and Fe-P are scarce in IP. This finding shows that the relation of particle sizes and phosphorus forms in sediment cores is changeable and complex. The concentration of inorganic phosphorus is not obviously correlated with 4~63 μm particle sizes. The vertical distribution of Ca-P is consistent with that of the particles larger than 63 μm at SDK core (Fig.5and 6), while there is no obvious correlation between the two at the CY core profile. The distributions of DP and Al-P are related closely to the particles less than 4 μm. The vertical variation of Fe-P is complex and has no obvious correlation with grain sizes, similar to the previous references[10,11] .The study reveals that the vertical variations of phosphorus forms with depth are susceptible to multi-factors, such as sedimentary environment, early diagenesis, grain sizes and anthropogenic activities.

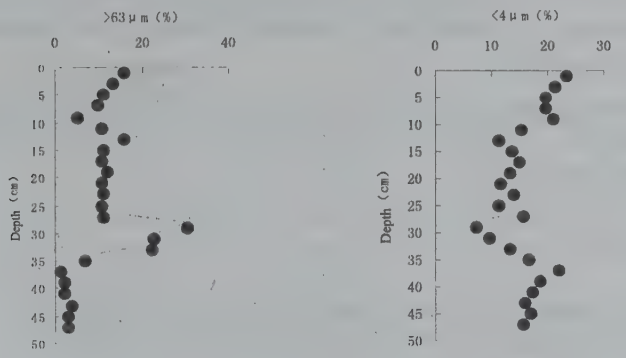

Fig. 5 Vertical variations of different grain size percentage from SDK core sediments

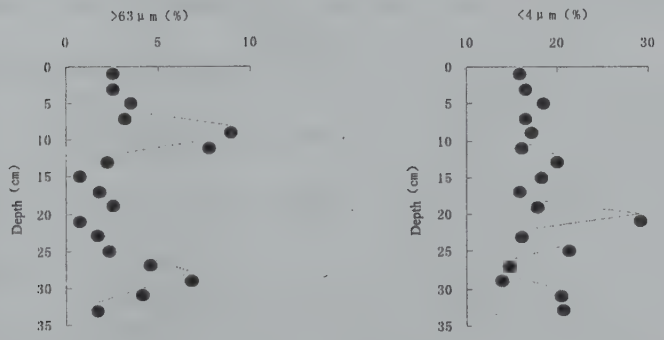

Fig. 6 Vertical variations of different grain size percentage from CY core sediments

3 Conclusion

3.1 Phosphorus forms of tidal flat sediments mainly have five kinds, involving OP, DP, Al-P, Fe-P and Ca-P in the Yangtze estuarine and coastal areas. OP and Ca-P are main phosphorus forms of coastal sediments due to the effects of human activities and coastal water environmental conditions.

3.2 The spatial distribution of phosphorus forms in surface sediments is related to their environmental geochemical behaviors and is controlled by regional differences of sewage discharge intensity. The concentrations of sediment phosphorus forms have high affinities with fine particle size contents. In most coastal areas the finer the particle sizes are, the higher the concentrations of phosphorus forms are.

3.3 The vertical variations of phosphorus forms in sediments are quite complex and obviously different in different geographical and geomorphological positions due to the effects of human activities and coastal water environmental conditions. And there exhibits a complex correlation between grain sizes in core sediments and phosphorus forms.

3.4 Fe-P concentrations nearby the sewage discharge outlets are obviously higher than those at the non-sewage discharge outlets, suggesting that Fe-P concentration can be regarded as an indicator for identifying sediment quality.

Acknowledgements

The work is supported by the National Natural Science Fund of China (Grant Nos.49801018 and 49771101), and Fund for University Key Teachers by the Ministry of Education.

References

[1] Klump, J.V., Martens, C.S. (1981) Biogeochemical cycling in an organic rich coastal marine basin-II: Nutrient sediment-water exchange processes. Geochimica et *Cosmochimica Acta*, 45:101-121.

[2] Yin Daqiang, Qin Qiurong, Yan Hang (1994)Effects of environmental factors on phosphorus release from sediments of Wulihu Lake. *Journal of Lake Science*, 6:240-244.

[3] Chen Jiyu (ed.) (1988) Integrated investigation report on Shanghai coastal zone and tidal flat resources. Shanghai Science and Technology Press, 122-123.

[4] Edmond., J. M., Spivack, A., Grant, B.C., *et al.* (1985) Chemical dynamics of the Changjiang Estuary. *Continental Shelf Research*, 4: 17-36.

[5] Han Weiming (1992) Phosphorus release from bottom sediments and effects on eutrophication. Environmental Science, **13** (3): 25-29.

[6] Hua Zhaozhe, Zhu Xiaoqing, Wang Xiaorong (2000) Study on bioavailability of *Selenastrum capricornutum* influenced by released phosphorus. *Acta Scientiae Circumstantiae*, **20** (1):100-105.

[7] Jin Xiangcan, Tu Qingying (eds.) (1990) Investigation Principle on lake eutrophication. Second edition. China Environmental Science Press, 208-238.

[8] Shang Shaoling, Hong Huasheng (1996) The study of phosphorus in Western Xiamen sea area. *Marine Environmental Science*, **15** (1): 15-21.

[9] Xu Jinshu, Li Liangge (1990) Existing forms of phosphorus in sediments from Middle and Northern Taiwan Strait. *Oceanologia et Limnologia Sinica*, **21** (1), 62-69.

[10] Lin Ronggeng, Wu Jingyang (1992) Forms of inorganic phosphorus in the sediments near the the Huanghe River Estuary. *Oceanologia et Limnologia Sinica*, **23** (4): 387-395.

[11] Bao Gengde, Huang Depei, Wang Yifan *et al*. (1984) A preliminary study of organic matter, N and P in coastal sediments from the shallow waters of the East China Sea. *Donghai Marine Science*, **2** (1): 15-21.

Relation between Gravity Field Feature and Tectonics and Earthquakes in Taiwan and Its Adjacent Seas

Zhang Chijun (张赤军), Fang Jian (方 剑)
Institute of Geodesy and Geophysics, Chinese Academy of Sciences, Wuhan 430077

Abstract Short wave gravity anomaly is correlated to sea floor topography in the gravity field of Taiwan and its adjacent seas. Gravity values of 200×10^{-5} ms^{-2} at Yushang and -160×10^{-5} ms^{-2} at Liuqiu sea trench are respectively the maximum and minimum gravity values in this area. Bouguer gravity anomaly reflects not only Moho interface undulation, but also fault distribution. The inflexion of gradient belt of Bouguer gravity anomaly is a spot liable to earthquakes . Middle-long wave geoid is the best data to invert crustal thickness. We calculate crustal thickness by using geoid data, and the maximum value is 38km; the minimum value is 12km in Taiwan and its adjacent seas.

Keywords Taiwan, gravity, crustal Thickness, earthquake activity

1 Preliminary discussion on the characteristics of gravity anomaly and field source

In Taiwan Island and its adjacent sea region of China the strike of free-air gravity anomaly is basically NNE, which agrees with the submarine relief,and the variation of anomaly amounts to 3060×10^{-5} m/s^2. The central part of Taiwan is covered by mountains passing through from north to south and the form of the free-air gravity anomaly in there is basically consistent with that of the mountains.In the Mount Yu area, the elevation of which is the highest, the free-air gravity anomaly is over 200×10^{-5} m/s^2. There are obvious gravity gradient zones on both sides of the mountain, which is related to the fault that goes along N-S. The minimum gravity anomaly amounts to 160×10^{-5} m/s^2, tens of kilometres away from the east side of Hualian harbor. There the anomaly changes suddenly from positive to negative. Thus, it shows the feature of the boundary between oceanic crust and continental crust. In addition, the anomaly extends further southeastwards, which reflects the form of Ryukyu Trench. The effect of the topographic mass of Huosao Island and Xiaolan islet makes the free-air gravity amomaly postive.

The depth of the Taiwan Straits is not large and its variation is small, from 10m to 80m, where the spread of free-air gravity anomaly Δg, is different from that in Taiwan Island region; This anomaly spreads out gently and the majority is positive and changes between $20\sim40\times10^{-5}$ m/s^2, because this anomaly is conditioned by the shoals of the Penyhu and Taiwan Islands where the water depth is only over 10m. In the Jinmen Island region to the east of Xiamen City the free-air anomaly reaches 20×10^{-5} m/s^2 as well.

In short, the free-air gravity anomaly is controlled by the height of relief and water depth. Therefore, in this sense, the height of relief and water depth can be inversed by the free-air anomaly with short wave length but the deep tectonic cannot.

For further exploration into the distribution of field sources we can study the spectral structure of

Supported by NSFC (No.49874016)

gravity field, i.e. the characteristics of the window field of different orders. It is known from the calculation of the model of 360 orders that in the whole field from 2 to 360 orders the Δg_f in the central mountainous areas of Taiwan amounts to (175~200) $\times 10^{-5}$ m/s^2, which approaches the data surveyed on earth surface. The reason why this value is less than 200×10^{-5} m/s^2 is that the resolution rate of the model is not high enough, i.e., the model does not reflect completely the substance distribution on the ridge of the central mountains. The gravity anomaly in the western flat of the Taiwan Island is (50~75) $\times 10^{-5}$ m/s^2, 25×10^{-5} m/s^2 in the strait zone, and (−150~175) $\times 10^{-5}$ m/s^2 near 23.5°N, 122.5°E . All of the above demonstrate that the results surveyed in the field and obtained by gravity field model are close to each other.

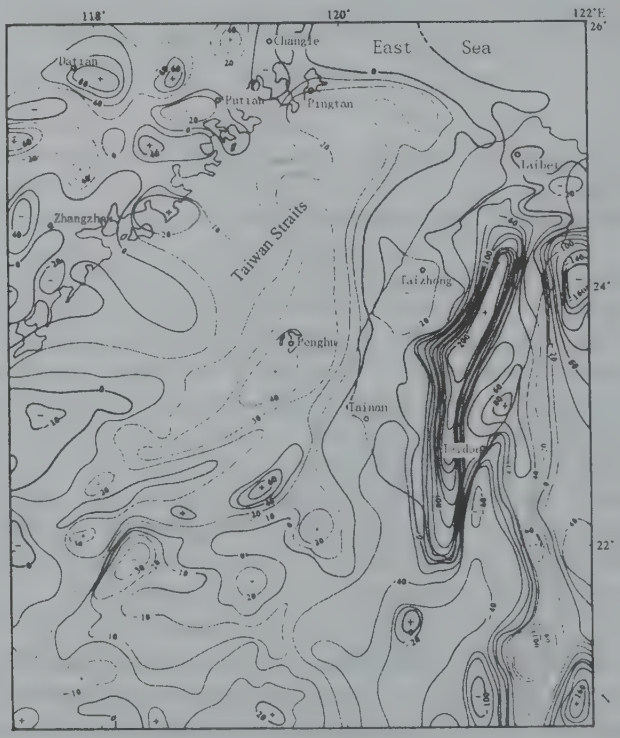

Fig. 1 Free gravity anomaly of the Taiwan Straits and its adjacent sea (after Reference [1])

If the anomaly is calculated only by the model orders of 180, then in the middle of Taiwan Island it is 80×10^{-5} m/s^2, which is rather low by comparison with the result by the model of 360 orders; near 23.5°N, 122.5°E, the anomaly is only -110×10^{-5} m/s^2. Both of the values at these two sites are smaller than that obtained by the model of 360 orders. It is basically owing to the fact that the resolution of that

model is only 1×1. However the sea floor of the Taiwan Straits is comparatively flat, so the results by the models of 180 orders and 360 orders are consistent with the surveyed data.

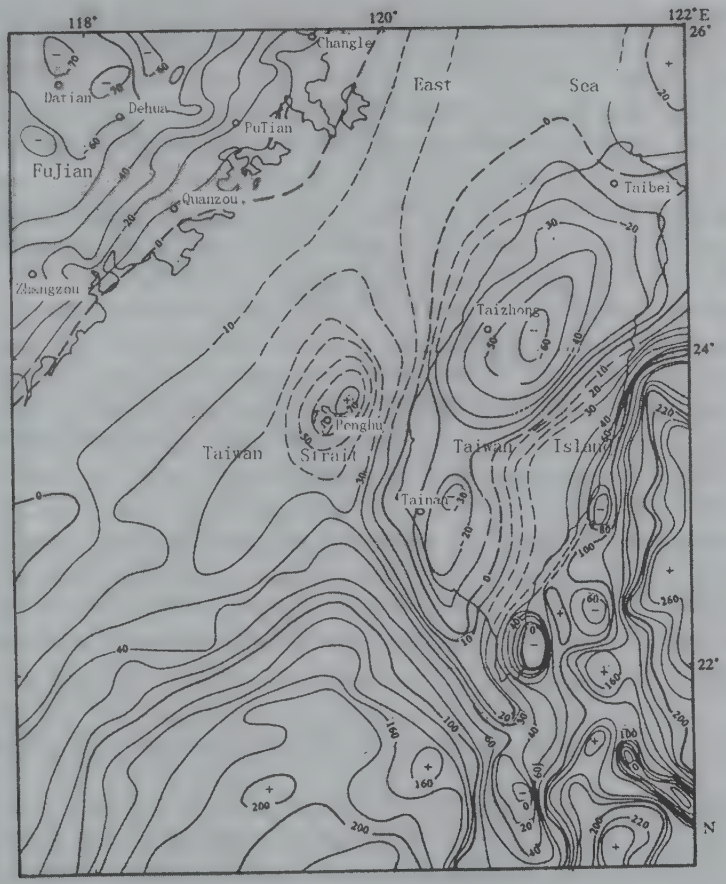

Fig. 2 Bouguer gravity anomaly of the Taiwan Straits and its adjacent sea (after Reference [1])

If we take n =2~49 orders, then the gravity anomalies in Taiwan Island and Taiwan Straits will be almost the same and the values can amount to 15×10^{-5} m/s^2 but the anomaly at 23.5° N,122.5° E is only -10×10^{-5} m/s^2; if n =50~100, then within Taiwan Island the anomaly will amount to 50×10^{-5} m/s^2; at 23.5°N, 122.5°E it is 50×10^{-5} m/s^2. When n =100~180, then the anomaly will be -80×10^{-5} m/s^2 at (23.5°N, 122.5°E and 15×10^{-5} m/s^2 in other regions. From the above analysis it is known that for the field of 2~49 orders the anomalies on the both sides are almost the same. This means that the field of low order is not influenced by the substance of shallow field source, but for the field of middle order (n =50~100) the rather shallow field source has certain influence on gravity field, and for that of n =180 and

even n =100~360 the shallow and very shallow field sources, such as high mountain, abyss and the like terrain mass all influence the Δg_f significantly.

It can be seen from Fig.2 that the distribution of the Bouguer gravity anomaly has high correlation to submarine depthand land relief elevation in Taiwan Island, the maximum amounting to-60×10^{-5} m/s^2. The higher the mountain is, the larger the negative value will be. Besides the assumption that we take the Bouguer layer in the correction term as infinitely great plate causes negative value and the crust thickening is another cause. The shape of thickening crust is approximately an ellipse; its strike is NNE but not as clear as that of the free-air anomaly that spreads along the mountains. In the sea to the east of Taiwan (23.5°N, 122.5°E)the anomaly is very clear in the map of Bouguer anomaly because the depth (h) amounts to more than 4000m and the correction between the layers is positive (0.0686H)[3] and its strike is consistent with that of the ocean bottom depth. A small closed anomaly near Eluangbi at the southern tip of Taiwan Island occurs, its magnitude amounting to 40×10^{-5} m/s^2.

On the boundary between Taiwan Island and the Taiwan Straits the Bouguer anomaly is close to zero. But in the Penghu Islands and Taiwan Shoal a positive closed anomaly exists. The maximum in the Penghu Islands amounts to 20×10^{-5} m/s^2, which we think is similar to the free-air anomaly that results mainly from local relief mass including the Xiapeng Tensile Depression, Penghu uplift etc. This means that the gravitational mass exists under a survey point and the elevation of the point is small, thus all of these factors make the practical gravity value larger than normal. In general, the Bouguer anomaly is distributed in a zone, its strike is also NNE and its value gets larger and larger as it goes east. The anomaly reflects basically the spread of the crust thickness in the transitional zone between the land and ocean. In addition, the crust becomes thinner and thinner as it goes farther away from the bank. Corresponding to this, the substance of upper mantle of high density is comparatively nearer to the water surface. On the basis of this phenomenon scientists often invert the thickness of the land (ocean) crust with Bouguer gravity anomaly.

2 Characteristics of the geoid and inversion of the Moho undulation from them

On the seas and oceans the quasigeoid coincides with the geoid. Therefore the elevation anomaly is exactly the undulation of geoid. In Fig.3 the geoid EGM-96 appears to be the same as the 3 following results which are obtained by the earth gravity field model (including surface gravity), the gravity field model improved by satellite altimetry and the calculated result from the satellite altimeter. On the basis of the above results it can be seen that no matter what methods or models are used to calculate the geoids they should be consistent with or close to each other because all of them reflect the same distribution of field sources. From Fig.3 it can also be seen that the distribution and strike of geoid are close to those of the tectonic in the adjacent area, and that its strike also is NNE. The change of geoid at the southeastern corner of the coast of Fujian is 7m, and that at the southeast corner of Taiwan Island is 22m. The difference in the section spreading about 70km amounts to 15m, and the horizontal gradient rate is 0.1%. Along the latitude line 21°N eastwards, the changing value increases to 32m. It is controlled by the thickness of ocean crust. But on the eastern side of the Taiwan Island the geoid is so strongly influenced by sea-floor abyss that in some area (its center is at 23.5°N, 122.8°E) many closed circles of elevation anomaly isoline are formed and the nearer it is to the center the less the value is (amounts to 16m). This suggests that the abyss is of symmetry like the bottom of a cooking pot.

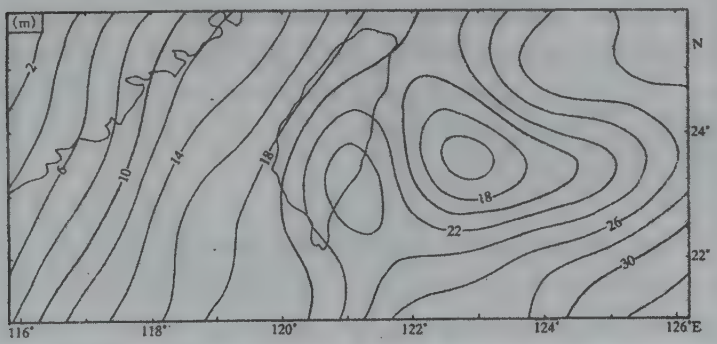

Fig. 3 Geoid anomaly calculated from EGM96 Model

If we simulate this course by the Airy compensation model, then the geoidal anomaly in a sea area can be calculated from depth by the following formula.

$$\Delta N = \frac{\pi G}{g}(\rho_c - \rho_\omega)[2Hh + (\frac{\rho_m - \rho_\omega}{\rho_m - \rho_c})h^2] \quad (1)$$

Where G is the gravitation constant; g is gravitational acceleration; H is average crust thickness; h is relief elevation or sea depth; ρ_m , ρ_c , ρ_w are the densities of the crust, mantle and water respectively and we take $\rho_m = 3\,300\,\mathrm{kg/m^3}$, $\rho_w = 1\,000\mathrm{kg/m^3}$, $\rho_c = 2\,800\mathrm{kg/m^3}$, $H = 30\,km$. Taking the disturbance from the abyss of 6 500m depth to the geoid into account, we can calculate the ΔN by formula (1). Here, taking the average depth as 3 300m, we will obtain ΔN =−5.5m, then subtract the ΔN from the anomaly in the center of this area and decrease progressively outwards, thus the ideal form of the geoid can be recovered. Consequently this form of geoid will benefit the inversion of crust thickness from geoid. The depth to the southwest of Taiwan near 21°N, 120°E changes considerably where it amounts to 3 383m. The abyss also causes the geoid to bend in strike trend. As regards the land, it can be seen from Fig.3 that near the central mountains of Taiwan Island the undulation of the geoid is 25m, 5m higher than that of coastal zone . The relative change results from the mountain body mass. The load of mountain body for a long time makes the rock layer flex and results in isostatic compensation. Thus we can calculate the geoid anomaly by the following formula:

$$\Delta N = \frac{\pi G}{g}\rho c[2Hh + \frac{\rho_m}{\rho_m - P_c}h^2] \quad (2)$$

Taking the above parameters and average height as 1500m, we have ΔN =4.8m. It is evident that this value is close to the real relative height of 5m (Fig.3).

If we only consider the relationship between the undulation of interface and the geoid, then the anomaly can be expressed in the following equation:

$$\Delta N(r) = \frac{G\Delta\rho}{g}\int_t \frac{d\upsilon}{|r - r'|} \quad (3)$$

where, r, r' are the radius vectors of the calculated point and the moving body element, $\Delta\rho$ is the difference of densities and $d\upsilon$ is the integral body element.

After the general field has been calculated by EGM-96, only if the difference between the densities of crust and mantle $\Delta\rho$ is known, the crust thickness can be inverted from the general or local field of the geoid and the inversion formula turns into the following.

$$\Delta N(r) = \frac{G}{g}\Delta\rho \sum \Delta\Omega(r') \int_{z_b}^{z_t} \frac{dz}{|r - r'|} \tag{4}$$

Where z_b, z_t are the bottom and top interfaces of the mass element; $\Omega(r')$ is the integral surface element, and the formula (4) can be turned into the following with the method given in Reference [8] based on Fourier transform.

$$F[N(r)] = 2\pi \frac{G}{g}\Delta\rho \exp(-|k|Z_0) \times \sum_{n=1}^{\infty} \frac{|K|^{n-2}}{n!} FZ^n(r') \tag{5}$$

Where $z(r') = z_t - z_b$, k is the model of wave number, z_0 is the reference depth. If only the first term is taken into account, we have

$$F[N(r)] = 2\pi \frac{G}{g} |K|^{-1} \Delta\rho \exp(|k|Z_0) F[Z(r')] \tag{6}$$

If the isostatic compensation is not taken into amount for linear approximation, the interface $b(r)$ will be

$$b(r) = F^{-1}\{Z_N |k|^{-1} F[\Delta N(r')]\} \tag{7}$$

where

$$Z_N(k) = 2\pi \frac{G}{g} |K|^{-1} \Delta\rho \exp(-|k|Z_0) \tag{8}$$

If the compensation of lithosphere is attended to, then $z'_N(k)$ will be

$$Z'_N(k) = 2\pi \frac{G}{g} |K|^{-1} \Delta\rho \exp(-|k|Z_0) \times [1 - \frac{\exp(-|k|t_0)}{(1 + \frac{|k|D}{g\Delta\rho})}] \tag{9}$$

where, t_0 is the depth of the flexed interface and D is the rigidity of the lithosphere. Afterwards the crust thickness can be inverted by formulae (7), (8) combining the operation given in Reference [1] (see Fig. 4). In the studied area the crust thickness varies considerably, 38km, the highest, in the middle of Taiwan, 30km in the Taiwan Straits and 12km, the shallowest, in the Ryukyu Trench.

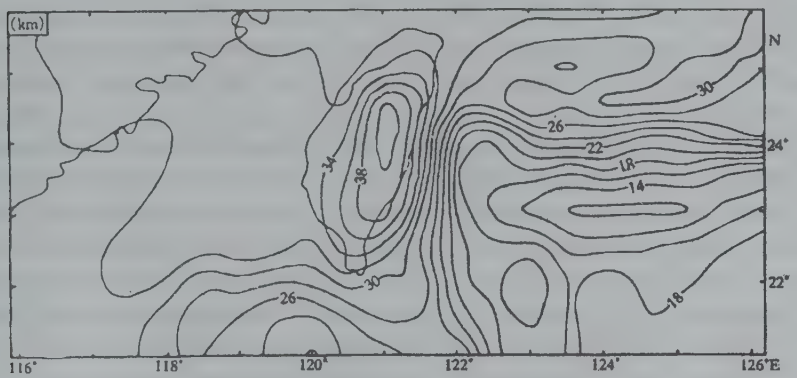

Fig. 4 Crustal thickness inverted by geoid anomaly

3 Function of gravity field in geological and geophysical studies

In respect of tectonic, the western side of the Taiwan Straits belongs to the continental shield depression zone of the East China Sea and the eastern side belongs to the continental shield rise zone. In the Miocene Epoch both zones began to deposit and the thickness of sedimente amounts generally to over 4km. The sediment of the Tertiary Period in the Xinzhu Basin of western Taiwan Plain amounts to 7 000~9 000m, and 7,000m in Taiwan Shoal. It looks as if the horizontal variation of the density within the sediment layer is not large. The positive Bouguer and free-air anomalies of certain magnitude demonstrate that in Penghu and its nearby region besides the influence of water depth the anomaly still reflects the characteristic of base uplift. In the Taiwan Straits the variation of geoid is comparatively large (near 15m), which mainly suggests that the crust thickness of continental shelf decreases progressively and the continental shelf tends to transit to the ocean crust. Since the gravitational geoid corresponding to a signal through a low-pass filter has weakened the disturbance from the mass above the Moho, the variation of the inversed crust thickness approaches the reality more than the gravity anomaly. To the southwest of Taiwan the free-air , Bouguer anomalies and the geoid all reflect clearly the variation of sea floor relief and this variation may also reflect the density variation of the crust and upper mantle after the convergence of the Philippine Plate with the Eurasia Plate. In Palaeozoic Era, Taiwan Island was a part of the Taiwan geosyncline. The volcanic rock of marine facies of the stage of Yanshan is the extension of the volcanic rock zone of continental facies in the southeast sea area of China, so the crust has the feature similar to that of the continental crust. Because the Bouguer anomaly is sensitive to the mass near the earth surface as compared with the geoid, the crust thickness nearby the Taiwan Island can be inverted by the Bouguer anomaly. But the Bouguer anomaly is liable to the disturbance from uneven distribution of the shallow mass, so we employ the geoid, which suffers less disturbance, to invert and the result is fairly good. The Moho in the middle of Taiwan caves down, and in the west plain and the strait area it is flat with a depth of 30~33km. To the east of the longitudinal valley the Moho so sharply declines that along the Lanyu Island–Lu Island its depth is only 27km. In there the crust is of a transitional type, turning from 122.5°E to the margin of the Philippine Sea basin.

The minimal crust thickness is about 12km so it is of an ocean crust type. The above results approach that calculated by the velocity of seismic P wave. Taiwan is the largest island of China, it is a Cenozoic Era fold-belt formed on the basis of geosyncline, and several N-N-E-ward reverse faults have been formed under the compression of the Philippine Plate with the Asia Plate. The whole Taiwan Island can be divided into 5 tectonic zones that are Tai-Peng depression, syncline in the west Taiwan, central anticling, longitudinal valley fault zone and eastern syncline. Although it is difficult to divide these faults and tectonic zones based on the gravity map, the existence of these faults and their overlapping effect is one of the causes which make the gradient of the Bouguer gravity anomaly increase. In the longitudinal deep fault zone (Great Longitudinal Valley) the Bouguer anomaly has varied greatly. In the west it is negative, which shows the nature of continental crust; in the east it is positive, which may indicate the transition from continental crust to ocean crust. Many geologists think that the Longitudinal Valley zone is a very deep and large trans-lithospheric fault and has the feature of a suture line. The west to it belongs to the ectonic of Cenozoic Era and the east to the Ryukyu-Okinawa Trough.

Fig. 5 Composite seismotectonic profile in Taiwan Island and its adjacent regions

In the Okinawa Trough to the northeast of Taiwan the geoid and Bouguer anomaly increase progressively, indecating that there the Moho uplifts progressively and the thickness of ocean crust decreases. The results inversed from the geoid approaches Fig.5. As mentioned above, in the Ryukyn

Trench to the east of Taiwan the free-air and Bouguer anomalies vary considerably. In there the crust thickness inversed from Bouguer anomaly is about 9km. The reason that the resulting thickness is less than that from geoid is probably the influence of the sediment on the Bouguer anomaly. On the basis of the spectral analysis of gravity the middle-long band (2~100 orders) reflecting the field source in the study area lacks clear anomaly but the part of short wave length (100~180 orders) reflects clearly and the more shallow field source (180~360 orders) reflects more clearly. All of these facts demonstrate that the gravity field in the Taiwan sea area is controlled by shallow and moderate deep field sources; consequently the sea floor relief varies on the contrary to the undulation of the Moho and in this way it is bound to bring about the special variation of gravity field and thus the crust thickness can be inversed by the anomaly or its field of total orders.

Since Taiwan and its northeastern and southeastern sea areas are part of the strong active areas of continental margin and island arc, these areas belong to the circum-Pacific seismic belt. From 1901 to 1980, 1, 019 earthquakes were recorded, 12.4 (on an average) strong quakes every year, among which there were 38 quakes of over magnitude 7. On an average, 1 quake of over magnitude 7 occurred every 2 years. Up to 1996 about 20 strong earthquakes had occurred in the Taiwan Straits. The Nantou earthquake on sept. 21, 2000 is of 7.6 , which killed 2,400 people and injured many people and caused a great property loss. By analyzing the focal mechanism of many earthquakes the principal compressive stress axis is roughly vertical to the strike of folds or faults, i.e. NW and SE strike. The reference [13] analyzes the materials of the strong earthquakes from 1906 to 1972 and points out that the principal compressive stress direction is between 108 and 149. It is known from the observations of crust movement and geological materials that the east coast of Taiwan is uplifting by 6~9mm every year and the rise in other areas occurs as well.[14] In recent years the GPS monitoring in the Taiwan region has been strengthened. It can be known from the results calculated with the data at many stations (including the GPS station at Taibei) that Taiwan in the Eurasia plate moves southeastwards relatively to the Pacific Ocean at a rate of 10cm/a.[16]

The Bouguer anomaly distributing in belts indicates that there may be a deep fault in the Fujian coastal zone, and the reference [15] considers that the fault is active. Although the earthquake frequency is not high, its intensity is high.

Generally speaking , great earthquakes occur easily along the active faults and at the intersections of fault fracture. Seeing that the large gradient of Bouguer anomaly indicates the existence of a fault and the turn of anomaly curve also reflects the change of fault strike or the influence from neighboring faults, it is evident that in the map of Bouguer anomaly, we can find out the anomaly distribution with above characteristics in Taiwan Island and the adjacent sea area, which is exactly the place where the longitudinal valley zone, the Okinawa trough, the trench on the outer side Ryukyn of and the Ryukyu arc strike-slip have thinned out. From the isostatic anomaly map in the reference [1] it can be seen that the isostatic anomaly in Taiwan and its adjacent sea region varies very much, amounting to 80×10^{-5}m/s. This shows that the crust here is in a state of unbalance and varies violently. In general, we can infer the special distribution of earthquake from the distribution of gravity anomaly. If we observe the non-tidal variation of gravity with time in Taiwan and on both sides of the Taiwan Straits and perform the corresponding crustal deformation survey, it is probable to provide the basis for earthquake prediction.

To sum up, the following conclusions may be drawn: 1) Through the spectral analysis of gravity field it is known that the distribution of the mass near the crust plays a major role. 2) For the inversion of the crust thickness using the undulation of geoid is better than using the gravity anomaly. The inversion

of the crust thickness in the east sea area to Taiwan demonstrates that the farther eastward the crust is located, the less its thickness is, but on the northern and southern sides it is quite thick. The inverted result approaches the reality in the studied area. 3) It is known from the analysis of Bouguer anomaly that the anomaly gradient zones and their turns are probably the zones where earthquake occurs easily. We should strengthen the gravity and deformation monitoring in order to contribute more to the earthquake prediction.

References

[1] The Second Geological Team of Ministry of Geology and Mineral Resources (1987). Geophysical Atlas of South China Sea[M]. Guangzhou: Guangdong People's Press.(in Chinese)

[2] Yuan, X.C. (1996). Geophysical Atlas of China[M]. Beijing: Geological Press. 161.(in Chinese)

[3] Fang Jun. (1985). Gravimetry and Earth Shape [M]. Beijing: Scientific Press, 213. (in Chinese)

[4] Huang C. L., Shu D. Q., Chen H.Z. *et al.* (1997). Synthetical Investigation of Geology, Geophysics and Geochemics in the West of the Taiwan Straits [M]. Xiamen: Xiamen University Press. 11~13.(in Chinese)

[5] Ning J. S., Li J. C., *et al.* (1994). The research of the Earths gravity field Model WDM94 complete to Degree 360[J]. *J.O.WTUSM,* **19**(4), 283~291.(in Chinese)

[6] Hwang C.W. (1999). A bathymetric model for the South China Sea from satellite altimetry and depth data [J]. *Marine Geodesy*, 22: 37~51.

[7] Turcotte,D., Schubert,G. (1982). Geodynamics[M]., New York: Wiley.

[8] Calmant S, Baudry N. (1996). Modelling bathymetry by inverted satellite altimetry data [J]. *Marine Geodesy,* 19:123-134.

[9] Yang S.N., Yang K.R. (1985). Chinese Regional Tectonics[M]. Beijing: Geological Press, 241-244.(in Chinese)

[10] Editorial Board for Geodynamical Atlas (1989) Geodynamical Atlas in China Lithosphere[M]. Beijing: Seismological Press, 40.(in Chinese)

[11] Liu G.D. (1990). Geology-Geophysical series atlas of China Sea and its adjacent regions[M]. Beijing: Geological Press, 1-25.(in Chinese)

[12] Chen X.X., Yuan D.Q., Wu C.J. (1996). Feature of *Ms* 7.3 earthquake source in south Taiwan Straits and analysis of earthquake status in the east-south sea[J]. *ACTA Seismologica Sinica.* **18**(2): 145~155.(in Chinese)

[13] Yu, M.C., Chen, X.N. *et al.* (1999). Introduction to the historical faults in Taiwan [A]. Proc. of 30th IGC(5) [C].Beijing: Geological Press.

[14] Chen Y.T., *et al.* (1999). Geodynamics environment in the Taiwan Straits and its both coast [J].*Crustal deformation and earthquake*, **19** (2), 38~45.(in Chinese)

[15] South China Sea Institute of Oceanology, Chinese Academy of Sciences (1989). Research of Petroleum Geology and Geophysics in West Taiwan[M]. Beijing: China Ocean Press, 110~113.(in Chinese)

[16] Kachishige Sato (1998). Plate and station movement deduced from the variation rate of GPS baseline length [J]. *Annual of Geodesy and Geophysics*, **44** (6): 25-32.

Palynological Evidence on Climate Changes in the East China Sea During Mid and Late Holocene

LI Zhen (李 珍)[1], Wang Yongji (王永吉)[1], Liu Zhenxia (刘振夏)[1], Lan Dongzhao (蓝东兆)[2]
1 *First Institute of Oceanography, SOA, Qingdao,* 266003
2 *Third Institute of Oceanography, SOA, Xiamen,* 361005

Abstract The pollen analysis of DGKS9617 core in the East China Sea (covering about the last 6800 years) shows five obvious pollen assemblages and seven sub-assemblages. Combined with the sediment and the result of diatom analysis, the climate changes are reconstructed during the Middle and Late Holocene. Corresponding to the pollen assemblages, the climate shifts just as follows: Assemblage Ⅰ-Warm and Dry Stage, Assemblage Ⅱ-Cool and Humid Stage, Assemblage Ⅲ-Hot and Dry Stage (the mean annual temperature is 2~3℃ higher than that today), Assemblage Ⅳ-Cool and Humid Stage, Assemblage Ⅴ-Warm and Dry Stage. The third stage is divided into three substages i.e. a slight colder and dry one, a slight warmer and humid one and a slight warmer and dry one. During the fifth stage, the climate becomes similar to that today with three warm substages and two cool substages.

Keywords palynology, climate changes, holocene, East China Sea

The East China Sea continental shelf receives large amounts of particulate and dissolved matters from Changjiang and Huanghe rivers, including a great deal of pollens and spores produced by terrestrial vegetation through water and wind. Thus, the pollen assemblages recorded in the sediments from the East China Sea can indicate the climate changes in detail.

With the cooperation between SOA, China and IFMEREM, France, several gravity cores are obtained from the scientific research vessel L'ATALANTE. One of the cores, DGKS9617, located in the East China Sea (31°18.58' N, 124°26.437' E) (Fig.1) with a depth of 57 meters under the water and a length of 8.5 meters, preserves abundant pollens, which provides favorable material for restoring the climate changes. The whole core is composed of silt and fine silt, and occasionally clayey sand. Frequent cross bedding indicates that strong tidal currents have occurred. Having not obtained the results of dating, we have estimated the ages by pollen assemblages, sediment characters and other reference in this paper.

1 Material and Methods

In order to obtain the detailed climate changes, close sampling is taken at the interval of 4cm from the core DGKS9617. Pollen extractions are made by standard methods in laboratory, samples being treated with hydrochloric acid (10%), sodium hydroxide (10%) to eliminate Ca2+ and organic material

* The International Cooperative Program is funded by NSFC (No: 49776292, 49576283) and the State Oceanic Administration (SOA) of China and IFREMER of France
* The subject is supported by Marine Science Youth Foundation of SOA (No.99502)

and heavy-medium separation is carried out many times with cadmium iodine (2.1~2.15g/cm^3) in turn. After preparation of thin sections, we identify the pollen under the light microscope and count more than 100 grains per sample. Several samples have not been counted because of rare pollens. The concentration of pollens is calculated by the extro-clavatum method. According to the results of identification and statistics, a pollen diagram is obtained which indicates the obvious climate shifts.

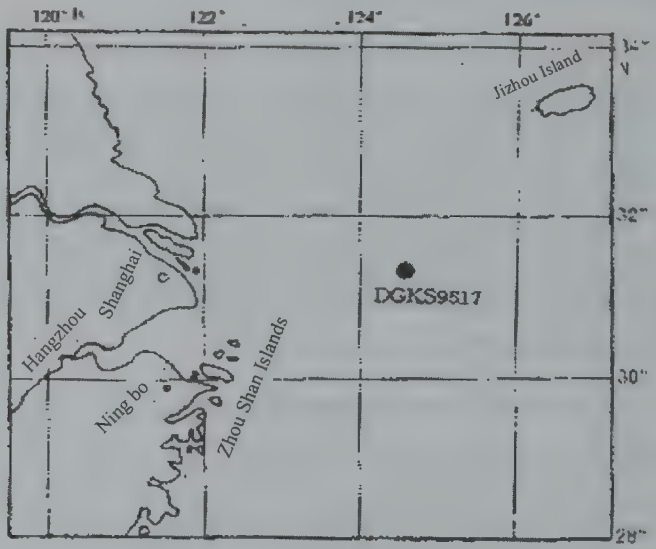

Fig.1 Location map of the core GK9617 in the East China Sea

2 Results

2.1 Pollen and spores

Pollen recorded in the core DGKS9617 is abundant and contains many types. We have identified pollens and spores classed to 25 families, 62 genera. Based on mother plants, the pollens on the whole are listed as follows:

1) Gymnosperm: *Ginkgo*, *Cycas*, *Pinus*, *Laris*, *Picea*, Cupressaceae, *Tsuga*, Taxodiaceae, Podocarpaceae.

2) Deciduous broad-leaf trees:*Q. acutissima*, *Ulmus*, *Beltula*, *Salix*, *Castanea*, *Tillia*, *Liquidambar*, Anacardiaceae, *Julans*. Acoraceae, *Carpnus*, *Ficus*, *Pistacia*, *Alnus*, *Pterocarya*.

3) Evergreen broad-leaf trees: *Q.glauca*, *Castanopsi*, *Eurya*, Meliaceae, *Ilex*, *Quisqualis*, *Figus*, *Helicia*, *Zelkora*, *Trachycarpus*, Rhiaophoraceae, Myristicaceae, Myrtaceae, *Liriodendron*, Carya, Rutaceae.

4) Shrub taxa: Ericaceae,*Corylus*, *Labiatae*, *Lonicera*, Euphorbiaceae, Balsuminaceae, *Elaeagnus*, *Camillia*, Apocynaceae, *Osmanthus*, Thymelaeaceae.

5) Herb taxa: Gramineae,*Urtica*, *Thalictrum*, Ranuncalaceae, Orchidaceae,*Cruciferae*, Onayraceae,

Umbelliferae, *Evonymus*, Chenopodiaceae, *Artemisia, Ephedra*, Cyperaceae, Potamogetonaceae, Iridaceae, *Alisma*, Liliaceae, Typhaceae, Sparganiaceae, *Polygonum, Hydrocharis*, *Myriophyllum*, *Lemna, Sagittaria.*

6) Fern taxa: *Pteridium, Polypodium, Adiantum, Hicriopteris, Osmunda, Pteris, Hymenophyllum, Cyathea, Lygodium, Ceratopteris,* Lycopodiaceae, *Plagiogyria, Cibotium,* Selagindle.

7) Others: *Cyclotella, Hystrichosphaera, Concentricytes* and some other types of diatom.

2.2 Pollen assemblages and the climate shifts restored

Six pollen assemblages are determined in the core, together with eleven subzones (Fig.2). The components of the pollen assdemblages are described as follows from bottom:

Assemblage Ⅰ (698~850cm):*Pteridium* – *Q. acutissima*–*Q. glauca*– *Polypodium* –Typhaceae. This assemblage is marked with high percentage of ferns, in which prominent components are *Pteridium*(the max value of 68.18%) and *Polypodium* (the max value of 10.78%). Ligneous plants consist of warm-temperate species such as *Quercous, Q.glauca, Castamolsos* and other subtropical trees like *Eurya, Ilex, Quisualis,* Euphorbiaceae, *Labiatae* and so on, while the main components of Typhaceace (mean=5%) and *Alisma* are a prevailing group in the herbs. The high percentage of warm elements and plentiful aquatics indicates the warmer and humid climate.

Assemblage Ⅱ(602~698cm): *Pteridium* –*Q.acutissima* –*Q.glauca* –Chenopodiaceae– *Polypodium. Pteridium* is still the main component and up to 30.36%, and next is *P alypodium*(6.32%). *Hicriopteris, Pteris,* Hymenophyllum and *Cyathea,* which belong to tropical or subtropical types, occur occasionally. Ligneous plants are similar to the Assemblage Ⅰ, but Typhaceae reduces quickly and arid herbaceous elements such as Chenopodiaceae (6.54%) and *Artemisia* (5%) increase, which shows the warm and arid climate with the mean annual temperature being 2–3℃ higher than that today as in Assemblage Ⅰ.

Assemblage Ⅲ (374~602cm): the pollen assemblages in general point to the cooler and more arid condition than before as shown by the predominance of *Pteridium, Quercous, Polypodium*, *Pinus and Artemisia* while *Q.glauca* is decreasing. Because of the frequent shift, three subzones are further divided.

Subzone Ⅲa (501~602cm):*Pteridium* – *Q.acutissima*– *Artemisia* – Chenopodiaceae. *Q.glauca* gradually reduces to 4.55% and Chenopodiaceae increases with a certain castanopsis percentage of 1.66%, indicating the cool and arid condition with the mean annual temperature about 2℃ lower than that in Assemblages Ⅰ and Ⅱ, but similar to that today.

Subzone Ⅲb (427~501cm):*Pteridium* – *Q.acutissima* – Typhaceae– *Q.glauca* –*Polypodium.* The evergreen tree *Q.glauca* (6.14%) increases again, with the *Castanopsis* percentage of 2.41%, in herbs, *Artemisia* decreases and Typhaceae becomes the main component, showing the slight warmer and humid climate, being 1~2℃ higher than that today.

Subzone Ⅲc (374~427cm):*Ptedium* – *Q.acutissima* –*Artemisia* –Chenopodiaceae. This subzone obviously indicates the slight cool and arid condition but the temperature is still 1℃ higher than that today.

Assemblage Ⅳ(192~374cm): Pollen concentration rises sharply to the maximum in the whole core, with the character of the rising ligneous plants and the reducing ferns. According to the changes of components, three subzones are divided, indicating a cold and arid climate in general.

Subzone Ⅳa (286~374cm): *Q. acutissima*–*Artemisia*–Chenopodiaceae–*Pteridium* –*Polypodium.* Ligneous plants gradually increase from 13.77% to 68.42%, while ferns reduce from 73.19% to 17.29%. This subzone is marked with the prevailing *Quercous* (mean = 14.19%) and *Castanopsis* disappearing.

The increasing of Cupressaceae, *Ulmus* and *Betula*, which is fit in the cooler condition, shows a lower temperature than before and abundant *Acremisia* as well as Chenopodiaceae indicate an arid environment.

Subzone Ⅳb (237~286cm): *Q.acutissima* -*Q.glauca* -*Artemisa* -Chenopodiaceae -*Pterium*. Ligneous plants have been steady with an average of 56.68%, in which *Q.glauca* rises up to the maxium value (mean = 18.75%) in the subzone and *Castanopsis* appears again. The high percentages of *Artemisa* , Chenopodiaceae and Compositae in association with low values of humid herbaceous elements show a slight warm and arid climate.

Subzone Ⅳc (192~237cm):*Q. acutissima* - *Q. glauca* Typhaceae- Gramineae *Polypodium.* The broadleaf tree of temperate *Quercous* (17.3%) and the evergreen *Q. glauca* (15%) are still the prominent components similar to the Subzone Ⅳb. But hydrophyte (nearly 22%) obviously increases while the steppe elements (Chenopodiaceae, *Artemisia*) are decreasing. This subzone clearly shows a slight warm and humid climatic condition.

Assemblage Ⅴ (116~192cm):*Q.acutissima* - *Polypodium* - Typhaceae Gramineae- *Q.glauca* -*Pinus*. A clearly different pattern is represented by the low percentage of *Q.glauca* and disappearance of *Castamolsos*, which reflects a cold climate, corresponding to the highest content of *Pinus*. Pollen taxa from the artificially raised herbaceous plant or Gramineae increase in contrast to those steppe elements. Thus, it shows a cool and arid climatic condition, which may be appropriate for agriculture.

Assemblage Ⅵ(0~116cm): The assemblage's components change very quickly with a big margin at small intervals. So, it is necessary to divide it further into five subzones.

Subzone Ⅵa (89~116cm):*Q.acutissima* - Gramineae *Q.glauca* -*Artemisia*. Deciduous *Quercus* and evergreen *Q.gauca* abruptly rising in number in association with *Castamosis* (2~3%) occurring and Cupressaceae decreasing reflect the mixed deciduous and evergreen forest which indicates a warm climate in this area. High percentage of *Artemisia* points to the arid condition.

Subzone Ⅵb (70~89cm): Gramineae-Typhaceae - *Hystrichosphaera.* The highest percentage of Gramineae, especially that with the grain size more than 40 μ m , reflects a fit condition for agriculture. In this stage, ligneous plants decrease while the ferns, Hydrophyte and freshwater- Hystrichosphaera all increase, indicating a slight cooling and humid condition, in which agriculture is well developed.

Subzone Ⅵc (47~70cm):*Q.acutissima* -Gramineae -*Q.glauca* -Typhaceae. This stage, similar to the Subzone Ⅵa, indicates a warm climate, except for the humid condition that is shown by the high percentage of humid herbaceous elements and the low percentage of steppe elements.

Subzone Ⅵd (11~47cm):*Pteridium* - Gramineae - Cupressaceae - Chenopodiaceae. *Pteridium,* which is the main component of ferns, abruptly increases, in contrast to the ligneous plant decreasing with high percentage of Cupressaceae (6.37%) as well as other low-temperature taxa (*Ulmus, Betula*). In addition, Chenopodiaceae rises a little, and thus the subzone reflects a cold and arid condition with the mean annual temperature 1℃ lower than today.

Subzone Ⅵe: *Q.acutissima* -*Q.glauca* Gramineae - *Pteridium.* As shown in the upper part of the diagram, *Q.acutissima* (12.53%) and *Q.glauca* (8.5%), above 11cm, are the main components of the ligneous plants, in association with the lower percentages of Cupressaceae, *Ulmus* and *Betula*, indicating that the climate change into the warm and arid condition again, which may be similar to that today.

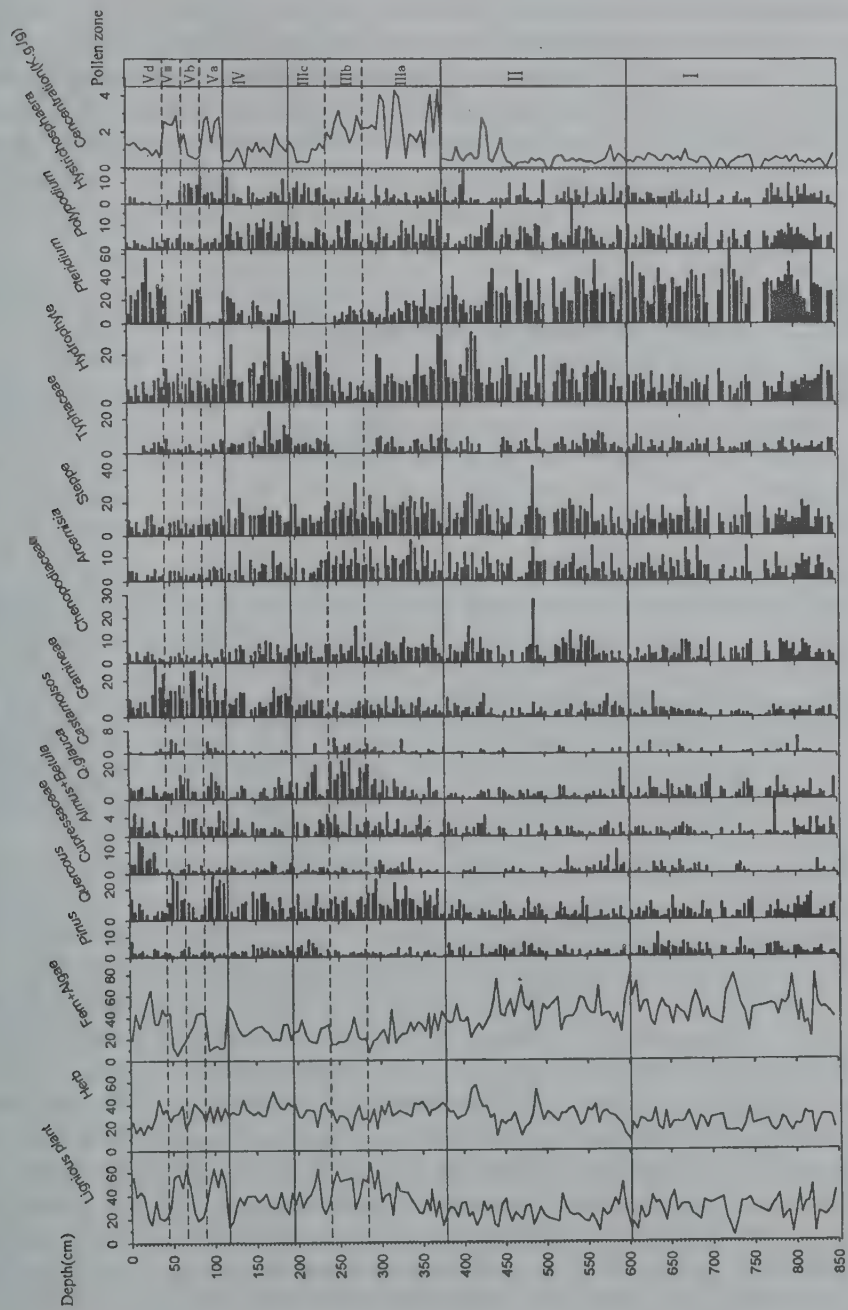

Fig. 2 Pollen diagram showing major floral components of the sediment in the East China Sea

2.3 Pollen Concentration

Pollen concentration is defined as the total pollens per volume (grains/cm^3) or weight (grains/g). Closely linked to the mother plants, the changes of pollen concentration can also be regarded as one of the evidences on climate shifts. To avoid too large errors that may be caused in the laboratory treatment and the statistics due to different numbers of pollens, we have chosen the extro-clavatum method to calculate the pollen concentration using the following equation:

$$X = \frac{N^* n}{N' * G}$$

X–pollen concentration (grains/g)

N–the total extra clavatum added into the sample

N'–the total extra clavatum determined under the microscope

G–the weight of sample for analysis

Based on the corrected values of mother plants, the curve, which expresses the pollen concentration changes with the depth of the sample, is attached to the right panel of the pollen diagram (Fig.2).

3 Discussion

3.1 Determining the stratigraphical time

Frequent cross bedding indicates strong tidal currents. On the basis of the tectonic character and sedimentation and the pollen assemblages of this area, especially in the pollen zones, deciduous or evergreen broadleaf trees are the main components in the whole core with abundant *Q.glauca* and *Castamosis* and low content of coniferous elements. Wang Kaifa *et al.* found that a great deal of the evergreen *Q.glauca* and*Castamosis* appeared at the beginning of Holocene and bloomed in mid-Holocene in Changjiang Delta. So, we can conclude that the core is the sediment during the mid-late Holocene, which is also reflected by the fact that the diatoms preserved are all of the type in the modern surface sediment.

In the pollen diagram, we can find the obvious change at the level of 374cm where the pollen concentration abruptly rises and the ligneous plant becomes the prominent taxon, in contrast to ferns. The phenomenon may be caused by sea regression. Because in marine strata, the farther offshore, the sediment area is the lower the pollen concentration is and the higher the spore content becomes. E.B. Kronorwa found that spores were carried farther and suggested that spores were easy to be transported by water than by others because of the stronger floating ability when she investigated the pollens preserved in the bottom of North Pacific Ocean. In the same way, pollen analysis on the marine sediment near the west of Eran Island in Middle Pacific Ocean shows that pollen concentration decreases with the increasing distance away from the coast, while the spore content is rising. Wang Kaifa and Wang Yongji obtained the similar conclusion when they studied the pollen in the surface sediment in the Yellow Sea and East China Sea. Being in the shallow sea environment and far away from the coastal line during the Holocene, pollen assemblage and distribution are strongly affected by sediment rules of pollen carried in the area, which differs from the coastal area where the pollen resource distance induced by sea level changes is the main factor. Thus, we are apt to determine that this level is the boundary between the mid-Holocene and the late-Holocene.

Consisting of *Q.glauca*, *Castamosis*, *Eurya*, *Ilex*, *Quisqualis*, *Figus*, *Helicia*, *Zelkora*, *Trachycarpus*,

Myrtaceae, *Liriodendron*, Carya and a certain amount of deciduous broadleaf trees, the pollen zones I and II indicate the character of mixed deciduous and evergreen broadleaf forest prevailed by evergreen trees. In the pollen zone III, the warm genus and family trees obviously decreasing and coniferous trees and the steppe elements increasing shows the cooler and drier condition than before, but the mean annual temperature is still 1~2℃ higher than that today, corresponding to the Sub-Boreal Period. In all, we can estimate that the pollen zones I and II are related with the Atlantic Period, while the pollen zone III reflects the Sub-Boreal Phase.

3.2 Reconstruction of paleoclimate and paleoenvironment

As for studying climate changes during Holocene, most scientists regard Optimum-Atlantic Period (based on A.Blytt) or Mid-Holocene (based on three-period dividing) as a whole stage to study and this stage, when vegetation on the coastal land was most luxuriant, the sea level was the highest and the coastal line extended the farthest, played an important role as an indicating period in Holocene (Meng Guanglan *et al*, 1984; Wang Kaifa *et al*, 1989). However, with more and more high-resolution study on climate changes, it is found that the Mid-Holocene or Atlantic Period is not always in the warm condition, in fact, many shifts of cool-warm or dry-wet conditions occurred. Yang Huairen *et al* (1984) found that during the Atlantic Period, the climate changed within a 4~5℃ range of temperature in East China and the temperature as well as the sea-level changes were keeping lower than that today for a long time. Han Huiyou *et al.* (2000) suggested that a transformation period existed when warm-cool and wet-dry conditions shifted within a relatively wide range according to the study of pollens and plant fossils on Baohuashan Hill in Jurong County of Jiangsu Province.

The study in this paper suggests that the climate was generally warm-humid during the mid-Holocene when vegetation bloomed with the main components of warm species such as *Q.glauca*, *Cast amosis* and much more species appearing in the mid-subtropical zone and south-subtropical zone. With the persistently warming climate, dry condition became the character of the coastal area in Southeast China and the warm-wet climate appeared inland with 2~3 ℃ higher than today and the coast-line once extended to the region of Zhenjiang as Meng Guanglan reported (1989). During the Sub-Boreal Period, the climate was temperate-cool with three obvious shifts. The temperature during the substage IIIa was 2℃ lower than Stage II and the arid condition was indicated by *Q.glauca* gradually reducing and Chenopodiaceae increasing, compared with the growth environment of the similar vegetation. Subzone IIIb with evergreen tree of *Q. glauca* increasing again and *Castamopsis* occurring shows a slight warm and humid climate. The third substage is indicated by the subzone IIIc with the character of a slight cool and arid condition.

Tab.1 Paleovegetation and paleoclimate indicated by pollen analysis for DGKS9617 core

Age (aBP)	Pollen assemblages		Vegetation types	Climate stages		Mean annual temperature
80	VI	VIe	Mixed deciduous and evergreen broad-leaf forest	War man darid	Warm and arid	Simila to today with two cool substages nearly 1℃ lower than today
376		VId	Mixed evergreen and deciduous broad-leaf forest		Cool and arid	
562		VIc	Mixed deciduous and evergreen broad-leaf forest-Meadow		Warm and humid	
720		VIb	Meadow and swamp-Agricultural plants		Cool and humid	
933		VIa	Mixed deciduous and evergreen broad-leaf forest-Meadow		Warm and arid	
1530	V		Mixed coniferous and evergreen broad-leaf forest-agricultural plants	Cool and humid		1 ~ 2 ℃ lower than today
1900	IV	IVc	Mixed coniferous and evergreen broad-leaf forest-Meadow	Cold and arid	Warm and humid	Similar to today
2300		IVb			Temperate and arid	
3000		IVa			Cool and arid	1 ~ 2 ℃ lower than today
3400	III	IIIc	Mixed evergreen and deciduous broad-leaf forest-Meadow	Warm and humid	Temperate and arid	Nearly 1℃ higher than today
4000		IIIb			Warm and humid	1 ~ 2 ℃ higher than today
4800		IIIa			Temperate and arid	Similar to today
5600	II		Mixed deciduous and evergreen broad-leaf forest, prevailed by evergreen trees-Meadow	Warm-Hot and arid		2 ~ 3 ℃ higher than today
6800	I		Mixed deciduous and evergreen broad-leaf forest, prevailed by evergreen trees-Swamp	Warm-Hot and humid		

During the late-Holocene, the sea level had retreated to the site similar to that today. Pollen transportation course was shortened much and the pollens of ligneous plant are easy to reach the site and settle down, which may be the main reason for the maximum pollen concentration. The variance of pollens increased in the sediment. The northern subtropical vegetation on coastal land reflected by the general pollen assemblages indicated the temperate-cool and arid climate. During this time, with the decline of the sea level and extensive development of lakes, swamp and rivers are developing, the humid herbs such as *Alisma*, Typhaceae, Sparganiaceae, *Polygonum, Lemna* and Iridaceae were growing well. Three substages are determined, i.e. a colder and arid climate, a slight warm and arid climate and a slight warm and humid climate, corresponding to IVa, IVb and IVc respectively. Substage IVa is one of the coldest stages in Holocene, when agriculture developed and ancestors cultivated on the plain (Li Zhen

et al., 1996). It is also called Neo-ice age lasting for a short time. Substage IVb is a slight warm and arid climate, then the climate changed into IVc with the character of warm and humid condition associated with the warm and humid period of 1900~1530aB.P. in Changjiang Delta reported by Zhang Tianling (1982). Wang Kaifa (1989) has suggested four periods of vegetation and climate shifts of Shanghai area during the late-Holocene on the basis of pollen analysis. They are a warm and humid climate with the mean annual temperature higher than today, a cooler climate than today, a warmer climate than today and a colder climate again, respectively, corresponding to 2900~1800aB.P., 1800~1400aB.P., 1400~850aB.P. and 850~550aB. P.

Since the tenth century, the human activities and the stronger ability to rebuild nature have greatly affected the vegetation development and climate changes. The climate has frequently changed on the basis of warm and arid condition similar to today in general. Five substages can be identified, which are three warm substages and two cold periods connected with the pollen subzones of VIa, Vic, VIe, VIb and VId respectively. The last cold substage may be associated with the little cold phase in China.

4 Conclusion

1) Our data show two possible boundary lines, one being the level of 374cm between mid-Holocene and late Holocene, the other being the level of 602cm between the Atlantic Period and the Sub-Boreal Period during mid-Holocene.

2) In the Atlantic Period, indicated by the pollen assemblages I and II, the sea level had risen to the highest level and the mean annual temperature was also 2~3 ℃ higher than that today. In the Sub-Boreal Period, shown by the pollen assemblage III, the coastline began to retreat and the temperature became lower but it was still 1~2 ℃ higher than that today. During the sub-Atlantic Period, corresponding to the late Holocene, the coastline retreated to the Shanghai area just as today and the temperature was similar to that today in general, except for the two obvious slight cold phases.

3) Rhizophoraceae, a special plant along the tropical coast, which growth demands a strict ecological environment, and other tropical plants such as *Quisqualis, Trachycarpus* appear in the core now and then, which may be consistent with the Kuroshio Current transporting action reported by Zhang Yulan and Wang Kaifa.

In this area, due to the complex factors such as hydrodynamic action, tidal current, bioturbation, even human activity and so on, it is necessary to further study other index to solve the knotty problem and correct the results from pollen analysis.

Acknowledgements

This work has been completed with the cooperation of science groups on the scientific research vessel in 1996. Here, the authors are thankful to all the institutions and people who have supported this work, especially to Xu Xiaowei for part of the figures and Wang Xiangqin for the convenience provided by her in laboratory treatment.

Reference

[1] Yang Zigeng and Lin Maohe (1996) Quaternary stratigraphy in China and its international correlation. *Geological Publishing House*, Beijing, China. (in Chinese)

[2] Wang Kaifa *et al.* (1989) Vegetation and climate changes in the west of Shanghai since 3.000aB.P from pollen assemblages. *History and Geology*, **6**. (in Chinese)

[3] Meng Guanglan *et al.* (1989) Late Quaternary sporopollen assemblages and their geological significance in the Changjiang River mouth area of the East China Sea. *Marine Geology & Quaternary Geology*., **9** (2): P13-25. (in Chinese)

[4] Zhang Tianlin (1982) The primary study on the climate history of Changjiang Delta,*Trasaction of Huadong Normal University*, (4).

[5] Jian Zimin *et al.* (1996)The cooling event in West Pacific during late Holocene.*Science in China (Compile D)*. **26** (5). (in Chinese)

[6] Anne-Marie Lʃzine *et al.* (1997) Ehanced anticyclonic circulation in the eastern North Atlantic during cold intervals of the last deglaciation inferred from deep-sea pollen records. *Geology*. **25** (2): P119-122.

[7] Jol Guiot. (1989) Late Quaternary climatic change in France estimated from multivariate polìen time series. *Quaternary Research*, 28, 100-118.

[8] Brian Huntley and I.Colin Prentice (1988) July temperatures in Europe from pollen data, 6000 years before present. *Science*, **241**: 687-690.

[9] Joel Guiot *et al.* (1993) Reconstruction of Holocene precipitation patterns in Europe using pollen and lake-level data.*Quaternary Research*. **40**: 139-149.

[10] Xue-Dong Xu (1999) Motoyoshi Oda. Surface-water evolution of the eastern East China Sea during the last 36 000 years. *Marine Geology*, **156**: 285-304.

[11] Prof.Kenneth O.Emery Commemorative International Workshop (1999) Land Sea link in Asia. Publised in Japan.

Enhancement Effects of Three Rare Earth Elements on the Growth of Chaetoceros Mulleri*

Qu Keming (曲克明), Xin Fuyan (辛福言)
Yellow Sea Fisheries Research Institute, CAFS, Qingdao 266071

Abstract Enhancement effects of rare earth elements on the growth of *Chaetoceros mulleri* is studied in this paper. The results show that all of the light, middle and heavy rare earth elements have similar enhancement effect on the growth of *Chaetoceros mulleri*, with the beneficial concentrations of La, Gd and Yb being 7.28~87.40 μ mol/L, 6.36~57.23 μ mol/L and 5.78~17.34 μ mol/L. The optimum concentrations of La, Gd and Yb are 7.28 ~50.98 μ mol/L, 31.80~44.52 μ m ol/L and 5.78~17.34 μ mol/L, respectively. When the concentrations of La , Gd and Yb are 7.28~87.40 μ mol/L, 6.36~57.23 μ mol/L and 5.78~17.34 μ mol/L, the concentrations of chlorophyll have increased by 9.3~47.0%, 33.4~44.3%, and 36.5~40.3%, respectively as compared with the control group. The mechanism of enhancement of rare earth elements on the growth of *Chaetoceros mulleri* is also discussed in this paper.

Keywords rare earth element, *Chaetoceros mulleri*, enhancement

Introduction

Rare earth has special living action on organisms, so it is extensively applied in agriculture, forestry, livestock husbandry, freshwater aquaculture, herbage, and medicine (Xiong Binghui, 1994). Rare earth can significantly accelerate photosynthesis of higher plants and improve the quality of crops. Studies on the effects of rare earth on algae culture (Chu Zhongxi, 1994) and on freshwater fish farming (Song Zhengdong, 1994) indicate that the trace element of rare earth could enhance the growth of living beings in fresh water and improve their quality. But the concentration of rare earth in natural seawater is only 0.01 μg/L, which is too low to enhance growth of marine organisms.

Our previous studies were carried out on the effects of mixed rare earth on egg hatching and naulius metamorphosis of *Penaeus Chinensis* (Yuan Youxian, 1999), the effects of lanthanum on egg hatching and nauplius metamorphosis of *Penaeus Chinensis* (Xin Fuyan, 1997), the enhancement of mixed rare earth on the growth of *Penaeus Chinensis* (Yuan Youxian, 1997), and the effects of mixed rare earth on *Chaetoceros mulleri* (Qu Keming, 1997) and on *Isochrysis galbana* (Qu Keming, 1998).

The results of these experiments show that rare earth could significantly promote the growth of *Chaetoceros mulleri* and *Isochrysis galbana*. In order to understand the mechanism of effects of rare earth on marine organism, we have studied the effects of the light, middle and heavy rare earth elements on the growth and chlorophyll contents of *Chaetoceros mulleri* and their comparison .

* Supported by National Natural Science Fund of China (No: 39370548)

1 Experimental materials and methods

1.1 Experimental materials and reagent

The alga (*Chaetoceros mulleri*) has been collected from the Yellow Sea Fisheries Research Institute. The seawater for the trial is gotten from offshore in Maidao Island, Qingdao. The salinity and pH of the seawater are 30~31 and 8.1, respectively. The seawater is precipitated and filtered through sand, then stored in a polyethene plastic bucket. All reagents used in the trails are analytical reagents. The lanthanum, gadolinium, and ytterbium stock solutions of 1 000mg /L are prepared from the diluted hydrochloric acid and distilled water.

1.2 Experimental methods

Seawater and algae are put into 250ml flasks, and then nutrients and rare earth elements are put into these flasks. Each trial has 5 replicates and one control. The experimental conditions are as follow:

Test volume: 150ml in 250ml flask

Initial algae cell concentrations: $40\sim50\times10^4$cell/L

Nutrients concentrations added and the ratio: N/P/Fe = 30/2/ 0.5mg/L

Temperature: 25 ± 1℃

Lighting: 4 fluorescent lamp of 400W in parallel, 4000 Lux, lighting/dark =13/11

Shaking: 3~4 times per day, and exchange their positions randomly

Samples are collected every day and the absorbencies are determined by spectrophotometer (Shimadzu, Japan) with 1cm cell at the 550nm wave length. The algae cell concentrations are adjusted by using the working curve. Effects of rare earth on the growth of algae are assessed by statistics methods. The contents of chlorophyll are determined by using the methods provided in the Specifications of Oceanographic Survey, State Oceanic Administration of China, 1991.

2 Results and discussion

2.1 Effects of rare earth on the growth of *Chaetoceros mulleri*

2.1.1 Effects of lanthanum on the growth of *Chaetoceros mulleri*

The results (Fig. 1) of effects of lanthanum on *Chaetoceros mulleri* show that the algal cell concentrations of trails with 7.2887.40~μmol/L La were significantly ($P<0.05$) higher than that of the control group from the 2nd day. The algal concentrations of trials with 7.28~50.98 μmol/L La are significantly ($P<0.05$) higher than that of the control group and other trials at the 6th day, while no significant differences among these trials with 7.28~50.98 μmol/L La are found. The algal concentrations of the trials with 7.28~50.98 μmol/L La increase by 31.6~35.5%, as compared with the control group. Because the seawater is alkaline, La^{3+} will hydrolyze and the seawater will become turbid when the concentrations of La is higher than 87.40 μmol/L.

2.1.2 Effects of gadolinium on the growth of *Chaetoceros mulleri*

Chaetoceros mulleri cell concentrations of trials with 6.36~57.23 μ mol/L Ga and that of trials with 6.36~44.52 μmol/L Ga are significantly ($P<0.05$) higher than that of the control group from the 4th day

and from the 2nd day respectively (Fig. 2). The algal concentrations of trials with 19.08~44.52 μmol/L Ga are significantly (P<0.05) higher than that of the control group and other trials, while no significant differences among these trials are found. The algal concentrations of the trials with 7.28~50.98 μmol/L Ga increase by 17.7~19.1%, as compared with the control group.

2.1.3 Effects of ytterbium on the growth of *Chaetoceros mulleri*

Chaetoceros mulleri cell concentrations of trials with 5.78~17.31 μ mol/L Yb are significantly (P< 0.05) higher than that of the control group and other trials from the 3rd day (Fig. 3). There is no significant difference between trials with 5.78~17.31 μ mol/L Yb. The algal concentrations of the trials with 5.78~17.34 μ mol/L Yb increase by 19.3~22.8%, as compared with the control group.

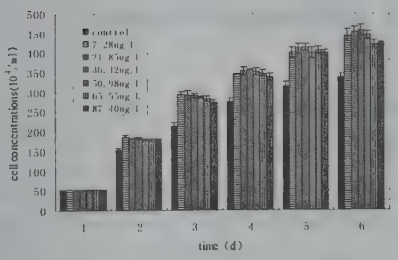

Fig. 1 Effects of La on the growth of *Chaetoceros mulleri*

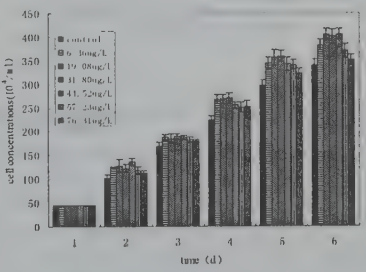

Fig. 2 Effects of Gd on the growth of *Chaetoceros mulleri*

2.1.4 Effects of light, middle and heavy rare earth elements on the growth of *Chaetoceros mulleri*

To compare the effects of light, middle and heavy rare earthelements on the growth of *Chaetoceros mulleri*, the optimum concentrations of La (36.42 μ mol/L), Ga (31.8 μ mol/L) and Yb (17.34 μ mol/L) are selected in the tests. The results (Fig. 4) show that the cell concentrations of the three trials are significantly (P<0.05) higher than that of the control group, but there are no significant differences among the three trials. It indicates that the three rare earth elements have similar positive effects on the growth of *Chaetoceros mulleri.* The beneficial concentrations are different among the three elements, so are the optimum concentrations. The beneficial concentrations of La , Ga and Yb are 7.28~87.40 μ mol/L, 6.36~57.23 μ mol/L and 5.78~17.34 μ mol/L respectively; the optimum concentrations of La, Ga and Yb, 7.28~50.98 μ mol/L, 19.08~44.52 μ mol/L and 5.78~17.34 μ mol/L respectively. These results are in keeping with those reported by Qu (1997), in whose study it is suggested that the mixed rare earth could enhance the growth of *Chaetoceros mullei*, and the optimum concentrations have been 12.04~ 48.17 μ mol /L.

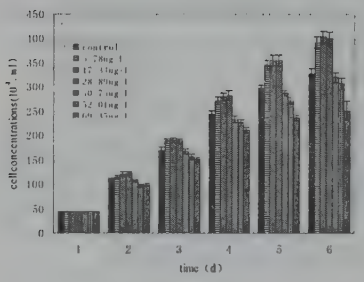

Fig. 3 Effects of Yb on the growth of *Chaetoceros mulleri*

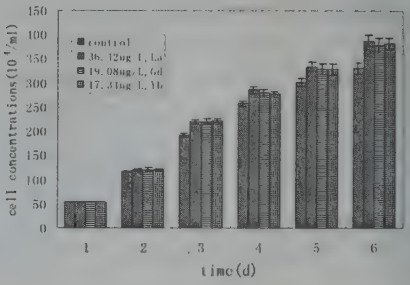

Fig. 4 Effects of 3 kinds of rare earth on the growth of *Chaetoceros mulleri*

2.2 Effects of rare earth on chlorophyll contents of *Chaetoceros mulleri*

2.2.1 Effects of lanthanum on chlorophyll contents of *Chaetoceros mulleri*

The results of effects of lanthanum on chlorophyll contents of *Chaetoceros mulleri* are given in Table 1. The chlorophyll contents of *Chaetoceros mulleri* of trials with 7.28~87.40 μ mol/L La are higher than that of the control group from the 3rd day, and increase by 7.28~87.40% at the 6th day as compared with the control group. These results are similar to those of the La test on growth of *Chaetoceros mulleri*.

Tab. 1 Results of effects of La on the chlorophyll synthesis of *Chaetoceros mulleri*

$[La^{3+}]$ (μ mol/L)	Contents of chlorophyll (μ g/L)					
	1st day	2nd day	3rd day	4th day	5th day	6th day
0	140.5	288.9	651.6	847.2	950.5	1 110.6
7.28	140.5	269.3	693.7	940.2	1 193.5	1 420.4
21.85	140.5	302.7	722.0	1 012.8	1 302.6	1 541.4
36.42	140.5	317.4	732.7	1 033.9	1 347.8	1 632.9
50.98	140.5	320.5	729.2	1 073.1	1 340.6	1 520.3
65.55	140.5	305.6	740.1	1 070.1	1 309.9	1 521.6
87.40	140.5	300.7	702.5	927.8	1 001.5	1 213.7

2.2.2 Effects of gadolinium on chlorophyll contents of *Chaetoceros mulleri*

The results of effects of gadolinium on chlorophyll contents of *Chaetoceros mulleri* are given in Table 2. The chlorophyll contents of *Chaetoceros mulleri* of trials with 6.36~57.23 μ mol/L Ga are higher than that of the control group from the 3rd day, and increase by 33.4~ 43.3% at 6th day as compared with the control group. These results are in keeping with those of Ga test on growth of *Chaetoceros mulleri.*

Tab. 2 Results of effects of Gd on the chlorophyll synthesis of *Chaetoceros mulleri*

[Ga^{3+}]	Contents of chlorophyll (μ mol/L)					
(μ mol/L)	1st day	2nd day	3rd day	4th day	5th day	6th day
0	140.5	288.9	651.6	847.2	950.5	1 110.6
6.36	140.5	280.1	657.8	926.1	1 213.7	1 482.0
19.08	140.5	299.3	688.9	933.7	1 327.8	1 522.6
31.80	140.5	305.6	702.3	962.6	1 388.6	1 582.7
44.52	140.5	301.6	721.5	987.3	1 385.7	1 589.8
57.23	140.5	292.5	720.1	957.8	1 341.6	1 531.6
76.31	140.5	299.4	667.8	867.7	960.4	1 109.5

2.2.3 Effects of ytterbium on chlorophyll contents of *Chaetoceros mulleri*

The results of effects of ytterbium on chlorophyll contents of *Chaetoceros mulleri* are given in Table 3. The chlorophyll contents of *Chaetoceros mulleri* of trials with 5.78~17.34 μ mol/L Yb are higher than that of the control group and other trials from the 3rd day, and incrase by 36.5~40.3% at the 6th day as compared with the control group. These results are similar to those of Yb test on growth of *Chaetoceros mulleri.*

Tab. 3 Results of effects of Yb on the chlorophyll synthesis of *Chaetoceros mulleri*

[Yb^{3+}]	Contents of chlorophyll (μ g/L)					
(μ mol/L)	1st day	2nd day	3rd day	4th day	5th day	6th day
0	140.5	288.9	651.6	847.2	950.5	1 110.6
5.78	140.5	300.1	682.1	926.9	1 194.6	1 394.8
17.34	140.5	307.3	693.5	942.3	1 288.3	1 592.6
28.89	140.5	290.2	647.7	836.5	949.4	1 000.8
40.45	140.5	280.4	648.3	830.4	933.1	987.4
52.01	140.5	273.5	607.4	786.7	901.5	980.1
69.35	140.5	270.6	600.6	700.1	900.4	961.3

Owing to the retractile characteristics of lanthanide, the ion radii of lanthanide decrease gradually with the increase of atomic number. The ion radii of lanthanum, gadolinium and ytterbium are 0.116, 0.105 and 0.0985nm respectively, when their ligancies are 8 (Xu Guangxian, 1995a). Some enzymes may be activated and/or prohibited by rare earth elements. The interactions between enzymes and rare earth are relative to both the concentrations and the radii of these elements (Xu Guangxian, 1995b). The catalyses may be obviously quickened at proper concentrations and suitable ion radii of rare earth elements. The mechanisms of the enhancement of rare earth on algal growth may be explained as follows: Rare earth elements could combine with some enzymes, as a result of which the enzymes are activated, and then the photosynthesis of algae are promoted. Further studies, however, are needed on which kind of enzymes could combine with rare earth elements.

3 Conclusion

All of the light, middle and heavy rare earth elements could significantly accelerate the growth of *Chaetoceros muller*. The degrees of promotion are similar, but the concentrations of rare earth elements are quite different. It is suggested that rare earth elements may combine with some enzymes, and activate the enzymes, resulting in the promotion of the photosynthesis of algae. As algal accelerants, the cheap mixed rare earth could be very promising.

Reference

[1] Xiong B H (1994) Applied study on biological function compound of rare earth. *Journal of Rare Earth*, **12** (4): 358-365.

[2] Chu Z X, Mu M H, Zhang H P, *et.al.* (1994) Effects of cerous chloride on photosynthesis, pigment and protein syntheses of *spirulina. Journal of Rare Earth*, **12** (4): 344-347.

[3] Song Z D, Jiang Z Y, Liu H T, *et.al.* (1992) Effects of rare earth elements on growth and metabolism of carp.*R are Earth*, 13: 60-62,70.

[4] Yuan Y X, Qu K M, Xin F Y (1999) Effects of rare earth on egg hatching and nauplius metamorphosis of *Penaeus Chinensis. Journal of Fishery Science of China*, **20** (1): 52-56.

[5] Xin F Y, Yuan Y X, Qu K M (1997) Effects of lanthanum on egg hatching and nauplius metamorphosis of *Penaeus Chinensis. Journal of Rare Earth*, **15** (1): 289-292.

[6] Qu K M, Yuan Y X, Xin F Y(1997) Effects of rare earth on growth of *Chaetoceros mulleri. Acta oceanologica sinica*, **19** (2): 124-127.

[7] Qu K M, Yuan Y X, Xin F Y (1998) Effects of rare earth on growth of*Isochrysis galbana. Oceanologia et limnologia sinica.* **29** (5): 552-557.

[8] State Oceanic Administration of China (1991) *Specifications of Oceanographic Survey*, China Ocean Press, Beijing: 688-691.

[9] Xu G X (1995a) *Rare earth* (Volume I). Metallurgical Industry Press , Beijing: 29-33.

[10] Xu G X (1995b) *Rare earth* (Volume II). Metallurgical Industry Press. Beijing: 471-480.

[11] Elderfield H, Greaves M J (1982) The rare earth elements in seawater. *Nature*, 296: 214-219.

[12] Yuan Y X, Qu K M, Xin F Y and Li J (1997) Enhancement of rare earth on growth of *Penaeus chinensis.*

Supplement and Consumption of Dissolved Oxygen and Their Seasonal Variations in Shrimp Pond

Sun Yao(孙 耀)[1], Zhang Shufang (张淑芳)[2], Chen Jufa(陈聚法)[1], Song Yunli[1] (宋云利)
1 *Yellow Sea Fisheries Research Institute, Chinese Academy of Fisheries Sciences, Qingdao* 266071
2 *Qingdao Ocean University* 266003

Abstract On the basis of the research of DO budget or kinetics in shrimp pond, the main influence process of DO and its seasonal variations are quantitatively described through redividing the budget process and modifying the quantitative method of the process. The percentages of oxygen demand of various processes in the total oxygen demand are different in shrimp cultivation seasons. It is showed that the dissolved oxygen demand of mini-organisms is the major affected factor of DO in this environment and approximately accounts for 64.1~74.1% of the total oxygen demand. In the early period of shrimp culture, the dissolved oxygen demand of allotrophic bacteria degrading organic matters is much lower than that of phytoplankton respiration. But in the midterm and later period, it is about 50% of the total oxygen demand because of the higher water temperature and more serious self-pollution. The dissolved oxygen demand of sediment is lower and just 19.1~28.8%, while the percentage of shrimp oxygen demand is lower. The effect of phytoplankton on DO in shrimp culturing water has dualism. One is the oxygen producing process of photosynthesis and the other is the oxygen consumption process of respiration. It is estimated that the dissolved oxygen demand of phytoplankton respiration is approximately one-fifth of the oxygen produced by photosynthesis under normal illumination conditions. The dissolved oxygen demand of allotrophic bacteria degrading organic matters and the total oxygen demand of sediment increase 4 times and 1.7 times respectively from the early period to the midterm and later period. Obviously, the DO of culturing water can be also greatly improved by controlling the self-pollution of organic matters during shrimp culture.

Keywords DO, consumption, supplement, consumption, shrimp pond

Introduction

Dissolving oxygen (DO) is one of the important environmental factors in shrimp pond cultivation waters, which directly or indirectly affects the growth of culturing organisms. In China, shrimp cultivation mainly adopts semi-intensively managed method without aeration. It is characterized by limited water exchange and feed throwing. The frequent incidence of shrimp diseases in the last few years has made Chinese shrimp cultivation change into the closed or semi-closed methods. So the balanced management of DO in the waters has become the key problem of the shrimp cultivation. On the basis of the research of DO budget or kinetics in shrimp pond, the main influence process of DO and its seasonal variations are quantitatively described through redividing the budget process and modifying the quantitative method of the process.

1 Material and Methods

1.1 Experimental shrimp ponds and cultivation conditions

The experiment was carried out at the shrimp cultivation farm in Rizhao City, Shandong province of China. Experimental shrimp ponds were built ten years ago. So far, the semi-intensively managed method has been adopted in the ponds. During the experiment, shrimp culturing conditions were as follows: the culturing density was 150 000 shrimps/hm^2; mixed feed was mainly adopted in the cultivation; the feed was thrown into ponds along the edges; feed amount was calculated with the standard method of the Chinese shrimp cultivation; the average water depth of the ponds was 1.2m; exchanged water amount was generally 0~25% per day.

1.2 Supplement and consumption processes of DO

According to the characteristics of shrimp cultivation ecosystem, the following processes are discussed: respiration process of organisms, which mainly includes that of shrimp and phytoplankton, degradation process of allotrophic bacteria to organic matter; total oxygen consumption process of sediment, and photosynthesis process of phytoplankton. The liquid paraffin wax was used to cover the water surface to eliminate the effect of water-atmosphere exchange.

1.3 Quantitative methods of the processes

Shrimp respiration process is determined with the simulating method in laboratory. The DO Meter (Model YSI-58, USA) is used to monitor DO changes in the waters. The dissolved oxygen demand of shrimp respiration (DOD_{shm}) can be calculated from the determined oxygen consumption curve. The dissolved oxygen demand of phytoplankton respiration and allotrophic bacteria degrading organic matter in seawater are estimated with the two following formula (Kadowaki 1994).

$$DOD_{Chl\text{-}a} = \beta_t \cdot C_{Chl\text{-}a} \quad (1)$$

In formula (1), $DOD_{Chl\text{-}a}$ is the dissolved oxygen demand of phytoplankton respiration, β_t is temperature coefficient and $C_{Chl\text{-}a}$ is chlorophyll-a content in cultivation waters. β_t can be described as temperature function, that is, $\beta_t = \beta_{20} \cdot Q_{Chl\text{-}a}(t-20)$, in which α_{20} is the determined value of β_t at 20℃ (2.0 $mgO_2/mg_{Chl\text{-}a} \cdot h$), $Q_{Chl\text{-}a}$ is a constant (1.074) and t is the determined water temperature.

$$DOD_{Bact} = \alpha_t \cdot C_{Bact} \quad (2)$$

In formula (2), DOD_{Bact} is the dissolved oxygen demand of allotrophic bacteria degrading the organic matter, α_t is the temperature coefficient and C_{Bact} is the total number of bacteria in per unit waters. α_t can be described as temperature function, that is, $\alpha_t = \alpha_{20} Q_{Bact}(t-20)$, in which α_{20} is the determined value of α_t at 20℃ (0.8×10^{-9} mgO_2/cells · h), Q_{Bact} is a constant (1.089) and t is the determined water temperature. Total dissolved oxygen demand of sediment (DOD_{sedt}) is determined with in situ simulating method designed by the authors. Oxygen produced by phytoplankton photosynthesis is calculated by $C_{Chl\text{-}a}$ and photosynthesis index (Q). According to the reacting equation of photosynthesis,

$$6CO_2+6H_2O \rightarrow (CH_2)_6+6O_2$$

If the reactant is Glucose 1 mol O_2 can be produced by reducing 1 mol CO_2. However, products of photosynthesis usually still include protein and lipids. It is recognized that the actual productivity of oxygen should be obtained by primary productivity (P) multiplied by 0.8. The primary productivity (P)

value can be calculated by the formula supplied by Cardee (1975),

$$P = C_{\text{Chl-a}} \times Q \times D \tag{3}$$

In formula (3), D is the illuminating time every day. Q in shrimp ponds is closely linked to water temperature and the relationship can be appositely expressed as $Q = 0.439\,t - 5.822$ (Shen *et al.*, 1993). Generally it is the net primary productivity determined with the ^{14}C tracing method, so the phytoplankton respiration process in the day is neglected .

2 Results

2.1 Oxygen demand of shrimp respiration and the change with its weight

The per unit weight shrimp oxygen demand [SOD, (O_2) mg/g · h] reduces with the increment of shrimp weight (W). The relationship can be quantitatively described as a logarithm curve, SOD= $-0.12\text{Ln}\,W + 0.52$, $R^2 = 0.9921$. DOD_{shri} can be obtained from SOD multiplied by shrimp weight in per unit culturing water and its seasonal change.

2.2 Oxygen demand of phytoplankton respiration at night and its seasonal variation

There are positive and negative effects of phytoplankton on DO in culturing waters, which not only produces O_2 through photosynthesis during the day but also consumes it through respiration at night. The relations of $\text{DOD}_{\text{Chl-a}}$ with $C_{\text{chl-a}}$ and t are positively interrelated, so higher $\text{DOD}_{\text{Chl-a}}$ values are observed when $C_{\text{chl-a}}$ and t are also higher in July and August (Fig.1). Keeping the phytoplankton relatively stable has been regarded as the key factor of controlling the quality of shrimp cultivation water, so the seasonal change range of chlorophyll-a in the ponds is smaller in our experiment.

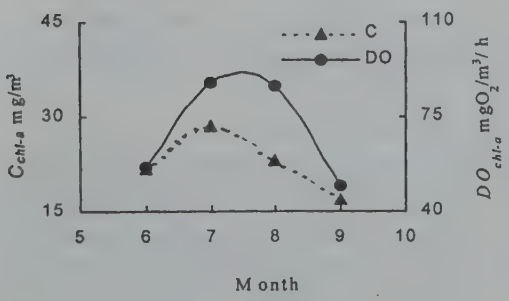

Fig.1 Chl-a and DOD_{Chla} in shrimp ponds and their seasonal variation

2.3 Oxygen demand of allotrophic bacteria degrading organic matters and its seasonal variation

The total amount of allotrophic bacteria in shrimp ponds and the dissolved oxygen demand in degrading organic matter process show an exponential increment during the experiment period. Their

increment patterns could be respectively described as the following exponential function, $DOD_{Bact} = 0.0108e^{0.98t'}$ ($R_2 = 0.9911$) and $C_{Bact} = 0.0135e^{0.91t'}$ ($R^2 = 0.9737$), t' is the cultivating season (Mon.).

2.4 Total oxygen demand of sediment and its seasonal variation

The total oxygen demand of sediment varies with the experiment seasons and areas (Fig.2). The value in the area polluted by feed remains is obviously higher than that in an unpolluted area, which increases largely with temperature and culturing time increment. But there is no apparent seasonal change in the unpolluted area. As the polluted area is about one-third of the total shrimp pond in the experiment, the mean DOD_{sed} can be obtained from the value of polluted area and unpolluted area. Its change trend with season can be described as a linear equation, $DOD_{sed} = 0.27t' - 42$, $R^2 = 0.9783$.

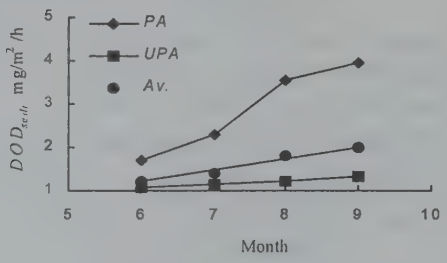

Fig.2 DOD_{Sedi} in shrimp pond and its seasonal variation

2.5 Supplement of DO and its seasonal variation in shrimp culturing water

In this paper the oxygen supplied by phytoplankton (DOS_{photo}) is mainly considered. DOS_{photo} and the primary productivity (P) and other calculating parameters are listed in Table 1, in which it is showed that the oxygen produced by phytoplankton is roughly equal to the oxygen consumption of phytoplankton and the higher values of them appear in July and August when the chlorophyll-a and temperature are also higher.

Tab. 1 P and its calculating parameters and DO_{chla} in shrimp ponds

Culturing seasons	*Cchla* (mg / m^3)	*D* (h / d)	*t** ℃	*Q* mgC / (mg$_{chla}$ • h)	*P* mgC / (m^3 • d)	DOS_{photo} gO$_2$ /(m^3 • d)
Jun.	21.84	14	25.6	4.54	16 54.2	3.53
Jul.	28.56	14	28.0	5.59	2 588.8	5.52
Aug.	23.12	13	30.8	6.82	2 312.3	4.93
Sep.	20.99	12	27.3	5.29	1 551.6	3.31

*t** is the average water temperature in illumination time everyday.

2.6 Budget condition of DO and its seasonal variation in shrimp culturing water

It is showed in Fig. 3 that the DO value is higher in the early period. It is smaller shrimps, lighter self-pollution and other reasons that make the supplement of DO more than the consumption of DO in the culturing water. After August, however, the total consumption of DO is more than the supplement, since the shrimp growth and more serious self-pollution lead to the increments of shrimp respiration, degrading organic matters of allotrophic bacteria and the total oxygen demand sediment. The actual monitoring results in the test shrimp pond show that DO is saturated or near saturated in the early days while lower in the midterm and later period.

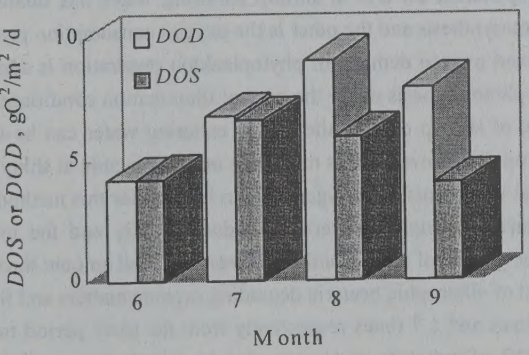

Fig.3 Budget condition of DO and its seasonal variation

3 Discusssion

In the different cultivation seasons, the percentages of oxygen demand of various processes in the total oxygen demand are different (Table 2). It is showed that the percentage of shrimp oxygen demand is lower, while the dissolved oxygen demand of mini-organisms is the major influencing factor of DO in this environment and approximately accounts for 64.1~74.1% of the total oxygen demand. In the early period of shrimp culture, the dissolved oxygen demand of allotrophic bacteria degrading organic matters is much lower than that of phytoplankton respiration. But in the midterm and later period, it is about 50% of the total oxygen demand because of the higher water temperature and more serious self-pollution. Madenjian et al. (1990) reported that the dissolved oxygen demand of sediment in shrimp ponds accounted for about 52% of the total oxygen demand. In this paper it is much lower and just 19.1~28.8%. The possible reason is that lower shrimp densityl has led to lighter pollution degree of bottom organic matter in comparison with their result.

Tab. 2 Percentage of oxygen demand of different processes in shrimp ponds

Seasons	Percentage of oxygen consumption (%)			
(Mon.)	DOD_{bact}	DOD_{chla}	DOD_{duri}	DOD_{sedi}
6	28.1	38.6	4.6	28.7
7	35.4	36.8	6.2	21.6
8	48.5	25.6	6.8	19.1
9	43.9	20.2	10.7	25.2

The effect of phytoplankton on DO in shrimp culturing water has dualism. One is the oxygen producing process of photosynthesis and the other is the oxygen consumption process of respiration. It is estimated that the dissolved oxygen demand of phytoplankton respiration is approximately one-fifth of the oxygen produced by photosynthesis under the normal illumination conditions. For this reason, in the midterm and later period of shrimp culture, the DO in culturing water can be improved by increasing phytoplankton density properly. However, this method is only applicable in shiny weather. In cloudy and rainy days, other measures of replenishing oxygen have to be used for this method is ineffective.

During shrimp culture, allotrophic bacteria reproduce rapidly and the total oxygen demand of sediment increase with the growth of shrimp and the increase of feed amount thrown into the ponds. The dissolved oxygen demand of allotrophic bacteria degrading organic matters and the total oxygen demand of sediment increase 4 times and 1.7 times respectively from the early period to the midterm and later period. Obviously, the DO of culturing water can also be greatly improved by controlling the self-pollution of organic matters during shrimp culture.

References

[1] Lu Maixin, Ou Yanghai, *et al.* (1992) The trends and management of dissolved oxygen in pond ecosystem [J]. *In Chinese Fresh fishery*, (4): 3~6.

[2] Zang Weiling, *et al.* (1995) Budget equation conditions of dissolved oxygen of *Penaeus chinensis* [J]. *In Chinese Acta Oceanologica Sinica*, **17** (4): 137-141.

[3] Madenjian C P. (1990) Patterns of oxygen production and consumption in intensively managed marine shrimp ponds [J].*Aquac Fish Manage*, **21**(4): 407-417.

[4] Shusaku KADOWAKI and Yoshiaki TANAKA. (1994) Oxygen consumption rates by phytoplankton and bacteria in sea water [J].*SUISANZOSHOKU*, **42** (2): 267-272.

[5] Sun Yao, *et al.* (1996) Total oxygen consumption of shrimp pond sediment and its seasonal variation [J]. *Chinese Journal of Applied Ecology*, **7** (1): 110-112.

[6] Shen Guoying, Lin Junmin, *et al.* (1992) Study on shrimp pond primary productivity and its use in cultivation early days [J].*In Chinese Journal of Xiamen University (natural science press)*, **31** (2): 188-193.

[7] Cadee G C. (1975) Primary production of the Guyana Coast [J]. *Netherlands J of Sea Res*, **4** (1): 128-143.

[8] Gao Shangde, Chen Xuren, *et al.* (1994) Variation of total bacteria number in shrimp pond waters and substrate during the adult culture of *Penaeus chinensis* [J].*Journal of Fisheries of China*, **18** (2): 138-142.

Marine Science Bulletin

Marine Science Bulletin publishes papers on marine science and technology including physical oceanography, chemical oceanography, marine biology, marine geology, environmental oceanography, estuarine & coastal sciences, marine technology, digital ocean, coastal zone management, ocean engineering, marine economics, etc., and aims to promote international academic cxchange.

Editor-in-Chief: Wang Hong（王　宏）
Deputy Editor-in-Chief: Lin Baofa（林宝法） Zhao Xucai（赵绪才）
Yang Ying（杨　鹰）
Executive Editor: Xu Jie（徐　杰） Zhang Deshan（张德山）
Computer typist: Cheng Xiuchun（程秀春）

Marine Science Bulletin **(Vol .3 No.2 Oct. 2001)**

Responsible Institution:
State Oceanic Administration of China
Edited and Published Semi-annually by:
National Marine Data and Information Service
Address: 93 Liuwei Road, Hedong District, Tianjin 300171, China
E-mail: msb@mail.nmdis.gov.cn

ISSN1000-9620
CN12-1271/N

Price: $ 30.00 Per year